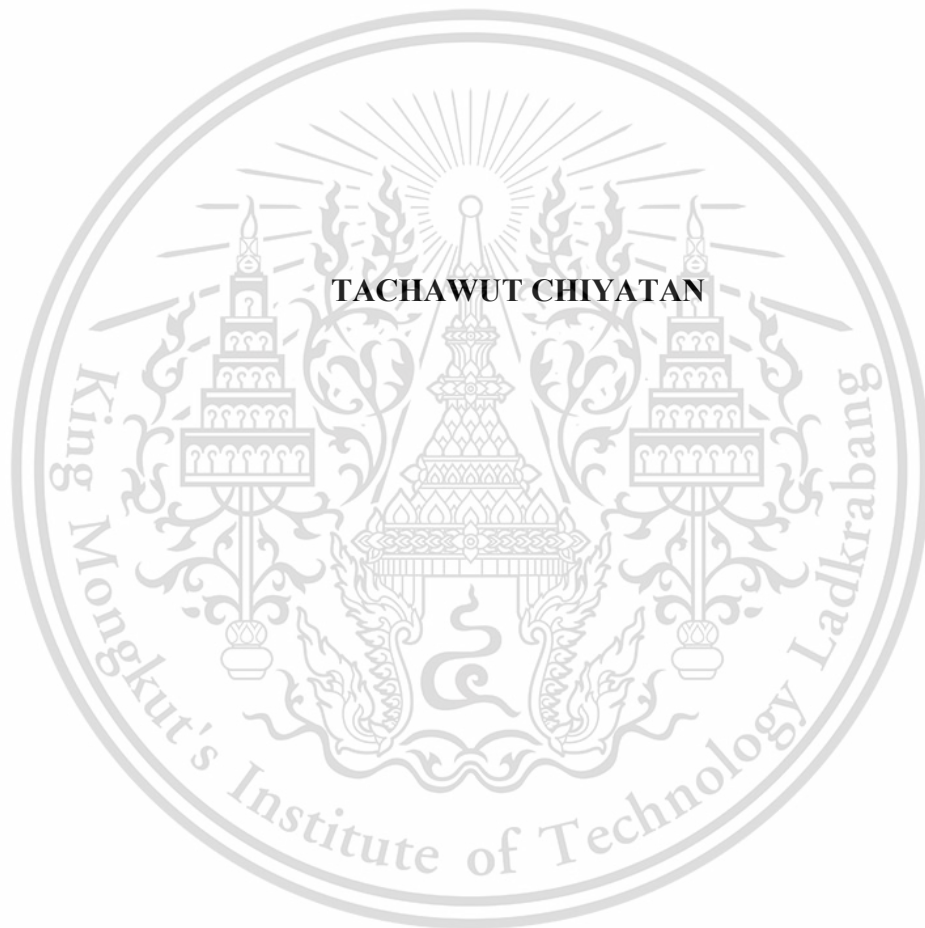


**AN EXPERIMENTAL STUDY AND MICROSTRUCTURE SIMULATION OF  
HIGH STRENGTH STEELS UNDER HIGH STRAIN RATE DEFORMATION**



**A THESIS REPORT SUBMITTED IN PARTIAL FULFILLMENT  
OF THE REQUIREMENTS FOR THE DEGREE OF  
MASTER OF ENGINEERING IN AUTOMOTIVE ENGINEERING  
INTERNATIONAL COLLEGE  
KING MONGKUT'S INSTITUTE OF TECHNOLOGY LADKRABANG  
ACADEMIC YEAR 2018  
KMITL-2018-IC-M-004-008**

**AN EXPERIMENTAL STUDY AND MICROSTRUCTURE SIMULATION OF  
HIGH STRENGTH STEELS UNDER HIGH STRAIN RATE DEFORMATION**



**A THESIS REPORT SUBMITTED IN PARTIAL FULFILLMENT  
OF THE REQUIREMENTS FOR THE DEGREE OF  
MASTER OF ENGINEERING IN AUTOMOTIVE ENGINEERING  
INTERNATIONAL COLLEGE  
KING MONGKUT'S INSTITUTE OF TECHNOLOGY LADKRABANG  
ACADEMIC YEAR 2018**

**KMITL-2018-IC-M-004-008**

This material is reserved for educational use only, not allowed for commercial use.

Forbidden to modify the content, and cite the document when use.



This material is reserved for educational use only, not allowed for commercial use.  
Forbidden to modify the content, and cite the document when use.

<b>THESIS TITLE</b>	An experimental study and microstructure simulation of high strength steels under high strain rate deformation
<b>STUDENT NAME</b>	Mr. Tachawut Chiyatan
<b>STUDENT ID</b>	59610046
<b>DEGREE</b>	Master of Engineering
<b>PROGRAMME</b>	Automotive Engineering
<b>ADVISOR</b>	Asst.Prof.Dr. Preechar Karin
<b>CO-ADVISOR</b>	Assoc.Prof.Dr. Vitoon Uthaisangsuk
<b>CO-ADVISOR</b>	Prof.Dr. Naoto Ohtake

## ABSTRACT

By the automotive structure design, crashworthiness has become also an important issue so that a better understanding of plastic deformation of material at high velocity is necessary. The effects of strain rate on mechanical properties and fracture mechanism of ferritic-martensitic dual phase (DP) steel grades 780 and 1000 were investigated by both experiments and micromechanics based modeling. For the examined steels, quasi-static ( $0.001 \text{ s}^{-1}$ ) and medium strain rate ( $0.5\text{-}1 \text{ s}^{-1}$ ) tensile tests were carried out on a universal testing machine, while high strain rate ( $1500\text{-}2500 \text{ s}^{-1}$ ) tests were performed by a Split-Hopkinson tensile bar. Afterwards, FE simulations using 2D representative volume elements (RVEs) were conducted for investigating microstructure effects on local deformation and damage of DP steels under varying strain rates. Flow curves of observed phase constituents at different strain rates were described by using a dislocation based theory and local chemical composition in combination with the Johnson-Cook (JC) hardening model. Furthermore, individual damage criteria based on the rate-dependent JC failure model were applied to describe the local crack mechanisms in DP microstructures. Calculated local stresses, strains and damage developments of deformed phases were studied. It was found that microstructure characteristics especially phase fraction differently affected the strain hardening and ductility of DP steels under low and high strain rate deformation. The damage initiation and propagation in microstructures of both steels at various strain rates predicted by RVE simulations were well correlated with the experimental results.

## ACKNOWLEDGEMENT

I gratefully acknowledge the scholarship from Thailand Advanced Institute of Science and Technology (TAIST-Tokyo Tech), and Tokyo Institute of Technology, which is a collaborative program among of National Science and Technology Development Agency (NSTDA, Thailand), Tokyo Institute of Technology (Tokyo-Tech, Japan), King Mongkut's Institute of Technology Ladkrabang (KMUTL, Thailand) and King Mongkut's University of Technology Thonburi (KMUTT, Thailand).

Without the contribution of many people, this thesis would not have been existed. It owes the existence to the supports and inspirations from a lot of people.

To my thesis advisor Asst. Prof. Dr. Preechar Karin of International College at KMUTL and co-advisor Assoc. Prof. Dr. Vitoon Uthaisangsuk of department of mechanical engineering at KMUTT, I would like to express my deepest gratitude for the encouragement and supervision through all obstacles and challenges since the beginning until the end of my study.

I also want to express my gratitude to all lecturers for your support and guidance to me for the whole three years. Also, I would like to thank my colleagues, friends, TAIST, KMUTL and KMUTT staffs for their support and helps in everything. Besides, I wish to thank Summit Auto Body Industry co. ltd and Advance Instrument Inc. for supported materials and mechanical testing. Moreover, I also would love to express my gratitude to all respondents who contribute their information and time on this study. And I do believe the study could not been done without their input.

Finally, I must express my very greatest gratitude to my parents and all relatives for providing me with unfailing support and continuous motivation throughout my years of study. This accomplishment would not have been possible without them.

Tachawut Chiyatan

## TABLE OF CONTENTS

<b>Chapter</b>	<b>Page</b>
ABSTRACT.....	I
ACKNOWLEDGEMENT .....	II
TABLE OF CONTENTS.....	III
LIST OF TABLES.....	VII
LIST OF FIGURES .....	VII
LIST OF SYMBOLS .....	XI
LIST OF DEFINITIONS .....	XIV
CHAPTER 1 INTRODUCTION .....	1
1.1 Research Background and Literature Reviews .....	1
1.2 Research Objectives .....	10
1.3 Scopes of Work .....	10
1.4 Expected Benefits.....	11
CHAPTER 2 THEORETICAL FUNDAMENTS.....	12
2.1 Advanced high strength steel .....	12
2.2 Dual phase steel.....	13
2.2.1 Microstructure and mechanical properties of dual phase steel.....	13
2.2.2 Fracture behaviour of dual phase steel .....	13
2.3 Mechanical testing machine types.....	17
2.3.1 Universal testing machine .....	13
2.3.2 Split-Hopkinson tensile bar .....	13
2.4 Flow curve model.....	22
2.4.1 Macroscopic flow curve model .....	23
2.4.2 Single phase flow curve model.....	23

This material is reserved for educational use only, not allowed for commercial use.

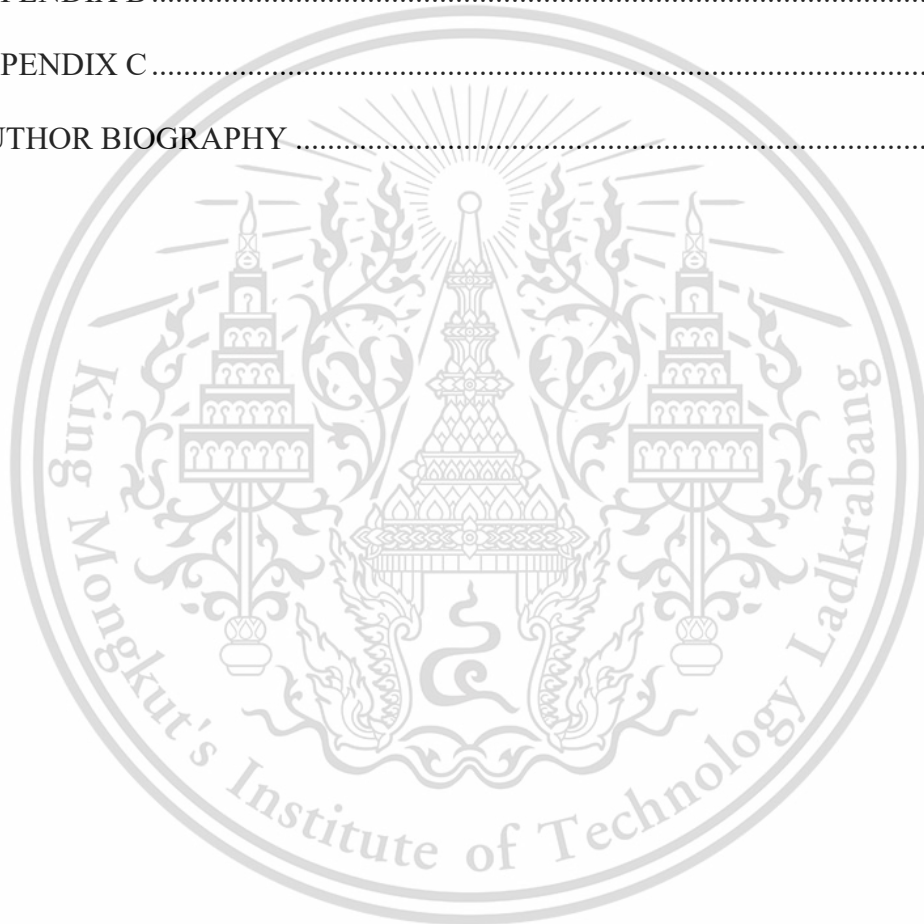
Forbidden to modify the content, and cite the document when use.

2.4.3 Dynamic flow curve model .....	25
2.5 Damage model.....	26
2.6 Digital image correlation.....	29
CHAPTER 3       EXPERIMENTS .....	31
3.1 Materials and microstructures .....	31
3.1.1 Chemical composition analysis .....	31
3.1.2 Microstructure characterization.....	32
3.2 Quasi-static uniaxial tensile tests .....	34
3.3 Tensile tests at various strain rates .....	35
3.3.1 Quasi-static to medium strain rate tensile tests .....	35
3.3.2 High strain rate tensile tests.....	36
CHAPTER 4       EXPERIMENTS RESULTS.....	38
4.1 Tensile properties .....	38
4.2 Stress-strain behaviour at various strain rates .....	39
4.3 Obseravtion of crack development.....	40
4.4 Fractographs analysis .....	42
CHAPTER 5       MODELLING AND SIMULATION .....	45
5.1 Macroscopic flow curve model .....	45
5.2 Representative volume element (RVE).....	47
5.3 Micromechanics based flow curve modelling.....	48
5.3.1 Single phase flow curves for quasi-static deformation.....	48
5.3.2 Singe phase flow curves for high strain rate deformation .....	50
5.4 Ductile damage criterion for micromechanical modelling.....	52
5.4.1 Determination of static damage loci for martensite.....	52
5.4.2 Determination of static damage loci for ferrite .....	57

This material is reserved for educational use only, not allowed for commercial use.

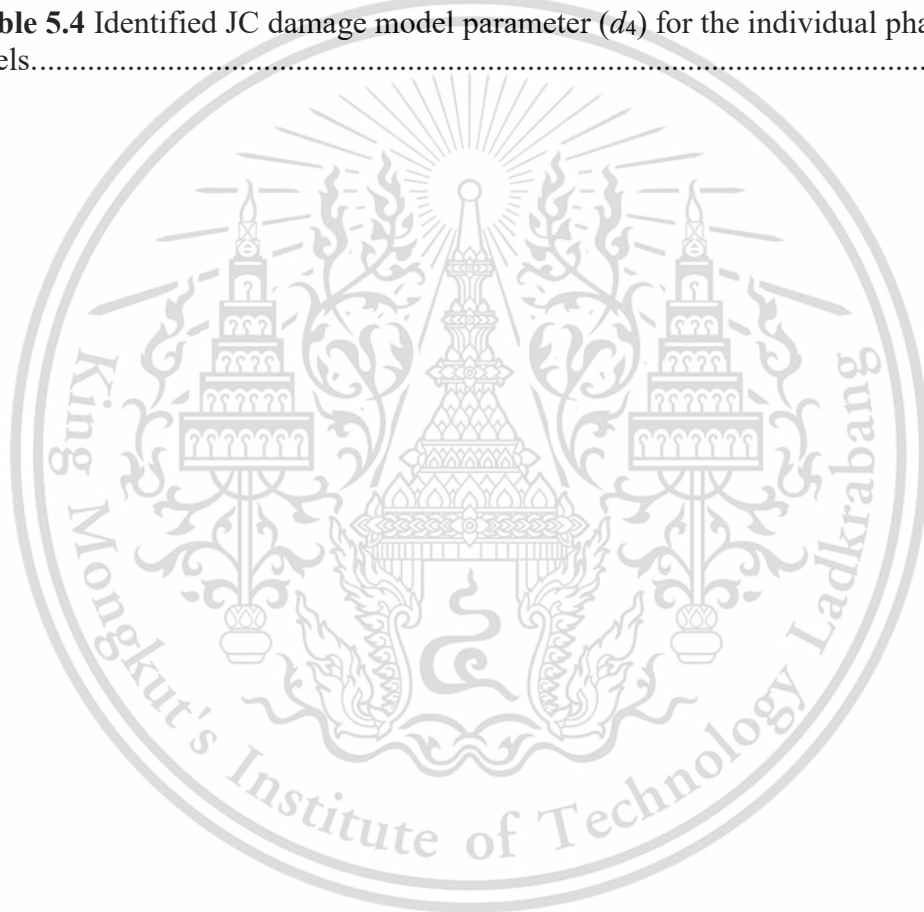
Forbidden to modify the content, and cite the document when use.

5.4.3 Rate-dependent damage locus .....	59
5.4.4 Damage initiation and damage evolution in RVE simulation .....	61
CHAPTER 6 SIMULATION RESULTS AND DISCUSSIONS .....	63
CHAPTER 7 CONCLUSIONS.....	70
REFERENCES .....	72
APPENDIX A.....	89
APPENDIX B.....	80
APPENDIX C.....	81
AUTHOR BIOGRAPHY.....	89



## LIST OF TABLES

Table	Page
<b>Table 3.1</b> Chemical composition of the used steel grade 780 and 1000 .....	32
<b>Table 3.2</b> The resulted microstructure analysis of investigated steels .....	33
<b>Table 4.1</b> Resulted tensile properties of investigated steels.....	38
<b>Table 5.1</b> Obtained plasticity model parameters of the investigated steels .....	46
<b>Table 5.2</b> Used heat treatment parameters for generating fully martensitic steels with different carbon contents.....	53
<b>Table 5.3</b> The values of applied uniform loads $F_1$ and $F_2$ for different stress triaxialities .....	58
<b>Table 5.4</b> Identified JC damage model parameter ( $d_4$ ) for the individual phases in DP steels.....	61



## LIST OF FIGURES

Figure	Page
<b>Figure 1.1</b> The European New Car Assessment Programme (Euro NCAP) frontal impact tests of SUV car .....	1
<b>Figure 1.2</b> Building block approach for safety design of vehicle .....	2
<b>Figure 1.3</b> a) Universal tensile testing machine b) The Split Hopkinson tensile bar....	2
<b>Figure 1.4</b> a) Automotive components made by DP steels and b) Future trend use of steels for automotive body .....	3
<b>Figure 1.5</b> The engineering stress-strain curves under static and dynamic tensile tests of the DP600 (a) and DP1000 (b) .....	3
<b>Figure 1.6</b> Comparison for a representative test, DP500, at $1110 \text{ s}^{-1}$ . (a) High speed images, wherein dashed lines are the edges of the specimen detected from (c). (b) The field of axial strain from DIC. The image in the background is always the reference image, while the color plots represent the deformed strain field. (c) The field of axial strain of the whole specimen from FE simulation .....	4
<b>Figure 1.7</b> The methodological flow of the multi-scale study on high strength steel sheets for the crashworthiness property across the component level, lab level and microstructure and process routines.....	5
<b>Figure 1.8</b> Presentation of light optimal microscopic microstructures and the created RVEs (contained in the red boxes) for DP600 steels with different volume fractions of martensite: (a) 20% (RVE size is $40 \mu\text{m} \times 40 \mu\text{m}$ ), (b) 37% (RVE size is $32 \mu\text{m} \times 32 \mu\text{m}$ ) and (c) 46% (RVE size is $40 \mu\text{m} \times 40 \mu\text{m}$ ) .....	6
<b>Figure 1.9</b> Distribution of (a) Von Mises stress and (b) equivalent plastic strain in RVE of DP600 steel with 46% martensite after stretching.....	6
<b>Figure 1.10</b> Influence of Johnson-Cook constitutive model on stress and strain curve (Purple line is normal stress and strain curve, green line is stress and strain curve under high strain rates and red line is stress and strain curve under higher temperature) .....	7
<b>Figure 1.11</b> Final collapsed mode of the present model with impacting velocity of 15m/s for two side views: (a) $L=176\text{mm}$ (b) $L=264\text{mm}$ (c) $L=310\text{mm}$ and (d) $L=350\text{mm}$ .....	7
<b>Figure 1.12</b> Determined equivalent plastic strain from DIC and stress triaxiality from FEM values of specimens .....	8
<b>Figure 1.13</b> The resulted obtaining fracture locus of steel DP980 (Transverse direction) .....	9
<b>Figure 1.14</b> Calculated ductile damage initiation of RVE under various stress triaxiality for the 20:80 Martensitic/bainite microstructure .....	9
<b>Figure 2.1</b> Typical steels classified by mechanical properties.....	12
<b>Figure 2.2</b> AHSS usage in automotive body.....	13
<b>Figure 2.3</b> Typical ferritic-martensitic microstructure of DP steel.....	14
<b>Figure 2.4</b> Quasi-static flow stress behaviour of DP steel with different martensite volume fraction .....	14
<b>Figure 2.5</b> Variation in yield strength, ultimate tensile strength and uniform elongation for DP600 and DP800 at different strain rates .....	15
<b>Figure 2.6</b> TEM images of ferrite structures (a,b) and martensite lath structures (c,d). (a,c) quasi-static $\sim 10^{-4} \text{ s}^{-1}$ and (b,d) high strain rate $\sim 10^3 \text{ s}^{-1}$ .....	16
<b>Figure 2.7</b> Typical stress-strain curves of brittle and ductile materials .....	16

This material is reserved for educational use only, not allowed for commercial use.

Forbidden to modify the content, and cite the document when use.

## LIST OF FIGURES

(Continued)

Chapter	Page
<b>Figure 2.8</b> Fracture surface of DP1000 steel after a quasi-static deformation.....	17
<b>Figure 2.9</b> The level of strain rate in mechanical tests.....	18
<b>Figure 2.10</b> Typical ranges of strain rate covered by conventional load frames, servo-hydraulic machines and bar testing systems and accordingly flow stress for typical steel .....	18
<b>Figure 2.11</b> Schematic diagram of the split-Hopkinson tensile bar apparatus.....	20
<b>Figure 2.12</b> The split-Hopkinson tensile bar apparatus .....	20
<b>Figure 2.13</b> Velocity direction of striker bar and wave propagation direction in the split-Hopkinson tensile bar system .....	21
<b>Figure 2.14</b> Typical forms of waves acquired from strain gauges.....	22
<b>Figure 2.15</b> The clamping specimen sheet to the loading bar system.....	22
<b>Figure 2.16</b> Comparison of models for quasi-static flow curve extrapolation.....	23
<b>Figure 2.17</b> The generated single phase flow curves of ferrite and martensite in DP590 steel .....	24
<b>Figure 2.18</b> Comparison of the Johnson-Cook model predictions with experimental results of DP500 steel .....	26
<b>Figure 2.19</b> Ductile damage in metal driven by void nucleation, void growth and void coalescence until crack propagation .....	27
<b>Figure 2.20</b> Relationship between stress triaxiality and equivalent plastic strain as a damage criterion.....	27
<b>Figure 2.21</b> Dependence of the equivalent strain to fracture on the stress triaxiality taken into account of shear fracture phenomenon at quasi-static deformation.....	28
<b>Figure 2.22</b> Developed damage curve in combination with strain rate function .....	29
<b>Figure 2.23</b> Detected the deformation of specimen using high quality camera.....	30
<b>Figure 2.24</b> Reference photos and images after the transformation of the specimen .....	30
<b>Figure 3.1</b> Flow chart of the research methodology .....	31
<b>Figure 3.2</b> (a) a light optical microscope and (b) scanning electron microscope .....	32
<b>Figure 3.3</b> Observed initial microstructure of steel grade (a,c) 780, (b,d) 1000 and (a,b) observed by LOM, (c,d) observed by SEM.....	33
<b>Figure 3.4</b> Dimension of the SS specimen for quasi-static uniaxial tensile test .....	34
<b>Figure 3.5</b> Test setup of universal testing machine for quasi-static tensile tests .....	34
<b>Figure 3.6</b> Obtained major strain of the SS specimen by using DIC technique .....	35
<b>Figure 3.7</b> MS specimen for tensile test at different strain rates.....	35
<b>Figure 3.8</b> Quasi-static deformation of MS specimen at strain rate of $0.001 \text{ s}^{-1}$ .....	36
<b>Figure 3.9</b> Test setup of SHTB system for high strain rate tensile tests .....	37
<b>Figure 4.1</b> Determined true stress-true strain curves under quasi-static uniaxial deformation of the steel grades 780 and 1000 .....	38
<b>Figure 4.2</b> Determined engineering stress-strain curves at different strain rates of steel grades (a) 780 and (b) 1000 .....	40
<b>Figure 4.3</b> Influences of strain rate on (a) yield strength, tensile strength, fracture elongation and (b) energy absorption of examined steel grade 780 and 1000.....	40

This material is reserved for educational use only, not allowed for commercial use.

Forbidden to modify the content, and cite the document when use.

## LIST OF FIGURES

(Continued)

Chapter	Page
<b>Figure 4.4</b> SEM images of microstructures close to the fracture surfaces of steel grade 780 after tensile tests under (a, b) quasi-static condition, (c) high strain rate and of steel grade 1000 under (d, e) quasi-static condition and (f) high strain rate. (F is ferrite and M is martensite).....	42
<b>Figure 4.5</b> Definition of the fracture surface in the necking zone .....	42
<b>Figure 4.6</b> Fracture surfaces of grade (a) 780 at quasi-static condition, (b) 780 at high strain rate, (c) 1000 at quasi-static condition and (d) 1000 at high strain rate by SEM .....	44
<b>Figure 4.7</b> Resulted dimple size distributions in fracture surfaces of grade (a) 780 and (b) 1000 at various strain rates.....	44
<b>Figure 5.1</b> Quasi-static stress-strain curves of grade (a) 780 and (b) 1000 from tensile tests and predicted by the combined Swift-Voce model.....	46
<b>Figure 5.2</b> Stress-strain curves at various strain rates of grade (a) 780 and (b) 1000 from dynamic tensile tests and predicted by Swift-Voce model combined with JC strain rate hardening model.....	46
<b>Figure 5.3</b> 2D RVE models used for the examined steel grades (a) 780 and (b) 1000 .....	47
<b>Figure 5.4</b> The symmetry boundary condition of RVE tensile simulation .....	50
<b>Figure 5.5</b> Static stress-strain curves of single phases and steel grades (a) 780 and (b) 1000 obtained by experiments and RVE simulations .....	50
<b>Figure 5.6</b> Flow stress curves of steel grades (a) 780 and (b) 1000 at different strain rates obtained by experiments and RVE simulations in comparison.....	52
<b>Figure 5.7</b> Observed microstructure of quenched fully martensitic steel in different carbon contents of (a) 0.209%, (b) 0.294%, and (c) 0.494%.....	53
<b>Figure 5.8</b> Stress-strain curves of quenched martensitic steels with different carbon contents in comparison with modelled single phase flow curves of martensite in the investigated DP steels .....	54
<b>Figure 5.9</b> Determined relationship between equivalent plastic strain at prior fracture and carbon percentage of martensitic steels.....	54
<b>Figure 5.10</b> Dimension of (a) pure shear, (b) combined shear, (c) uniaxial with hole, (d) U-notched tensile specimens for determining damage criterion.....	55
<b>Figure 5.11</b> Determined distributions of equivalent plastic strains and stress triaxiality of shear specimen at prior fracture of 0.209%C martensitic steels.....	56
<b>Figure 5.12</b> Comparative resulted equivalent plastic strain path from DIC and FE simulation. Note that Path 1, Path 2, Path 3 are repeatable DIC experiments.....	56
<b>Figure 5.13</b> Damage locus determined by DIC and FE simulation for 0.209%C martensitic steel specimen .....	56
<b>Figure 5.14</b> Determined damage loci for martensite with various carbon percentages in investigated steels .....	57
<b>Figure 5.15</b> Boundary condition for RVE simulations under various load direction .....	58
<b>Figure 5.16</b> Damage loci for ferrite in steel grade (a) 780 and (b) 1000 determined by RVE simulations coupled with the data from (Charoensuk, Panich, and Uthaisangsuk 2017).....	59

This material is reserved for educational use only, not allowed for commercial use.

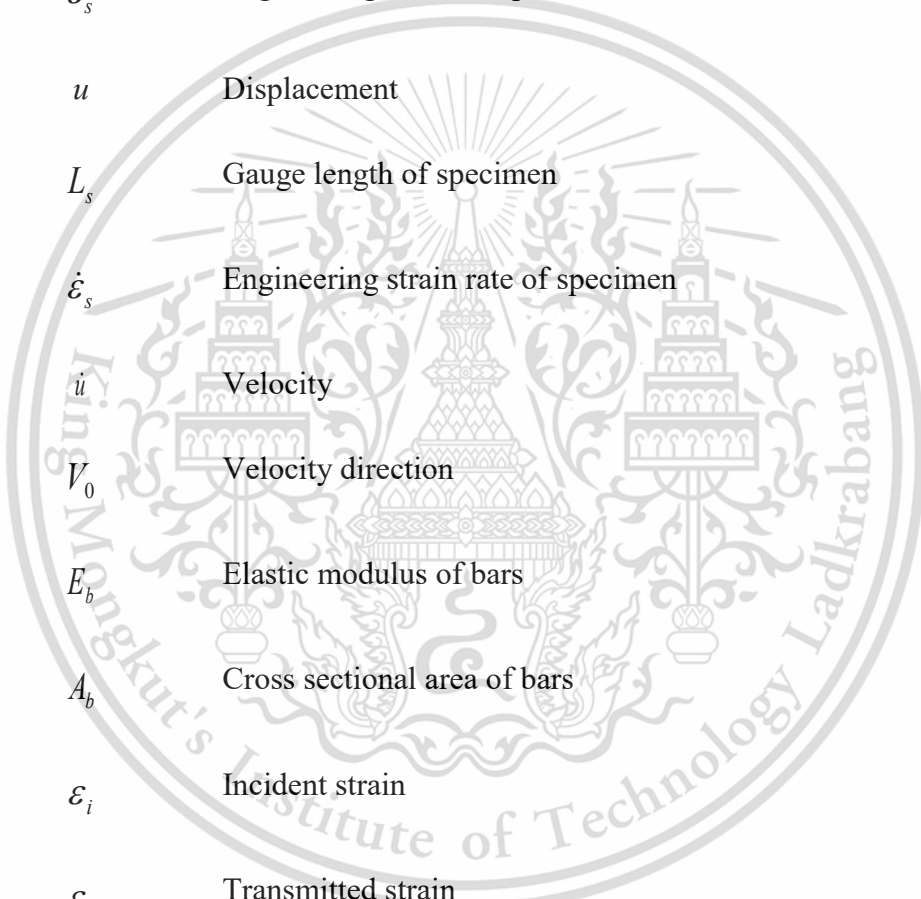
Forbidden to modify the content, and cite the document when use.

## LIST OF FIGURES

(Continued)

Chapter	Page
<b>Figure 5.17</b> (a) Determined stress-strain curves at different strain rates of 0.209%C martensitic steel and (b) relationship between fracture strain and strain rate.....	60
<b>Figure 5.18</b> Determined rate-dependent damage loci for martensite in (a) grade 780 and (b) 1000 and for ferrite in (c) grade 780 and (d) grade 1000 .....	61
<b>Figure 6.1</b> Resulted local stresses and damage appearance by RVE simulations for steel grade 780 and 1000 under uniaxial deformation at different strain rates.....	63
<b>Figure 6.2</b> Damage initiation, damage propagation and strain distributions in microstructure of grade 780 under quasi-static loading predicted by RVE simulations .....	65
<b>Figure 6.3</b> Damage initiation, damage propagation and strain distributions in microstructure of grade 780 under high strain rate loading predicted by RVE simulations .....	65
<b>Figure 6.4</b> Damage initiation, damage propagation and strain distributions in microstructure of grade 1000 under quasi-static loading predicted by RVE simulations .....	66
<b>Figure 6.5</b> Damage initiation, damage propagation and strain distributions in microstructure of grade 1000 under high strain rate loading predicted by RVE simulations .....	66
<b>Figure 6.6</b> Percentages of damaged areas and distributions of damage variables and equivalent plastic strains at the overall strain 0.182 in (a) ferrite and (b) martensite of steel grade 780 .....	67
<b>Figure 6.7</b> Percentages of damaged areas and distributions of damage variables and equivalent plastic strain at the overall strain 0.146 in (a) ferrite and (b) martensite of steel grade 1000 .....	67
<b>Figure 6.8</b> Calculated stress-strain responses of ferrite and martensite in steel grade (a) 780 and (b) 1000 under loading with different strain rates obtained by RVE simulations .....	68
<b>Figure 6.9</b> Overall stress-strain curves of steel grade (a) 780 and (b) 1000 under static and dynamic loading from experimental tensile tests and RVE simulations.....	69
<b>Figure A.1</b> Resulted XRD investigation of TRIP effect on steel grade 780.....	79
<b>Figure A.2</b> Resulted XRD investigation of TRIP effect on steel grade 1000.....	79
<b>Figure B.1</b> Resulted stress-strain behaviour of RVE simulations of steel 780 in different microstructure characteristic at dynamic strain rate.....	80
<b>Figure B.2</b> Local damage in RVE simulations of steel 780 in different microstructure characteristic at dynamic strain rate.....	80

## LIST OF SYMBOLS



$\sigma_s$	Engineering stress of specimen
$F$	Force
$A_s$	Cross sectional area of specimen
$\varepsilon_s$	Engineering strain of specimen
$u$	Displacement
$L_s$	Gauge length of specimen
$\dot{\varepsilon}_s$	Engineering strain rate of specimen
$\dot{u}$	Velocity
$V_0$	Velocity direction
$E_b$	Elastic modulus of bars
$A_b$	Cross sectional area of bars
$\varepsilon_i$	Incident strain
$\varepsilon_t$	Transmitted strain
$c_b$	Velocity of stress wave through the bars
$\varepsilon_r$	Reflected strain
$t$	Time duration of experiment
$\sigma$	Equivalent stress

This material is reserved for educational use only, not allowed for commercial use.

Forbidden to modify the content, and cite the document when use.

## LIST OF SYMBOLS

(Continued)

$\varepsilon$	Equivalent plastic strain
$T$	Temperature function
$A, B, n, C, m$	The Johnson-Cook constitutive model constant parameters
$\dot{\varepsilon}$	Strain rate
$\dot{\varepsilon}_0$	Reference strain rate
$\eta$	Stress triaxiality
$\sigma_h$	Hydrostatic stress
$\sigma_v$	Von Mises stress
$\sigma_1, \sigma_2, \sigma_3$	Principal stress
$d_1, d_2, \dots, d_5$	The Johnson-Cook damage model constant parameters
$\varepsilon_p^f$	Equivalent plastic strain at onset of the damage
$\varepsilon_\eta^f$	Equivalent plastic strain depended stress triaxiality
$\varepsilon_{\dot{\varepsilon}}^f$	Equivalent plastic strain depended strain rate
$\dot{\varepsilon}_p$	Equivalent plastic strain rate
$A, \varepsilon_0, n, k_0, Q, \beta, \alpha$	The Swift and Voce parameters
$\sigma_0$	The Peries stress and effects of alloy elements in solid solution

This material is reserved for educational use only, not allowed for commercial use.

Forbidden to modify the content, and cite the document when use.

## LIST OF SYMBOLS

(Continued)

$\Delta\sigma$	Strengthening by carbon in solution
$\alpha$	Material constant
$\lambda$	Grain size diameter
$\dot{\gamma}$	Micromechanical strain rate
$\tau$	Micromechanical shear stress
$\rho$	Local dislocation density
$M$	Taylor factor
$\mu$	Shear modulus
$b$	Burger's vector
$k_r$	Recovery rate
$L$	Dislocation mean free path
$\%C_{ss}^f$	Carbon content in ferrite (in wt.%)
$\%C_{ss}^m$	Carbon content in martensite (in wt.%)
$d_\alpha$	Average grain size of ferrite
$\mathcal{E}_{p(\eta, \%C)}^f$	Equivalent plastic strain depended carbon content
$\%C$	Carbon content (in wt.%)
$\omega_D$	Damage indicator

This material is reserved for educational use only, not allowed for commercial use.

Forbidden to modify the content, and cite the document when use.

## LIST OF DEFINITIONS

<b>Euro NCAP</b>	The European New Car Assessment Programme
<b>DP</b>	Dual Phase
<b>AHSS</b>	Advanced High strength steel
<b>SHTB</b>	Split-Hopkinson Tensile Bar
<b>FE</b>	Finite Element
<b>RVE</b>	Representative Volume Element
<b>LOM</b>	Light Optical Microscopy
<b>JC</b>	The Johnson-Cook
<b>GTN</b>	The Gurson-Tvergaard-Needleman
<b>DIC</b>	Digital Image Correlation
<b>2D</b>	Two Dimensional plane
<b>SEM</b>	Scanning Electron Microscopy
<b>CP</b>	Complex Phase
<b>MS</b>	Martensitic
<b>TRIP</b>	Transformation-Induced Plasticity
<b>HF</b>	Hot-Formed
<b>TWIP</b>	Twinning-Induced plasticity
<b>TEM</b>	Transmission Electron Microscopy
<b>CCD</b>	High quality camera
<b>ASTM</b>	American Society for Testing and Materials

This material is reserved for educational use only, not allowed for commercial use.

Forbidden to modify the content, and cite the document when use.

## LIST OF DEFINITIONS

(Continued)

<b>wt. %</b>	Weight Percentage
<b>SS</b>	The standard specimen
<b>MS</b>	Modified specimen
<b>YS</b>	Yield Strength
<b>UTS</b>	Ultimate Tensile strength
<b>UE</b>	Uniform Elongation
<b>s<sup>-1</sup></b>	Unit of inverse time
<b>MPa</b>	Megapascal Pressure Unit
<b>μm<sup>2</sup></b>	Square Micrometer
<b>μm</b>	Micrometer
<b>in<sup>2</sup></b>	Square Inch
<b>ml</b>	Milliliter
<b>Abaqus/CAE</b>	Finite Element simulation software
<b>CPE4</b>	Two Dimensional plane strain element
<b>S, Mises</b>	Von Mises stress or Equivalent stress
<b>DCPD</b>	Direct Current Potential Drop
<b>SDEG</b>	Stiffness degradation variable
<b>PEEQ</b>	Equivalent plastic strain
<b>DUCTRT</b>	Damage indicator history variable

This material is reserved for educational use only, not allowed for commercial use.

Forbidden to modify the content, and cite the document when use.

# CHAPTER 1

## INTRODUCTION

### 1.1 Research Background and Literature Reviews

Currently, the automotive technologies have been rapidly developed, for example growth of hybrid, electric and autonomous vehicles. On the other hand, the number of car accidents still increases from year to year. Therefore, improved structure and development of new materials for car bodies are necessary in order to enhance the safety of passenger. In automotive industries, crashworthiness testing has been taken into account for occupant safety, as shown in figure 1.1. Therefore, the evaluation of structural components under impact load or crashworthiness must be more precise, for which a better understanding of strain rate dependency of used material is indispensable, as illustrated in figure 1.2.



**Figure 1.1** The European New Car Assessment Programme (Euro NCAP) frontal impact tests of SUV car.

Source: (Autocarindia. 2015)

The effects of strain rate on mechanical properties and fracture behavior of various alloys could be examined by quasi-static, medium strain rate and high strain rate tensile tests in (Kim *et al.*, 2013; Anderson *et al.*, 2014; Rahmaan *et al.*, 2016; Erice, Roth and Mohr, 2018). For high strain rate testing of sheet metals, the Split Hopkinson tensile bar (SHTB) technique is widely employed (Chen *et al.*, 2011; Singh *et al.*, 2011; Qin *et al.*, 2013), while quasi-static and medium strain rate tests are commonly performed by using universal testing machine as illustrated in figure 1.3.

This material is reserved for educational use only, not allowed for commercial use.

Forbidden to modify the content, and cite the document when use.

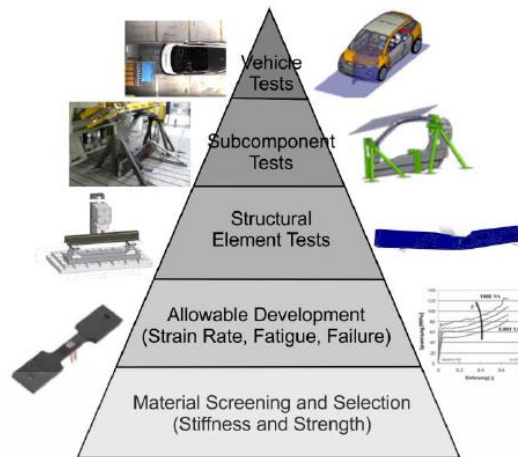


**Figure 1.2** Building block approach for safety design of vehicle.

Source: (Hesse, 2014)

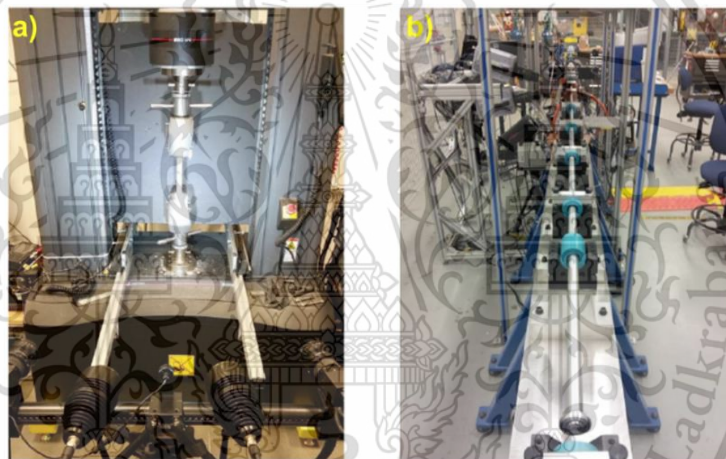


**Figure 1.3** a) Universal tensile testing machine b) The Split Hopkinson tensile bar.

Source: (Alturk *et al.*, 2017)

To achieve a greater efficiency of fuel consumption of vehicle lightweight design plays increasingly important role. For this purpose, new grades of advance high strength steel (AHSS) have been introduced in the automotive industries. The dual phase (DP) steel is one of the most important AHSS grades that exhibit advantageous mechanical properties. The low yield strength to ultimate tensile strength ratio of the DP steels lead to superior formability in combination with high resulting strength. Thus, DP steels have been increasingly used in various automotive crash-resistant components, in which weight reduction and improved passive safety due to large energy absorbability can be reached simultaneously (Uthaisangsuk, Prah and Bleck, 2009), as illustrated in figure 1.4a, and the future trend use of steels in vehicle is demonstrated in figure 1.4b.

This material is reserved for educational use only, not allowed for commercial use.

Forbidden to modify the content, and cite the document when use.

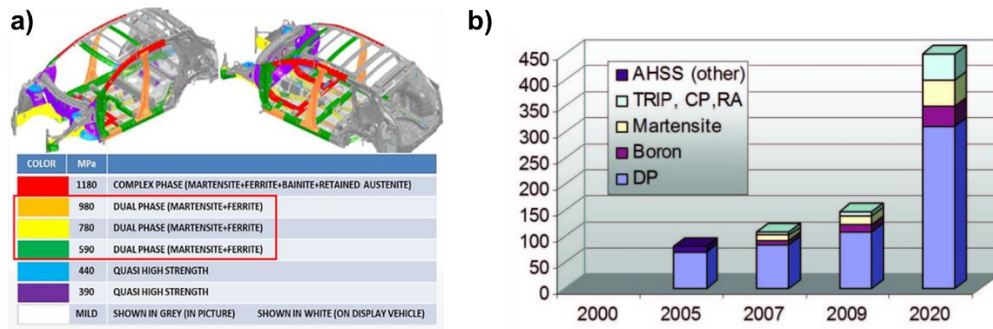


**Figure 1.4** a) Automotive components made by DP steels and b) Future trend use of steels for automotive body.

The DP steel is a type of low carbon steel, which possesses multiphase microstructure consisting of soft ferrite matrix and hard martensitic islands. By deformation of DP steel under quasi-static condition, the soft ferritic phase showed large ductility, whereas the hard martensitic phase exhibited high strength but poor elongation due to its less ductile nature, as generally observed as martensite cracking at failure of DP steels (Ramazani *et al.*, 2016). These useful properties can be principally controlled by adjusting the microstructure characteristics like phase fraction, phase distribution and morphology. An increase of martensitic volume fraction and reduced grain size enhance strengthening, while elongation can be improved by increasing the amount of ferrite and homogeneous dispersion of second phases. Nevertheless, the deformation and fracture behaviour of DP steels under dynamic loading became much more complex and showed different mechanisms (Kim *et al.*, 2013; Wang *et al.*, 2013; Xu *et al.*, 2019). The effects of strain rate on mechanical properties of DP steel grades have been examined in several works (Kim *et al.*, 2013; Das *et al.*, 2017; Erice, Roth and Mohr, 2018; Xu *et al.*, 2019). It was reported that the flow stresses of DP steels with the strength level ranging from 600 to 1000 MPa were increased by increasing strain rates. Indeed, the strain rate sensitivities of these DP steels were different. The steels with higher amount of martensite obviously showed a lower strain rate sensitivity than those of steels with low martensitic phase fraction (Kim *et al.*, 2013; Wang *et al.*, 2013). The effects of strain rate on the ductilities of different steels could be rather varying. It was shown in (Yu, Guo and Lai, 2009; Wang *et al.*, 2013; Alturk *et al.*, 2017) that the ductility of ferritic CR5 mild steel and DP600 grade were decreased by increasing strain rate, while the elongation of DP1000 grade was clearly increased by higher strain rates. For example, the resulted mechanical properties of the DP steels grade 600 and 1000 were different at various strain rates, as illustrated in figure 1.5. The microstructure of

This material is reserved for educational use only, not allowed for commercial use.

Forbidden to modify the content, and cite the document when use.

AHS steels greatly affected their strengths, ductilities and thus crashworthiness performances.

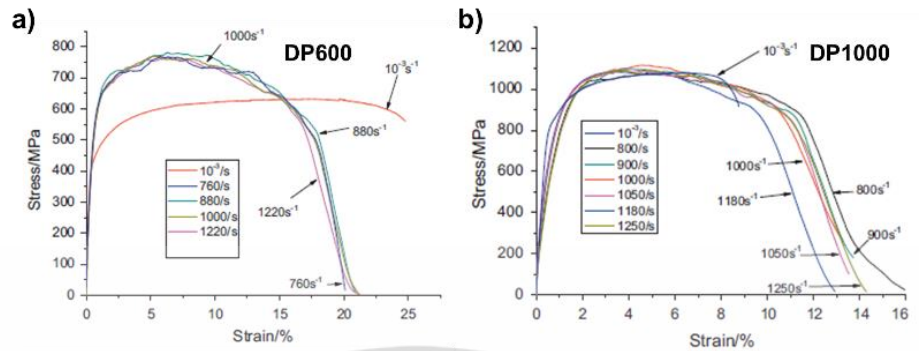


**Figure 1.5** The engineering stress-strain curves under static and dynamic tensile tests of the DP600 (a) and DP1000 (b).

Source: (Wang *et al.*, 2013)

Furthermore, mechanical behaviour of material from experiments can be described and analyzed by using finite element (FE) simulation. The FE method is a numerical method for solving mathematical physics and engineering problem which has been used to estimate the result of a differential equation that describes complex problem on mechanical behaviour such as plastic deformation. For example, (Qin *et al.*, 2013) applied FE simulation to predict strain field of DP steel during high strain rate deformation, as shown in figure 1.6.

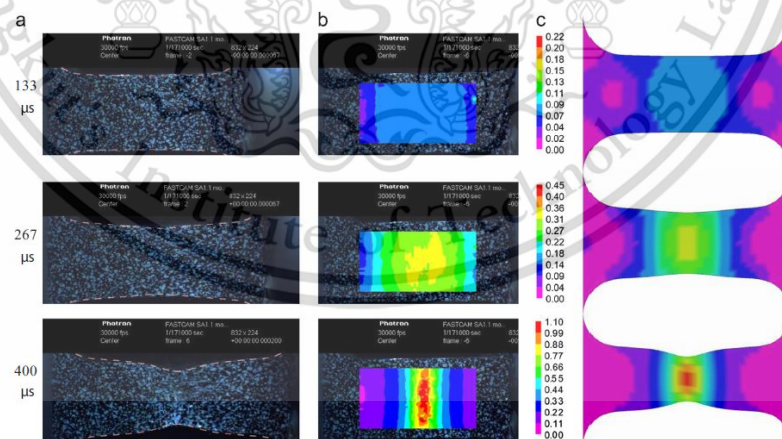


**Figure 1.6** Comparison for a representative test, DP500, at  $1110 \text{ s}^{-1}$ . (a) High speed images, wherein dashed lines are the edges of the specimen detected from (c). (b) The field of axial strain from DIC. The image in the background is always the reference image, while the color plots represent the deformed strain field. (c) The field of axial strain of the whole specimen from FE simulation.

Source: (Qin *et al.*, 2013)

This material is reserved for educational use only, not allowed for commercial use.

Forbidden to modify the content, and cite the document when use.

Note that DP steel is a multiphase steel which has ferritic-martensitic microstructure. The ferritic phase is soft and exhibits good elongation, while the martensitic phase is hard and contributes to strength of DP steels (Al-Abbasi and Nemes, 2003). During the plastic deformation of DP steels, these both phases have strong interactions on the microstructure level. Hence, a micro-scale based model is needed for characterizing the micromechanical behaviour of steel so that representative volume element (RVE) FE simulations were taken into account for investigated crashworthiness property of multiphase steel sheet, as shown in figure 1.7. Moreover, RVE simulations were employed for investigated the DP steel, as recommended by many literatures (Sun *et al.*, 2009; Sirinakorn, Uthaisangasuk and Srimanosawapal, 2014; Ramazani *et al.*, 2016; Srithananan, Kaewtatip and Uthaisangasuk, 2016; Darabi *et al.*, 2017). For example, (Ramazani *et al.*, 2016) applied 2D RVE model generated from real micrograph of the DP steel microstructure taken from light optical microscopy (LOM) for investigated micromechanical behaviour of the DP steel, as illustrated in figure 1.8. The generated flow curves of the both single ferritic and martensitic phases were based on a dislocation theory and chemical compositions of the examined DP steel for quasi-static deformation. Then, deformation microstructure of the DP steel was investigated by using RVE simulation, as demonstrated in figure 1.9. The Von Mises stress and equivalent plastic strain behaviour on micro-scale level were examined.

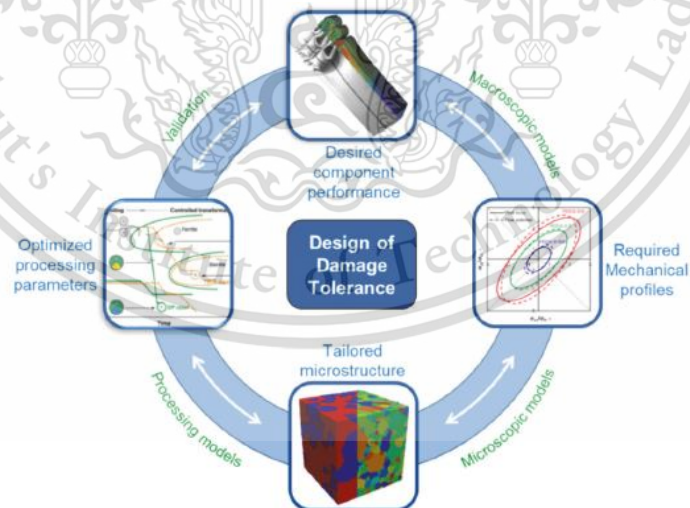


**Figure 1.7** The methodological flow of the multi-scale study on high strength steel sheets for the crashworthiness property across the component level, lab level and microstructure and process routines.

Source: (Liu *et al.*, 2018)

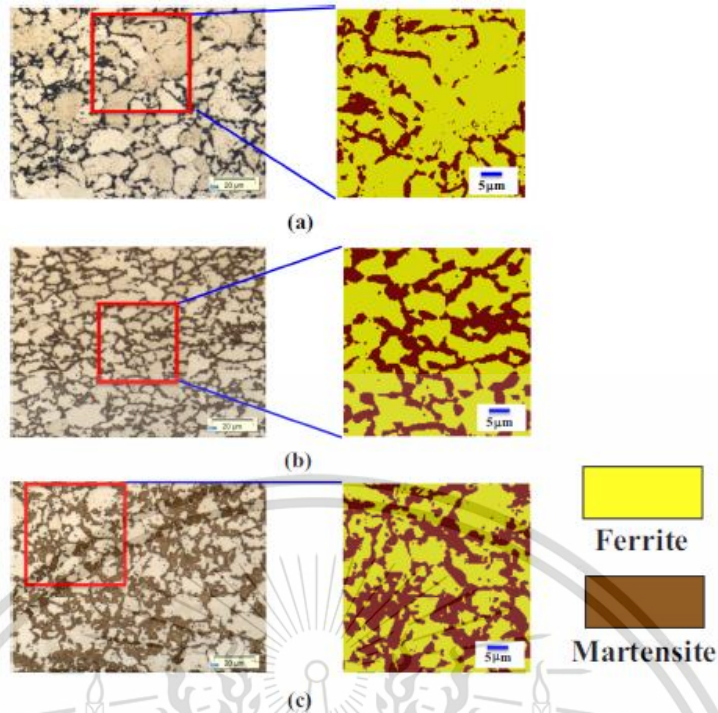


**Figure 1.8** Presentation of light optimal microscopic microstructures and the created RVEs (contained in the red boxes) for DP600 steels with different volume fractions of martensite: (a) 20% (RVE size is  $40\ \mu\text{m} \times 40\ \mu\text{m}$ ), (b) 37% (RVE size is  $32\ \mu\text{m} \times 32\ \mu\text{m}$ ) and (c) 46% (RVE size is  $40\ \mu\text{m} \times 40\ \mu\text{m}$ ).

Source: (Ramazani *et al.*, 2016)

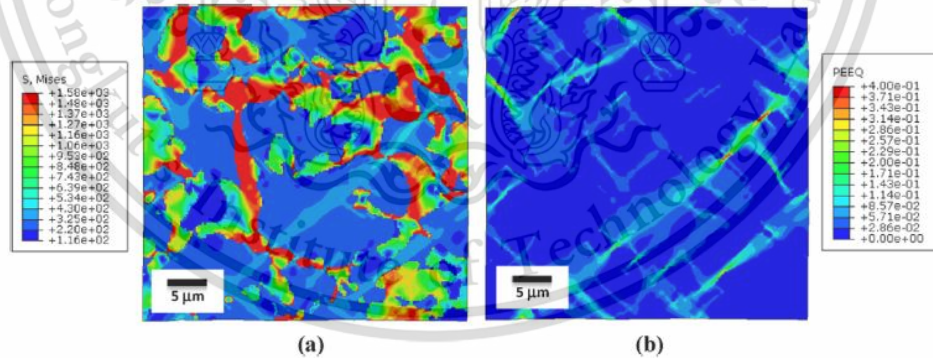


**Figure 1.9** Distribution of (a) Von Mises stress and (b) equivalent plastic strain in RVE of DP600 steel with 46% martensite after stretching.

Source: (Ramazani *et al.*, 2016)

However, the accuracy of finite element simulation results significantly depends on the used material models and their parameters. For describing plastic deformation at high strain rate of ductile materials such as steel, the Johnson-Cook (JC) constitutive model which is taken into account of plastic strain, strain rate and temperature effects, as This material is reserved for educational use only, not allowed for commercial use.

Forbidden to modify the content, and cite the document when use.

illustrated in figure 1.10, has been widely applied for predicting plastic deformation of ductile material under high strain rate loading (Johnson and Cook, 1983; Vedantam *et al.*, 2006; Yu, Guo and Lai, 2009; Qin *et al.*, 2013). For example (C.W. Isaac and O. Oluwole, 2015) applied the JC constitutive model for predicting dynamic crushing behaviour of square steel tubes using FE simulation, as demonstrated in figure 1.11.

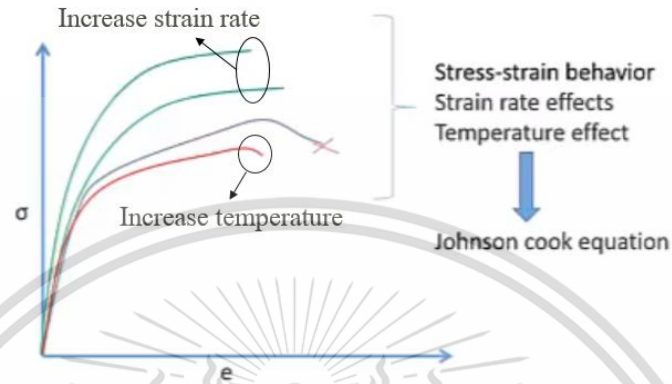


**Figure 1.10** Influence of Johnson-Cook constitutive model on stress and strain curve (Purple line is normal stress and strain curve, green line is stress and strain curve under high strain rates and red line is stress and strain curve under higher temperature).

Source: (Abaqus Acumen, 2017)

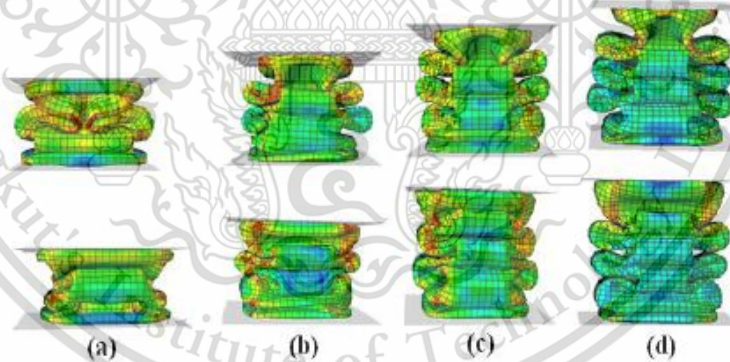


**Figure 1.11** Final collapsed mode of the present model with im-pacting velocity of 15m/s for two side views: (a) L=176mm (b) L=264mm (c) L=310mm and (d) L=350mm.

Source: (C.W. Isaac and O. Oluwole, 2015)

In (Erice, Roth and Mohr, 2018), effects of strain rate on ductile fracture initiation in AHS steel sheets were experimentally and numerically studied on a macro-scale. Various models based on accumulative damage mechanisms have been introduced as a fracture criterion. For example, the Gurson-Tvergaard-Needleman (GTN) model as a

This material is reserved for educational use only, not allowed for commercial use.

Forbidden to modify the content, and cite the document when use.

porous metal plasticity model was widely used to examine void growth mechanics and resulting ductile fracture of steels at high stress triaxiality state on both macro- and micro-level (Gurson, 1977; Uthaisangasuk, Prah and Bleck, 2008; Vajragupta *et al.*, 2012; Sirinakorn, Uthaisangasuk and Srimanosawapal, 2014). Besides, (Johnson and Cook, 1985) developed a fracture model taking into account the stress triaxiality, strain rate, and temperature. However, such model was restricted to fracture of bulk alloys due to void formation at high stress triaxiality. (Bao and Wierzbicki, 2004) carried out a series of tests on aluminum alloy grade 2024-T351 that covered a wide range of stress triaxiality. It was observed that the initiations of ductile fracture at negative and large triaxiality ranges were governed by different failure modes. For low stress triaxiality region, which basically occurred in sheet metal, failure could occur as a combination of shear fracture and void growth. Afterwards, (Bai and Wierzbicki, 2008) introduced a metal plasticity and fracture model which incorporated the hydrostatic pressure and third deviatoric stress invariant or Lode angle parameter. For the determination of damage locus based on such model, (Charoensuk, Panich and Uthaisangasuk, 2017) performed tensile tests of sheet samples having different shapes in combination with a digital image correlation (DIC) technique and FE simulations. DIC technique was applied with FE simulation to collect both stress triaxiality and equivalent plastic strain from the experimental testing to generate damage locus, as illustrated in figure 1.12. The example of resulted damage locus of DP steel grade 980 is shown in figure 1.13.

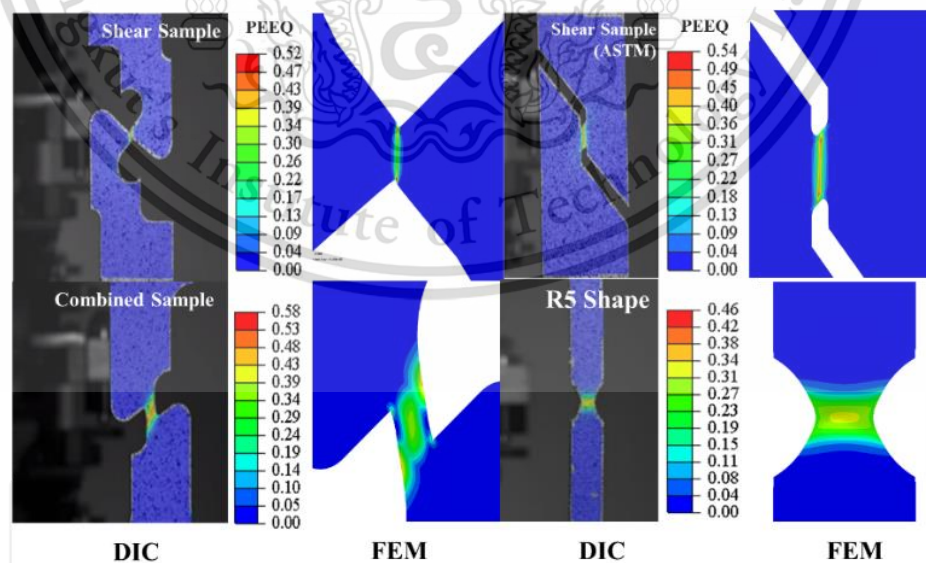


**Figure 1.12** Determined equivalent plastic strain from DIC and stress triaxiality from FEM values of specimens.

Source: (Charoensuk, Panich and Uthaisangasuk, 2017)

This material is reserved for educational use only, not allowed for commercial use.

Forbidden to modify the content, and cite the document when use.

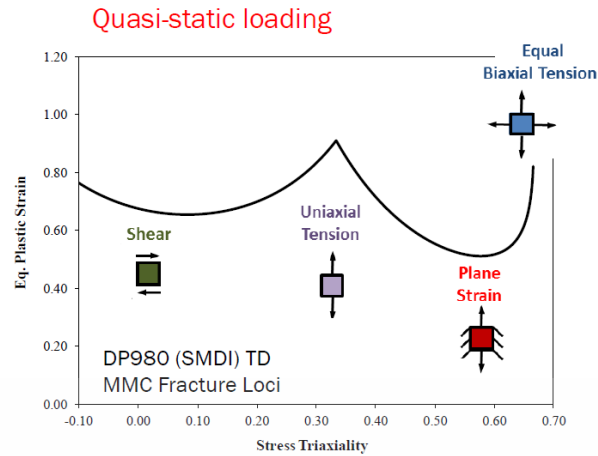


**Figure 1.13** The resulted obtaining fracture locus of steel DP980 (Transverse direction).

Source: (Michael Worswick, 2018)

For application of damage curve, the applied damage curve with RVE simulations for two-phase boron steel at quasi-static condition was conducted (Srithananan, Kaewtatip and Uthaisangsuk, 2016), then the damage locus was applied to FE 2D RVE simulations of a martensite-bainite mixture to predict damage initiation under various states of stress on micro-scale, as shown in figure 1.14, in which the obtained damage curves were individually applied for each phase. However, the modeling of most previous works was done on the macro-scale or under quasi-static deformation. Additionally, deformation and fracture mechanism on the microstructure level of DP steel at elevated strain rates were merely studied by experimental observations.

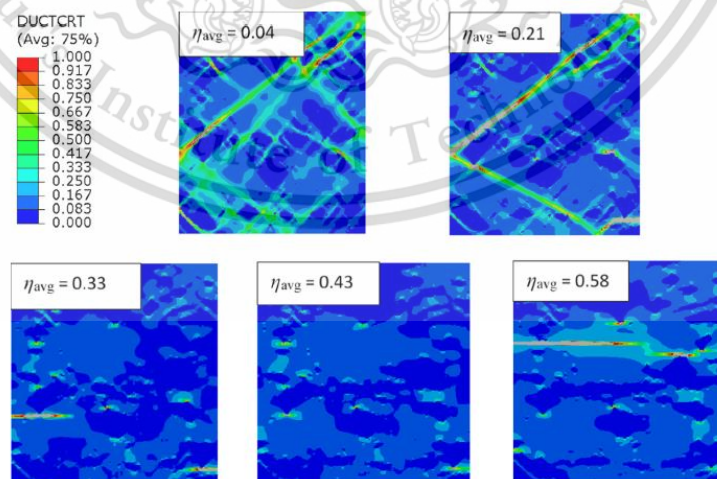


**Figure 1.14** Calculated ductile damage initiation of RVE under various stress triaxiality for the 20:80 Martensitic/bainite microstructure.

Source: (Srithananan, Kaewtatip and Uthaisangsuk, 2016)

This material is reserved for educational use only, not allowed for commercial use.

Forbidden to modify the content, and cite the document when use.

Therefore, the present work aimed to better describing the dynamic deformation behavior of DP steel grades 780 and 1000 by applying a micromechanical modeling. First, tensile tests at different strain rates were performed for the examined steels. Then, crack development and fracture surface of samples after the tests were investigated by scanning electron microscope (SEM) analysis. RVE simulations were carried out for the DP steels subjected to uniaxial tension at varying strain rates. Flow curves of the individual phases were defined on the basis of a dislocation theory and local chemical compositions. Hereby, the JC strain rate-dependent hardening model was taken into account, for which model parameters were identified according to the experimental tensile properties and results from literatures. Furthermore, the JC rate-dependent damage model was also applied for the single phases of examined steels. For martensite, damage curves were determined from quenched carbon steels with similar carbon contents, while those of ferrite were adapted from the previous work. Afterwards, the resulting local deformations and crack occurrences in the microstructure of investigated DP steels under high strain rates were predicted by RVE simulations and discussed.

## **1.2 Research Objectives**

1. To study deformation and damage behaviour of high strength steel under high strain rate deformation on the microstructure level.
2. To apply RVE model to predict strain rate-dependent behaviour of high strength steel.

## **1.3 Scopes of Work**

1. The as-received high strength steel sheet grade 780 and 1000 were selected for investigation.
2. Initial microstructure of the DP steels were observed by using LOM and SEM.
3. Universal tensile testing machine was employed for quasi-static and medium strain rate tensile testing.
4. The split-Hopkinson pressure bar was applied for high strain rate tensile testing.

This material is reserved for educational use only, not allowed for commercial use.

Forbidden to modify the content, and cite the document when use.

5. Microstructure deformation and fracture surface after tests were examined by SEM and image analysis.
6. 2D RVE were generated on the basis of a random area two-phase microstructure of examined DP steel taken from a light optical microscopy by using In-house software.
7. FE RVE model was applied for investigated effect of microstructure by using Abaqus/explicit software.
8. Flow curve of single phases were defined as the basis of dislocation-density based strain hardening model in combination with the JC strain rate hardening model.
9. Damage curve in combination with JC rate-dependent damage model was applied to RVE simulation for damage analysis of microstructure deformation and micromechanical properties at different strain rates.
10. Discussions and conclusions of resulted experiments and FE RVE simulations.

#### **1.4 Expected Benefits**

1. Better understanding the effects of strain rates on mechanical and failure behaviour of high strength steels taking into account microstructure characteristics
2. Obtaining a micromechanical modelling approach for predicting deformation behaviour of high strength steels under different strain rates on both macro and micro-scale.
3. Improving the prediction accuracy of material behaviour under high strain rate condition for the automotive design.

## CHAPTER 2

### THEORETICAL FUNDAMENTS

#### 2.1 Advanced high strength steel

The family of advanced high strength steel (AHSS) continues to grow and evolve. Many grades of AHSS have been developed to meet the unique and varied performance requirements of many components of vehicle (Lahaije and Sikora, 2014). The AHSS family includes Dual Phase (DP), Complex Phase (CP), Martensitic (MS), Transformation-Induced Plasticity (TRIP), Hot-Formed (HF), and Twinning-Induced Plasticity (TWIP) (Hall, 2011). These AHSS grades are uniquely qualified to meet the functional performance demands of certain parts. Each type may be tailored to have a specific set of characteristics from a broad range of possibilities. These steels, while improving the strength and safety of cars on the road today, also offer flexibility for automotive engineers who seek to design novel, light-weight solutions (Morgans, 2013). Increasingly selected for application in vehicles to address challenges faced by automakers, AHSS can help improve safety, fuel efficiency, manufacturability, durability, and quality, while minimizing the lifetime greenhouse gas emissions from production, use, and end-of-life phases of the vehicle. AHSS also remain an economical choice in the highly competitive automotive industry. Additionally, figure 2.1 shows the details of AHSS compared to other steels.

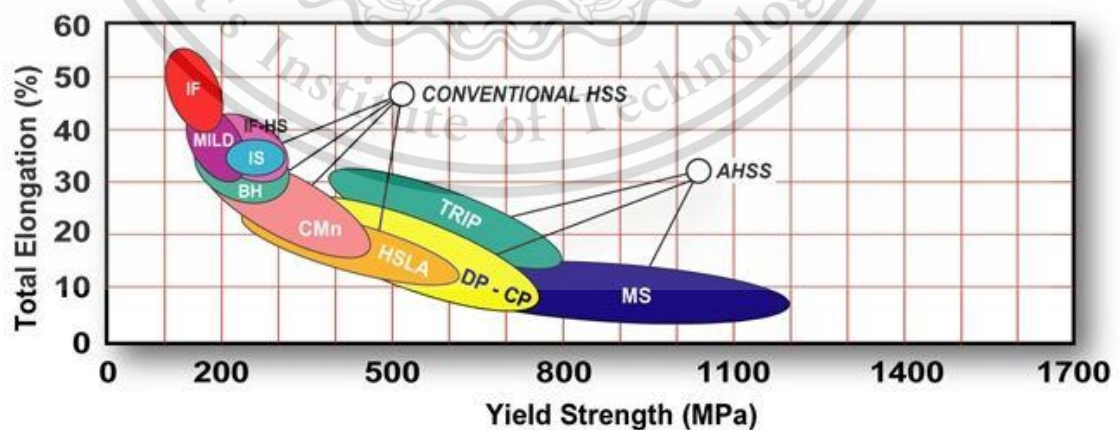


**Figure 2.1** Typical steels classified by mechanical properties.

Source: (Msynk, 2014)

This material is reserved for educational use only, not allowed for commercial use.

Forbidden to modify the content, and cite the document when use.

## 2.2 Dual phase steel

The term DP steel, refers to a class of AHSS which is composed of two phases namely a purely ferrite matrix and a dispersed martensite second phase. DP steels have high ultimate tensile strength, enabled by the martensite combined with low initial yielding stress, high early-stage strain hardening and macroscopically homogeneous plastic flow (Chakraborti and Mitra, 2007). These features render DP steels ideal materials for automotive-related sheet forming operations. Their advantages are such as low yield strength, low yield to tensile strength ratio, high initial strain hardening rates, good uniform elongation and good fatigue resistance. Due to these properties DP steels are often used for automotive body parts (Fallahi, 2002; Morgans, 2013), as shown in figure 2.2.

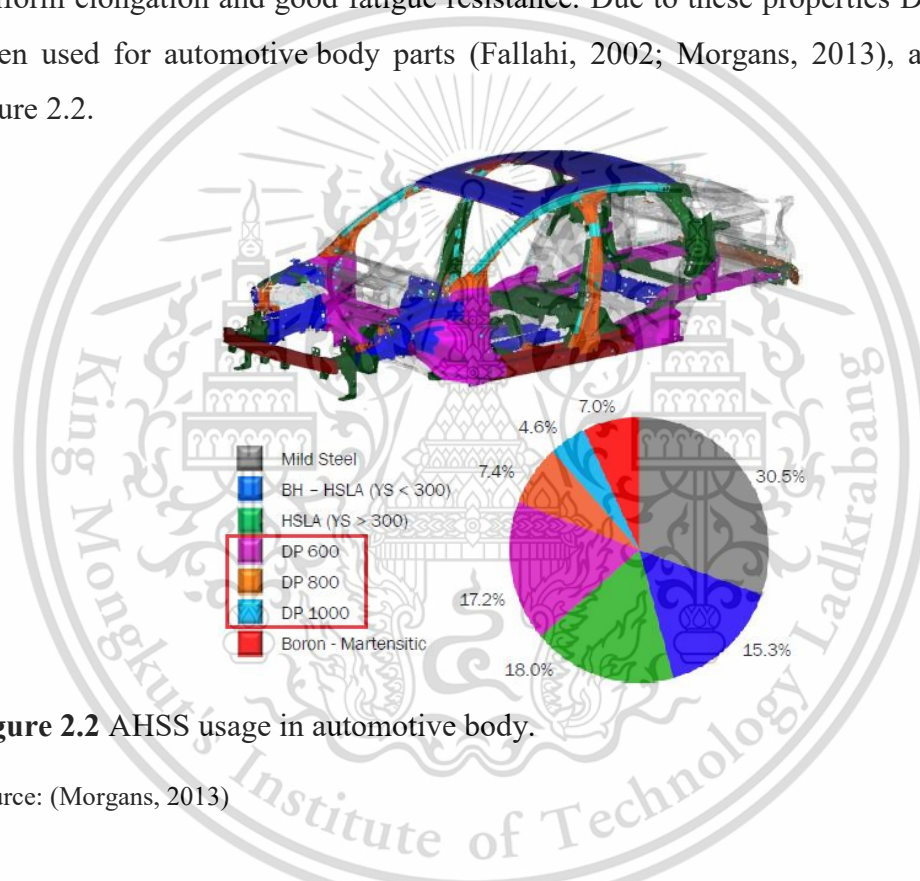


**Figure 2.2** AHSS usage in automotive body.

Source: (Morgans, 2013)

### 2.2.1 Microstructure and mechanical properties of dual phase steel

DP steel is a high-strength steel that has a ferritic-martensitic microstructure, as illustrated in figure 2.3. Mechanical properties of ferritic phase is soft and good elongation, whereas those of martensitic phase is hard and brittle. Consequently, DP steel provides the advantage of both microstructures in which strength and ductility of those phases are properly combined. The dual phase microstructure is commonly obtained through heat treatments. Continuous annealing and hot rolling processes can be used to obtain the DP microstructure (Dzupon *et al.*, 2007). The excellent mechanical

This material is reserved for educational use only, not allowed for commercial use.

Forbidden to modify the content, and cite the document when use.

properties of DP steels can be attributed to the mixing of a ductile ferritic phase with the stronger more brittle martensitic phase. Under quasi-static load, the mechanical properties of DP steels are dependent on both grain size of ferrite and volume fraction of martensite within the microstructure. For example, (Sodjit and Uthaisangsuk, 2012) demonstrated that flow stress of the ferritic-martensitic DP steels by tensile tests were increased with increase of martensite content, as shown figure 2.4. The grade of DP steel such as grade DP600 and DP800 are related to its on strength and martensite content. Besides, (Sodjit and Uthaisangsuk, 2012) reported that the composition and hardness of the martensitic phase of DP steel did not significantly affect the overall mechanical properties of the material.

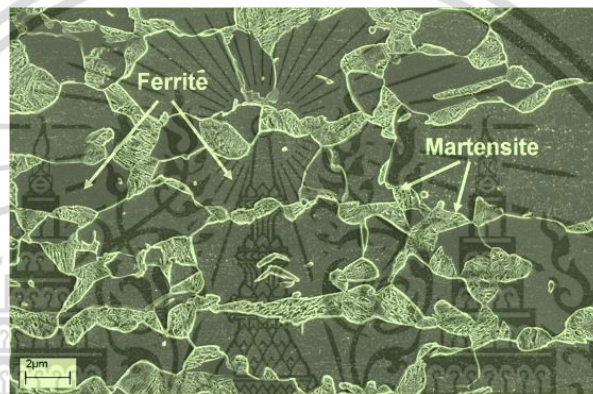


**Figure 2.3** Typical ferritic-martensitic microstructure of DP steel.

Source: (Satyendra, 2014)

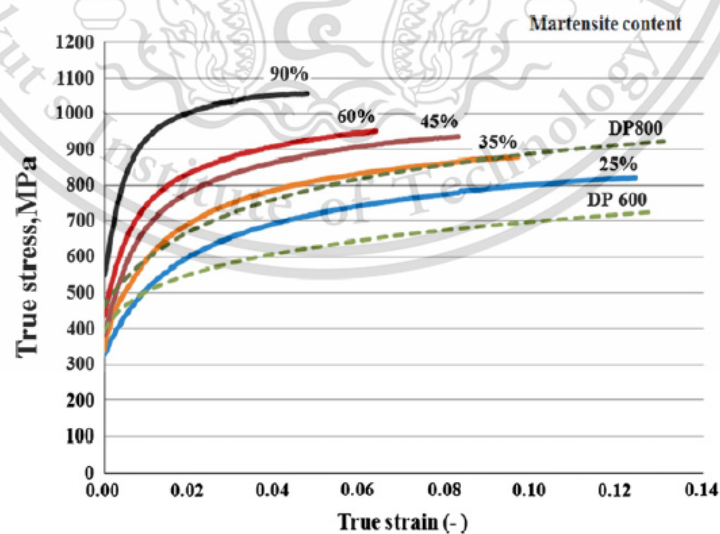


**Figure 2.4** Quasi-static flow stress behaviour of DP steel with different martensite volume fraction.

Source: (Sodjit and Uthaisangsuk, 2012)

This material is reserved for educational use only, not allowed for commercial use.

Forbidden to modify the content, and cite the document when use.

To investigate mechanical properties of DP steel at high strain rate, (Das *et al.*, 2017) studied the DP steel grades 600 and 800 having martensite contents of 10.2% and 33.2%, respectively. It was found that the yield and ultimate tensile strength of both DP steels were higher while increased strain rates, while uniform elongation of two investigated steels were decreased, as demonstrated in figure 2.5.

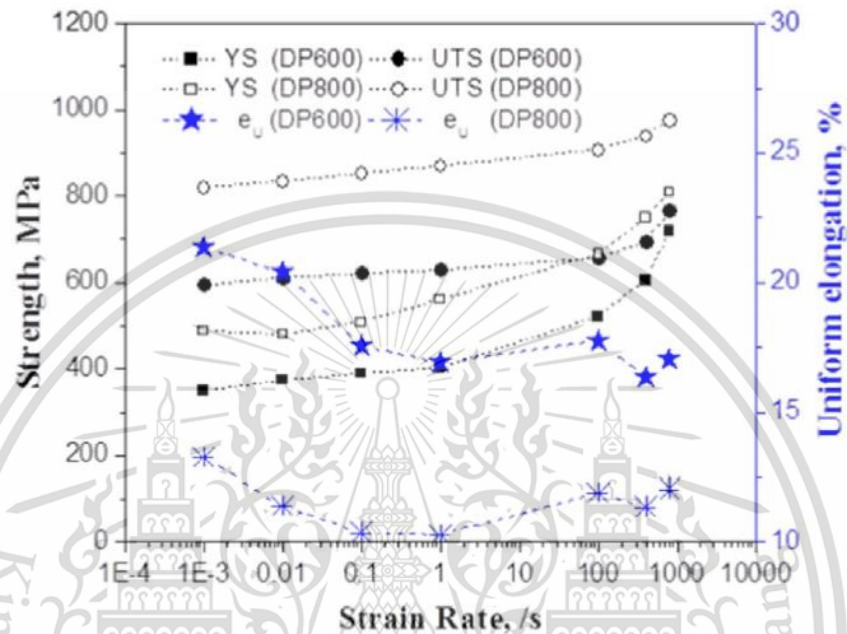


**Figure 2.5** Variation in yield strength, ultimate tensile strength and uniform elongation for DP600 and DP800 at different strain rates.

Source: (Das *et al.*, 2017)

In addition, (Hengjun *et al.*, 2018) examined the strain rate dependence of DP steel grade 800 by tensile tests at different strain rates and TEM observation. From the mechanical testing, it is seen that both yield strength and ultimate tensile strength of DP steel was increased by enhanced strain rate. Then, TEM observations of failed DP steel specimen under quasi-static and high strain rate tests were carried out and the results are illustrated in figure 2.6. Figure 2.6(a,b) and Figure 2.6(c,d) presented ferrite structure and martensite lath structure after corresponding tests, respectively. Dislocations were produced both interior and the boundary of ferritic grain as increasing strain rate. Moreover, dislocation density on the boundaries of the phases was much higher in the centre of sample from high strain rate test. On the other hand, martensite lath obviously exhibited no change of dislocation density under different strain rates, while quantities of dislocations in ferrite grain were much increased with increasing strain rate.

This material is reserved for educational use only, not allowed for commercial use.

Forbidden to modify the content, and cite the document when use.

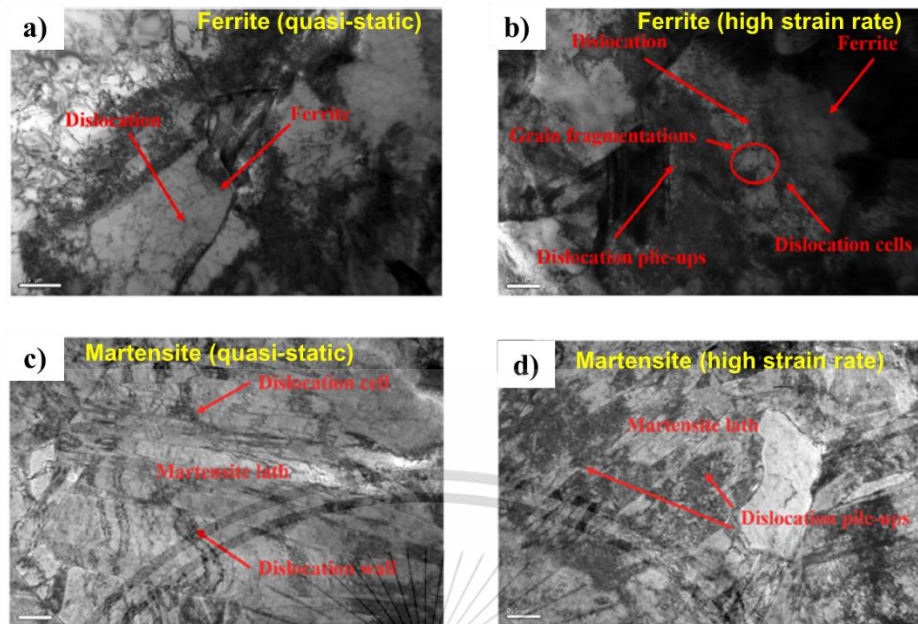


**Figure 2.6** TEM images of ferrite structures (a,b) and martensite lath structures (c,d). (a,c) quasi-static  $\sim 10^{-4} \text{ s}^{-1}$  and (b,d) high strain rate  $\sim 10^3 \text{ s}^{-1}$ .

Source: (Hengjun *et al.*, 2018)

## 2.2.2 Fracture behaviour of dual phase steel

Fracture behaviour of metal can be divided into two main mechanisms those are ductile fracture and cleavage fracture (Anderson, 2005). The flow stress behaviour of ductile material is not linear and includes both elastic and plastic, while the relationship of stress and strain of brittle material is linearly until occurred cleavage fracture, as illustrated in figure 2.7.

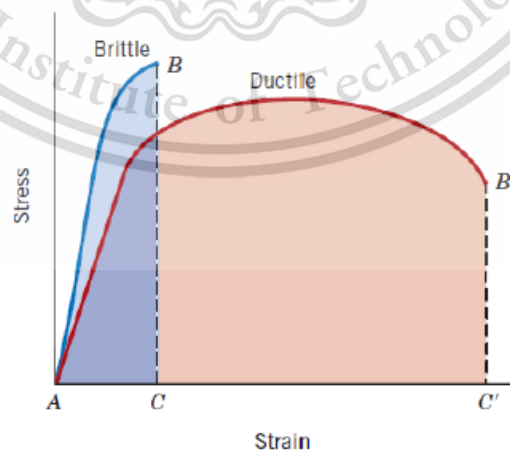


**Figure 2.7** Typical stress-strain curves of brittle and ductile materials.

Source: (Anderson, 2005)

This material is reserved for educational use only, not allowed for commercial use.

Forbidden to modify the content, and cite the document when use.

The DP steel is a low carbon steel type which shows multiphase microstructure consisted of soft ferritic matrix and hard martensitic island. Under quasi-static deformation of DP microstructure, the soft ferritic phase exhibited good ductility and ductile fracture, while hard martensitic phase had high strength but poor elongation ability due to cleavage fracture occurrence (martensite cracking) (Ramazani *et al.*, 2016). The typical dimple and cleavage fracture of the DP steel observed by SEM are illustrated in figure 2.8 (Xu *et al.*, 2019). The result showed that the DP steel clearly showed two fracture mechanisms both dimple and cleavage fracture.

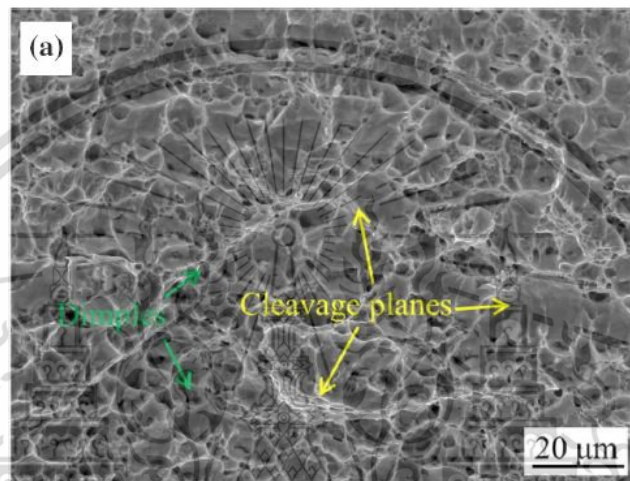


**Figure 2.8** Fracture surface of DP1000 steel after a quasi-static deformation.

Source: (Xu *et al.*, 2019)

### 2.3 Mechanical testing machine types

In principle, any testing machine which can apply a uniaxial tensile load to sheet steel specimen until failure with a specified high strain rate can be used to conduct the dynamic tensile test. The load can be a constant load for a period of time, or an instant load wave used for high strain rate. The machine should also have the proper measurement systems to measure and record the important parameters, such as strain, displacement and load. In general, the strain rate region of interest for vehicle crash behaviour can be classified to quasi-static, medium strain rate and high strain rate condition, as shown in figure 2.9. Thus, at least three types of testing systems are required. For testing at quasi-static condition or strain rates below  $0.1 \text{ s}^{-1}$ , a conventional load frame, either mechanical or servo-hydraulic, should be used. For strain rates higher than  $0.1 \text{ s}^{-1}$ , both servo-hydraulic and bar type machines should be used. The servo-hydraulic type system can normally cover the strain rate range of  $0.1$  to  $500 \text{ s}^{-1}$ , while

bar type system covers the strain rates 500 to 1000 s<sup>-1</sup> and higher. The strain rate increments 1, 10, 100, 250, 500 1000 s<sup>-1</sup> are sufficient for describing the strain rate sensitivity of steels materials. Figure 2.10 is a schematic representation of the applicable range of strain rates for the three testing systems.

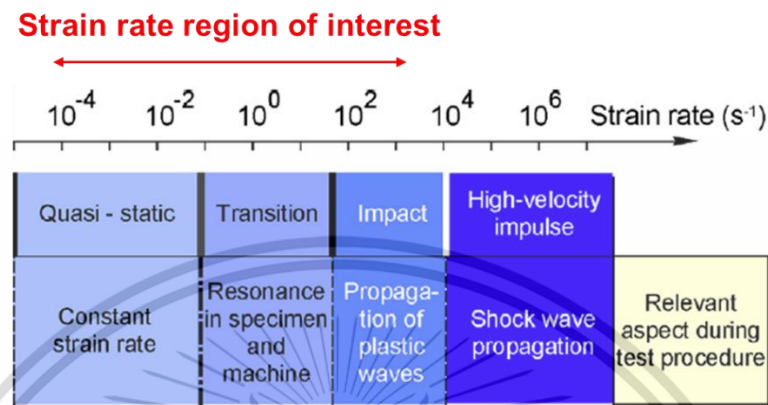


**Figure 2.9** The level of strain rate in mechanical tests.

Source: (Bruschi *et al.*, 2014)

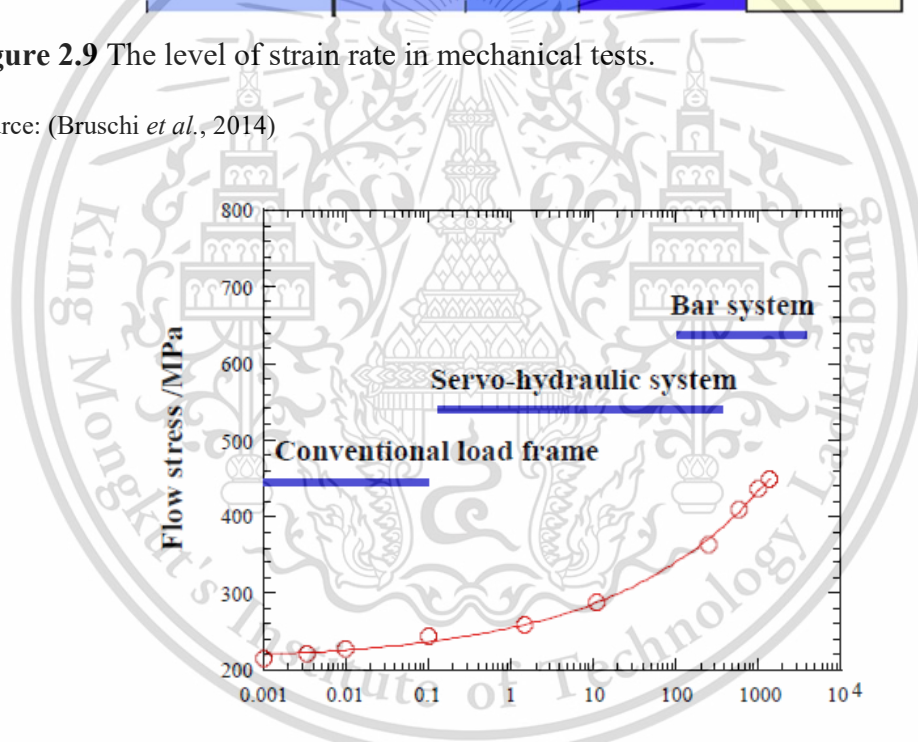


**Figure 2.10** Typical ranges of strain rate covered by conventional load frames, servo-hydraulic machines and bar testing systems and accordingly flow stress for typical steel.

Source: (Borsutzki and Opbroek, 2005)

### 2.3.1 Universal testing machine

The conventional load frame and servo-hydraulic systems can be grouped in the universal testing machine. The material tensile testing at quasi-static load and medium strain rate are performed by using universal testing machine to determine mechanical

This material is reserved for educational use only, not allowed for commercial use.

Forbidden to modify the content, and cite the document when use.

properties of material. The machine is controlled by velocity which can be assigned in millimeter per second. The universal testing machine can record the force ( $F$ ), time ( $t$ ), and displacement ( $u$ ). Then, the mechanical properties of tested material is generally described by the stress-strain diagram. The engineering stress-strain curve can be calculated using the equations (2.1) and (2.2). Additionally, the engineering strain rate is computed with the equation (2.3).

$$\sigma_s = \frac{F}{A_s}, \quad (2.1)$$

$$\varepsilon_s = \frac{u}{L_s}, \quad (2.2)$$

$$\dot{\varepsilon}_s = \frac{\dot{u}}{L_s} \quad (2.3)$$

Where

$\sigma_s$  = engineering stress of specimen

$F$  = force

$A_s$  = the cross sectional area of specimen

$\varepsilon_s$  = engineering strain of specimen

$u$  = displacement

$L_s$  = gauge length of specimen

$\dot{\varepsilon}_s$  = engineering strain rate of specimen

$\dot{u}$  = velocity

### 2.3.2 Split-Hopkinson tensile bar

Currently, dynamic testing of material is becoming more important due to more need of analysis and optimization of crashworthiness and impact performance. The split Hopkinson pressure bar is the classical experimental technique applied for determining the mechanical properties under dynamic loading. Moreover, several researchers have shown that split Hopkinson tensile bar (SHTB) can be applied to study at high strain rate of material properties and provide more reliable data than other testing machines. This material is reserved for educational use only, not allowed for commercial use.

Forbidden to modify the content, and cite the document when use.

(Wang and Xu, 2006; Chen *et al.*, 2011; Rahmaan *et al.*, 2016). A schematic of the SHTB apparatus is provided in Figure 2.11, and its photograph is shown in Figure 2.12.

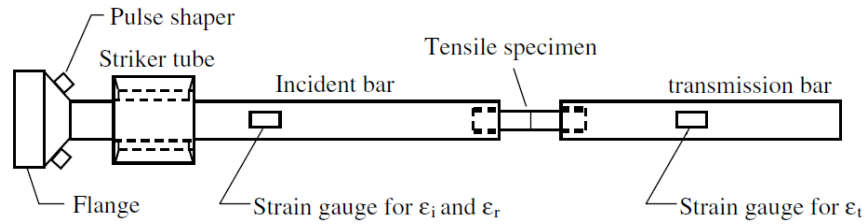


**Figure 2.11** Schematic diagram of the split-Hopkinson tensile bar apparatus.

Source: (Wang and Xu, 2006)

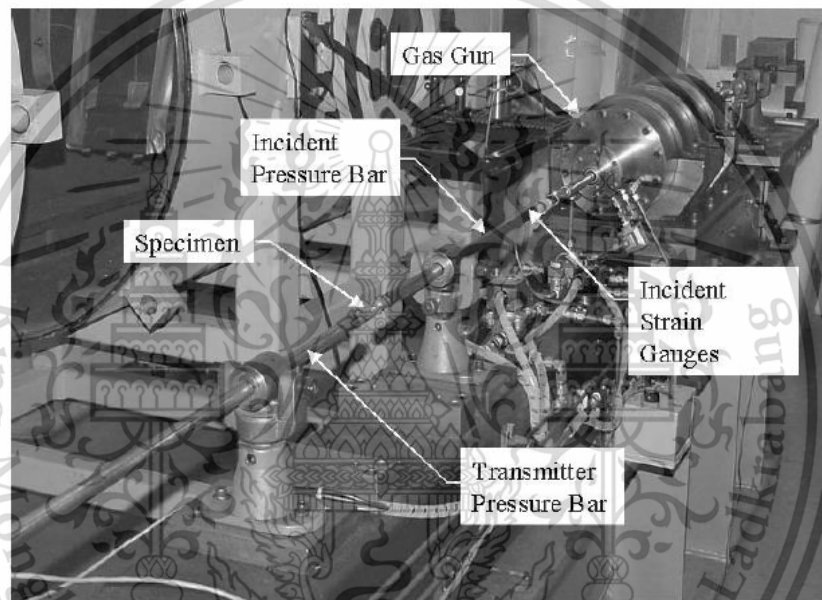


**Figure 2.12** The split-Hopkinson tensile bar apparatus.

Source: (Salisbury and Worswick, 2007)

The SHTB is based on the principle of one dimensional wave propagation. Its main components are gas gun, striker bar, incident bar and transmission bar. The striker bar sits in the barrel at the gas gun chamber. The incident bar and transmission bar are made of same material and same cross-section area. At all times during the test the striker, incident and transmission bar should remain elastic. The sample to be tested is sandwiched between the incident and transmission bar. The striker bar is propelled by gas pressure towards velocity direction ( $V_0$ ), as illustrated in figure 2.13.

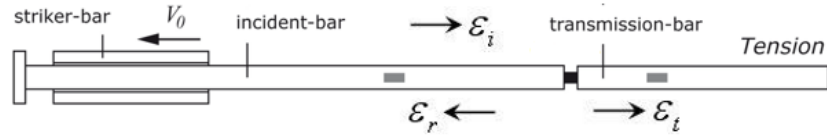


**Figure 2.13** Velocity direction of striker bar and wave propagation direction in the split-Hopkinson tensile bar system.

Source: (Luciano Avilla Gray, 2013)

During high strain rate tensile testing, an elastic tension wave propagates up the incident bar toward the sample, namely, incident pulse ( $\epsilon_i$ ). On reaching the sample, repeated wave propagation within it deforms the sample plastically. Part of the wave goes through to the transmission bar, namely, transmitted pulse ( $\epsilon_t$ ) and part is reflected back into the incident bar that is reflected pulse ( $\epsilon_r$ ), each of which is picked up by the strain gauges mounted on the corresponding bars. The typical wave shapes of SHTB test, recorded by strain gauges, is illustrated in figure 2.14. The strain gauges on each bar are mounted to measure the axial strain. The elastic strain generated in the incident and transmission bar are used to calculate the stress-strain of the sample. Additionally, the specimen is sheet, a particular adapter is designed to clamp the specimen to the loading bar by using pin, as shown in figure 2.15. The engineering stress, engineering strain and strain rate are calculated based on the one-dimensional stress wave theory by the following equations (Chen *et al.*, 2011; Qin *et al.*, 2013):

$$\sigma_s = \frac{A_b}{A_s} E_b \epsilon_t \quad (2.4)$$

$$\epsilon_s = -2 \frac{c_b}{L_s} \int_0^t \epsilon_r dt \quad (2.5)$$

$$\dot{\epsilon}_s = -2 \frac{c_b}{L_s} \dot{\epsilon}_r \quad (2.6)$$

Where  $E_b$  = elastic modulus of bars  
 $A_b$  = cross sectional area of bars

This material is reserved for educational use only, not allowed for commercial use.

Forbidden to modify the content, and cite the document when use.

$\varepsilon_t$  = transmitted strain

$c_b$  = velocity of stress wave through the bars

$\varepsilon_r$  = reflected strain

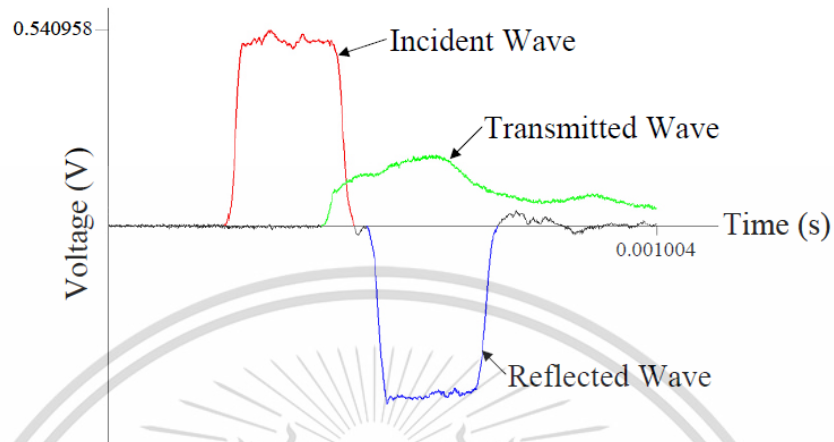


**Figure 2.14** Typical forms of waves acquired from strain gauges.

Source: (Smerd, 2005)

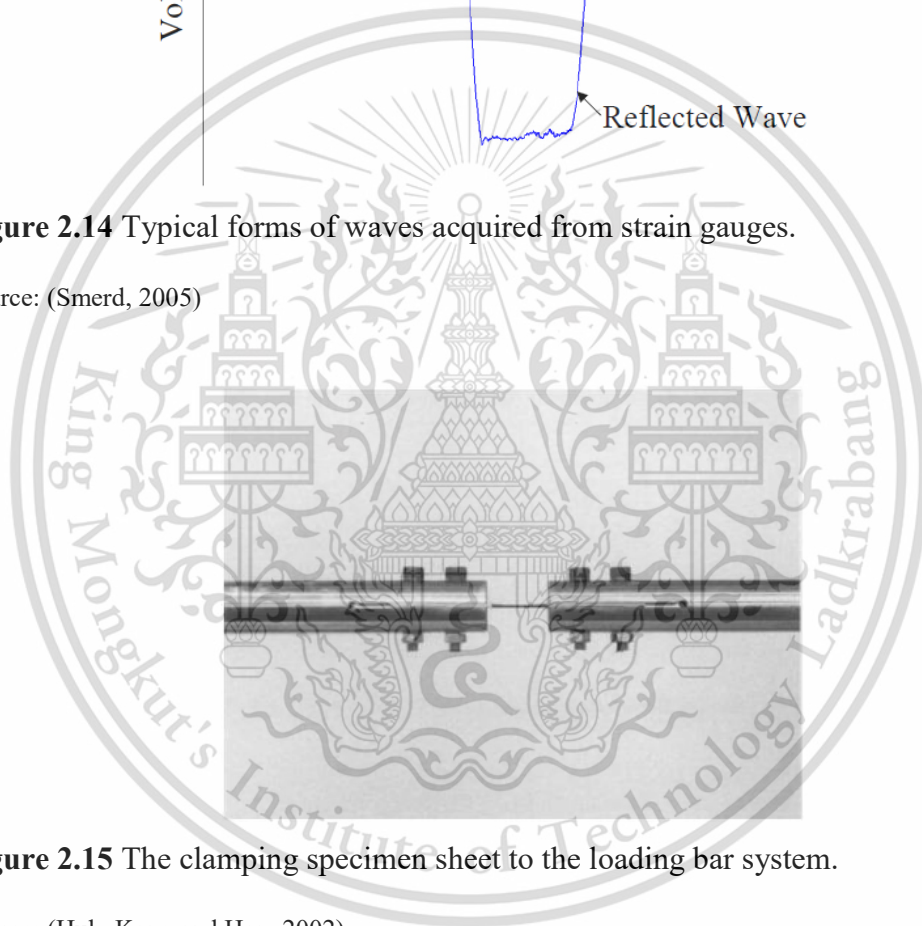


**Figure 2.15** The clamping specimen sheet to the loading bar system.

Source: (Huh, Kang and Han, 2002)

## 2.4 Flow curve model

The flow curve model or flow stress model is a mathematical model that relates flow stress to parameters such as chemical composition, phase constitution and grain size for predicting mechanical quasi-static behaviour of material as a function of plastic strain. Moreover, flow curve model can be defined as the instant value of stress required to continue plastic deformation of material. Many authors have shown that flow curve model represents the material characteristic required for commercial finite element

This material is reserved for educational use only, not allowed for commercial use.

Forbidden to modify the content, and cite the document when use.

software to simulate mechanical behaviour of material during obtaining loading (Uthaisangasuk, Prahl and Bleck, 2008; Vajragupta *et al.*, 2012; Ramazani *et al.*, 2016).

#### 2.4.1 Macroscopic flow curve model

Macroscopic flow curve model is an empirical or physical model employed to describe the progression of flow stress behaviour on the macro-scale. Several flow curve models are available to extrapolate strain hardening of material subjected to tensile test under quasi-static loading at room temperature, as shown in figure 2.16.

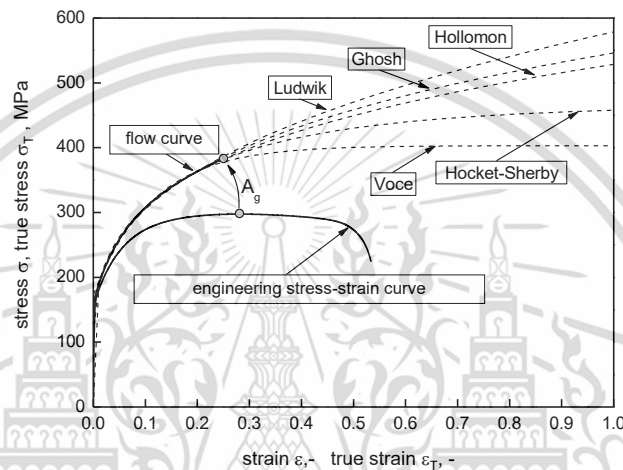


**Figure 2.16** Comparison of models for quasi-static flow curve extrapolation.

Source: (Münstermann and Bleck, 2009)

#### 2.4.2 Single phase flow curve model

In this work, effective isotropic formulations for the flow stress behaviours of each individual phases were assumed using the von Mises equivalent plastic material law. The constitutive models of the flow curves are the function of the chemical composition of material, microstructural characteristics and thermal processing. The local carbon content was an important factor to incorporate. In general, the plastic deformation behaviour of ductile metal can be described by the shear stress on the current microstructural state ( $\tau$ ). This micromechanical shear stress is a function of the micromechanical strain rate ( $\dot{\gamma}$ ), the temperature ( $T$ ), and the local dislocation density ( $\rho$ ). According to the Mecking–Kocks theory, the evolution of the dislocation density with deformation is the result of the competition between the rate of production of dislocation and the annihilation rate of dislocation. This relation can be expressed as (Bouquerel, Verbeken and De Cooman, 2006):

This material is reserved for educational use only, not allowed for commercial use.

Forbidden to modify the content, and cite the document when use.

$$\frac{d\rho}{Md\varepsilon} = \frac{1}{\lambda b} + \frac{k}{b} \sqrt{\rho} - f\rho \quad (2.7)$$

Where  $M$  is the Taylor factor,  $b$  is the magnitude of the Burgers vector.  $k$  and  $f$  are fitting parameters, and  $\lambda$  is the grain diameter. This concept was further developed for the ferritic and martensitic phase. Then, modified flow curve model of single phases, ferrite and martensite can be expressed as (Sirinakorn, Wongwiset and Uthaisangskul, 2014; Ramazani *et al.*, 2016):

$$\sigma(\text{MPa}) = \sigma_0 + \Delta\sigma + \alpha M \mu \sqrt{b} \sqrt{\frac{1 - \exp(-Mk_r \varepsilon)}{k_r L}} \quad (2.8)$$

Where  $\alpha$  is material constant,  $\mu$  is the shear modulus,  $L$  is the dislocation mean free path,  $\sigma_0$  is the Peierls stress and effects of alloying elements in the solid solution and  $\Delta\sigma$  is strengthening by carbon in solution. An example of generated single phase flow curve of the ferritic-martensitic DP steel for both ferritic and martensitic phase were illustrated in figure 2.17. From the results, single phase flow curve of ferrite was softer, while martensite was harder as followed by the dislocation density equation (Bouquerel, Verbeke and De Cooman, 2006).

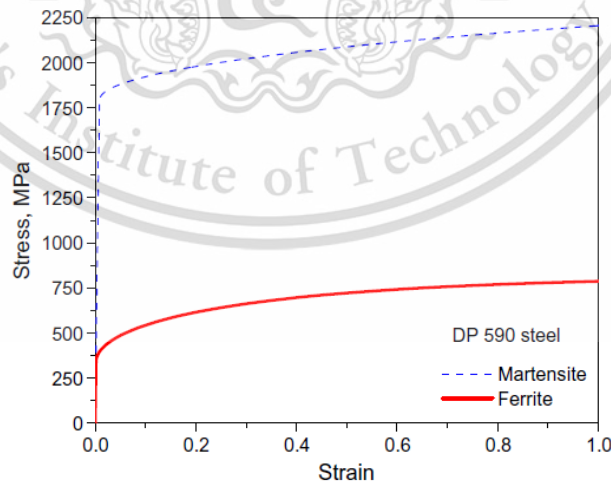


**Figure 2.17** The generated single phase flow curves of ferrite and martensite in DP590 steel.

Source: (Paul, 2013)

This material is reserved for educational use only, not allowed for commercial use.

Forbidden to modify the content, and cite the document when use.

### 2.4.3 Dynamic flow curve model

Dynamic behaviour of material often involves high strain rate behaviour. Thus, the dynamic flow curve model takes into account involved plastic strain, strain rate and temperature. (Johnson and Cook, 1983) proposed constitutive model to describe relationship between equivalent stress and influence factors including equivalent plastic strain, strain rate and temperature. The Johnson-Cook (JC) constitutive model is an empirical model given stress in a function of strain which is expressed as:

$$\sigma[\varepsilon, \dot{\varepsilon}, T] = [A + B\varepsilon^n][1 + C \ln(\frac{\dot{\varepsilon}}{\dot{\varepsilon}_0})][1 - T^m] \quad (2.9)$$

Where

$A$  = yield stress

$B$  = hardening modulus

$n$  = hardening exponent

$C$  = strain rate coefficient

$\dot{\varepsilon}$  = strain rate

$\dot{\varepsilon}_0$  = reference strain rate

$T$  = Temperature function

$m$  = Temperature coefficient

(Singh *et al.*, 2011; Qin *et al.*, 2013) recommended, determined the five Johnson-Cook material constants are  $A$ ,  $B$ ,  $C$ ,  $n$  and  $m$ . They could be calculated by a fitting method. Firstly, the  $A$ ,  $B$ , and  $n$  parameters can be obtain by quasi-static testing at room temperature.  $A$  represents the true yield stress of material at a strain rate of  $0.001 \text{ s}^{-1}$  which is equal to the stress corresponding to 0.2% offset strain,  $B$  and  $n$  are determined by curve fitting in the plastic zone from the true flow stress at 1% offset strain to the point of uniform elongation at strain rate  $0.001 \text{ s}^{-1}$ . Otherwise, the  $C$  parameter can be obtained by a dynamic testing at room temperature. The strain rate sensitivity parameter  $C$  is determined as the slope of the linear fit of natural logarithm of strain rate versus the ratio of dynamic true flow stress at 1% offset plastic strain to that of quasi-static. Finally, the  $m$  parameter can be obtained by the quasi-static test at different temperature. For example, (Qin *et al.*, 2013) generated and applied the JC constitutive model for predicting stress-strain behaviour of DP500 at different strain rates in which the predicted flow curves by JC constitutive model and obtained by

This material is reserved for educational use only, not allowed for commercial use.

Forbidden to modify the content, and cite the document when use.

experiments are compared, as illustrated in figure. 2.18. It was found that the JC constitutive model can be employed to predict precise stress-strain behaviour at various strain rates according to the resulted experiments.

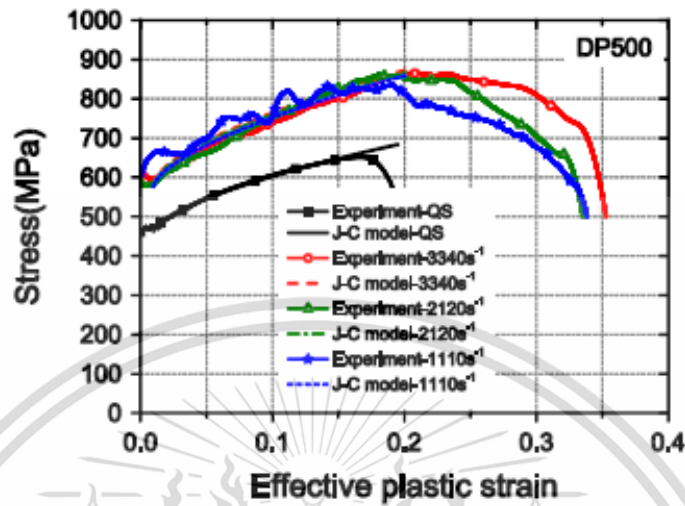


**Figure 2.18** Comparison of the Johnson-Cook model predictions with experimental results of DP500 steel.

Source: (Qin *et al.*, 2013)

## 2.5 Damage model

Damage model used in this work is ductile damage criterion which is generally employed for predicting crack initiation and crack propagation for both macroscopic failure and deformation microstructure (Borvik *et al.*, 2001; Sirinakorn, Wongwises and Uthaisangasuk, 2014; Srithananan, Kaewtatip and Uthaisangasuk, 2016). Ductile damage criterion describes the microscopic ductile failure which is driven by void nucleation, void growth and void coalescence until crack propagation, as shown in figure 2.19. For predicting the crack initiation, damage curve was employed by (Bao and Wierzbicki, 2004), which assumed that the equivalent plastic strain at the onset of the damage ( $\epsilon_p^f$ ) is a function of the stress triaxiality ( $\eta$ ) as illustrated in figure 2.20. The stress triaxiality is a ratio between hydrostatic stress ( $\sigma_h$ ) and Von Mises stress ( $\sigma_v$ ) which can be expressed as:

$$\eta = \frac{\sigma_h}{\sigma_v} = \frac{\frac{1}{3}(\sigma_1 + \sigma_2 + \sigma_3)}{\sqrt{\frac{1}{2}(\sigma_1 - \sigma_2)^2 + (\sigma_2 - \sigma_3)^2 + (\sigma_3 - \sigma_1)^2}} \quad (2.10)$$

This material is reserved for educational use only, not allowed for commercial use.

Forbidden to modify the content, and cite the document when use.

Where  $\sigma_1$ ,  $\sigma_2$  and  $\sigma_3$  are principal stress.

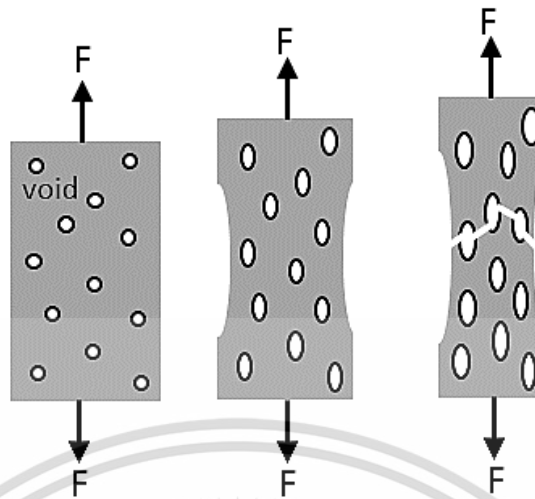


**Figure 2.19** Ductile damage in metal driven by void nucleation, void growth and void coalescence until crack propagation.

Source: (Münstermann and Bleck, 2009)

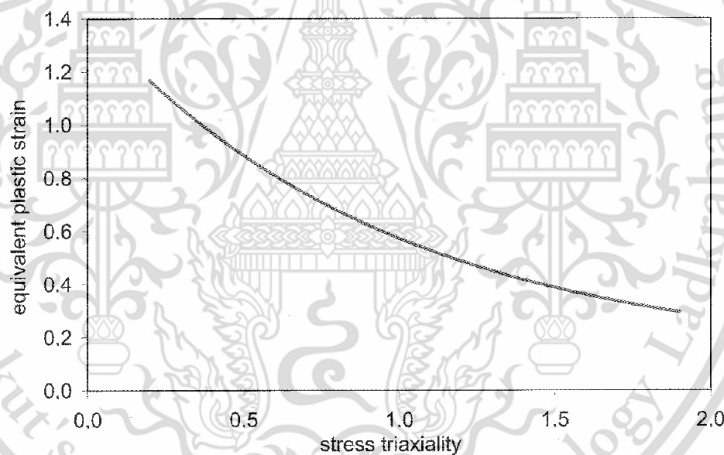


**Figure 2.20** Relationship between stress triaxiality and equivalent plastic strain as a damage criterion.

Source: (Bai and Wierzbicki, 2015)

Additionally, fracture behaviour of material under high strain rate deformation was also taken into account in this present work. Consequently, the effect of strain rate and temperature are incorporated to the damage curve model. Johnson and Cook described the effect of strain rate and temperature on ductile fracture (Johnson and Cook, 1985). The Johnson-Cook damage model has been developed to consider the effects of stress triaxiality, strain rate, and temperature by the following equations:

This material is reserved for educational use only, not allowed for commercial use.

Forbidden to modify the content, and cite the document when use.

$$\varepsilon^f = [d_1 + d_2 \exp(d_3 \eta)] [1 + d_4 \ln(\frac{\dot{\varepsilon}}{\dot{\varepsilon}_0})] [1 + d_5 T] \quad (2.11)$$

Where  $d_1$ ,  $d_2$ ,  $d_3$ ,  $d_4$  and  $d_5$  are empirical constants which could be obtained by experimental tests of the material in different effects such as stress triaxiality, strain rate and temperature. Nevertheless, the JC damage model is limited by stress triaxiality dependence. It could be applied to only predict fracture due to void formation at high stress triaxiality. Yingbin Bao and Tomasz Wierzbicki found that different stress triaxialities exhibited different type of fracture from their experimental testing of deformed 2024-T351 aluminum alloy specimen at various state-stress (Bao and Wierzbicki, 2004). Thus, fracture locus is not only demonstrated void formation, but also exhibited shear fracture phenomenon, as shown in figure 2.21.

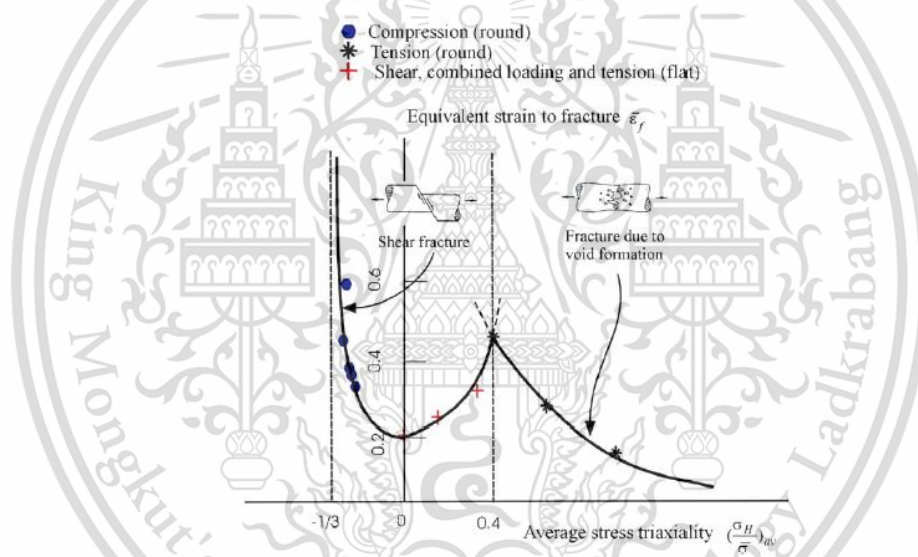


**Figure 2.21** Dependence of the equivalent strain to fracture on the stress triaxiality taking into account shear fracture phenomenon at quasi-static deformation.

Source: (Bao and Wierzbicki, 2004)

Additionally, (Erice, Roth and Mohr, 2018) developed a fracture model by combining the fracture locus and strain rate term of the JC damage model for representing damage curve at different strain rates as expressed in the equation (2.12). Example of obtained damage curves at various strain rates of CP1180 steel taking into account both void formation and shear fracture phenomenon are shown in figure 2.22.

$$\varepsilon_p^f = \varepsilon_\eta^f[\eta] \varepsilon_\dot{\varepsilon}^f[\dot{\varepsilon}_p] \quad (2.12)$$

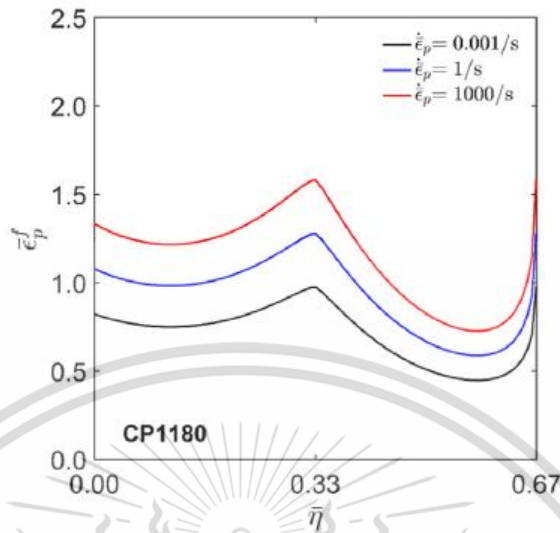


**Figure 2.22** Developed damage curve in combination with strain rate function.

Source: (Ericc, Roth and Mohr, 2018)

## 2.6 Digital Image Correlation

Digital Image Correlation (DIC) is a non-contact optical technique for measuring contour, deformation, and strain on almost any material. DIC is widely used for macroscopic mechanical testing by using high quality camera to detect the deformation mapping on deformed specimen. Additionally, the CDD camera which is high quality camera is applied for capturing the deformation of specimen. The overall setup of DIC technique was illustrated in figure 2.23.

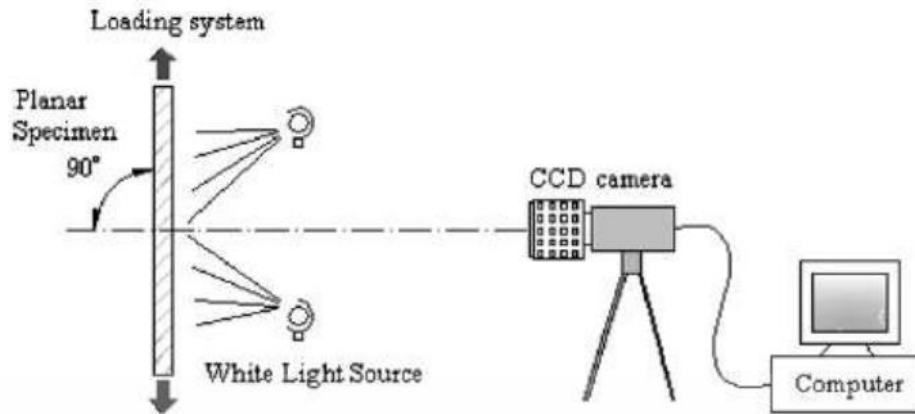


**Figure 2.23** Detected the deformation of specimen using high quality camera.

Source: (Pan *et al.*, 2009)

Before beginning the material testing, the specimen is sprayed by black spot on white background for referring the local deformation. During the material testing, the specimen is deformed, the black spots are also displaced and deformed. Consequently, the deformation mapping algorithm can detect the black spots by capturing planar images of the surface of body, as illustrated in figure 2.24.

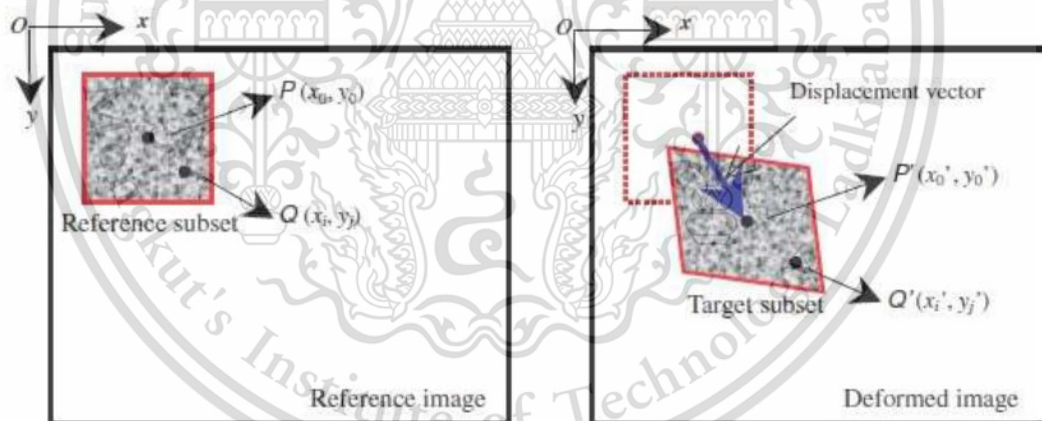


**Figure 2.24** Reference photos and images after the transformation of the specimen.

Source: (Pan *et al.*, 2009)

## CHAPTER 3

### EXPERIMENTS

In experimental procedures, the investigated effects of microstructure and strain rate on mechanical properties of DP steels are carried out. The experimental methods are applied in this work include microstructure characterization and mechanical testing. They can be divided into three topics that are material and microstructure analysis, quasi-static tensile tests following the standard ASTM E8 and tensile tests at different strain rates. The overall research methodology of this work is illustrated by a flow chart in Figure 3.1.

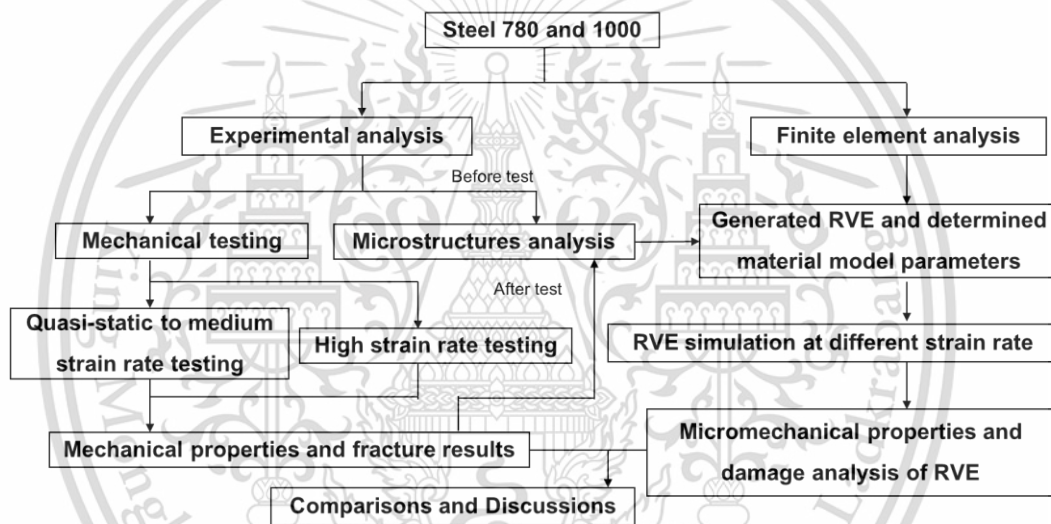


Figure 3.1 Flow chart of the research methodology.

### 3.1 Materials and microstructures

#### 3.1.1 Chemical composition analysis

The cold rolled DP steel sheets grade 780 and 1000 with the thickness of 1 mm and 1.2 mm, respectively, from part making industries were investigated in this work. The chemical composition of the steels is given in Table 3.1, which were determined by the vacuum emission spectroscopy.

**Table 3.1** Chemical composition of the used steel grade 780 and 1000.

Steel grade	C	P	Si	Cu	Ni	Cr	Mn	Mo
780	0.107	0.016	0.918	0.009	0.010	0.183	2.000	0.002
1000	0.171	0.014	0.460	0.008	0.018	0.002	2.346	0.001

### 3.1.2 Microstructure characterization

For the microstructure analysis of DP steels, the samples were prepared from the thickness plane for the metallography examination. At the beginning, the samples were polished by using silicon carbide paper with grit size of 240, 400, 600, 800, 1000, 1200 1500 and 2000 in<sup>2</sup> respectively, and were finally polished with 0.05  $\mu\text{m}$  alumina. Next, the samples were etched by 2% Nital solution (2 ml  $\text{HNO}_3$  in 98 ml ethanol). Finally, the microstructure of DP steels were characterized by using both a light optical microscope (LOM) and scanning electron microscope (SEM) at higher magnification, as shown in figure 3.2(a) and (b), respectively.

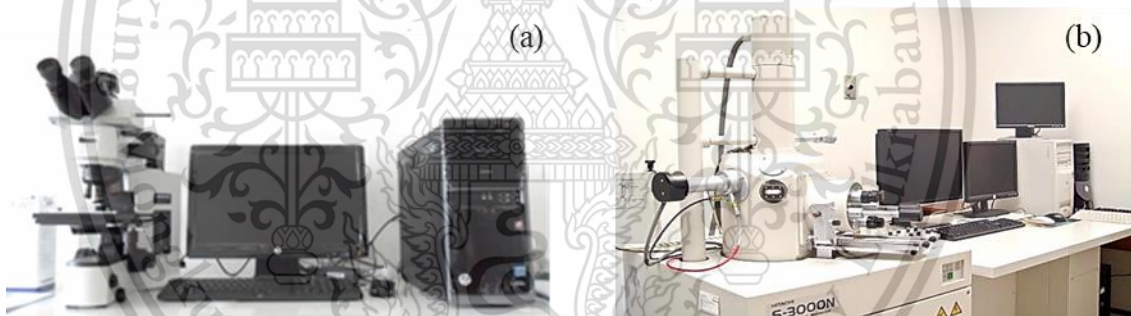


**Figure 3.2** (a) a light optical microscope and (b) scanning electron microscope.

In the obtained micrographs from LOM, the bright zones were ferrite and the dark distributed areas were martensite in figure 3.3(a,b). The observed microstructure consisted of large amount martensite islands scattered in ferritic phase matrix, which was similar in both DP steels. The observed initial microstructure at higher magnification characterized by SEM are present in figure 3.3(c,d).

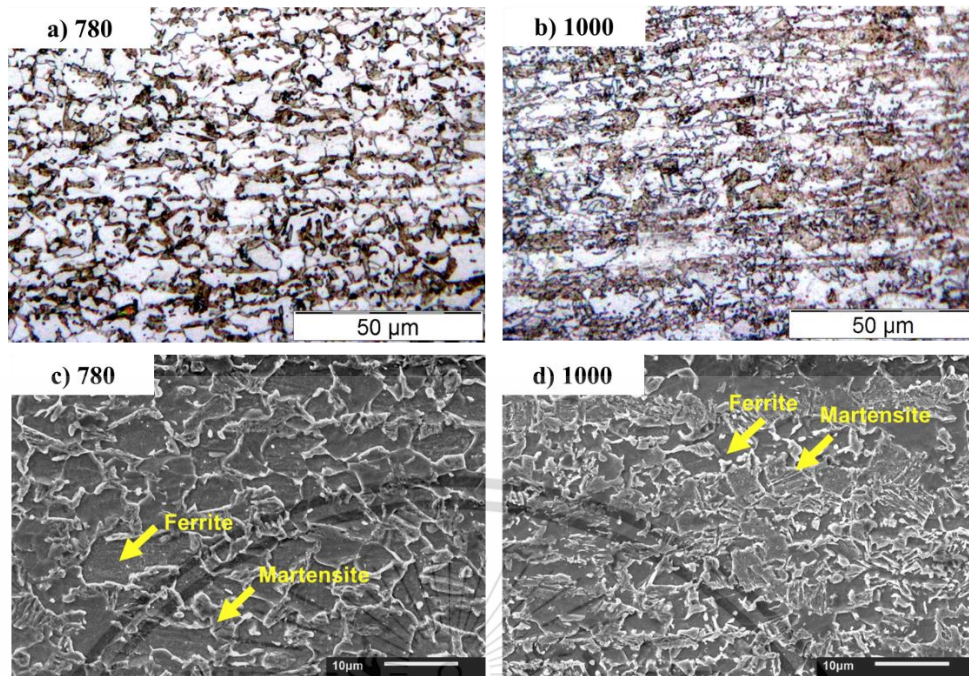


**Figure 3.3** Observed initial microstructure of steel grade (a,c) 780, (b,d) 1000 and (a,b) observed by LOM, (c,d) observed by SEM.

The microstructure phase fraction and the grain size of each phase were determined by a mean of the image analysis programming. In addition, the carbon contents in martensite were approximated by the rule of mass balance. Consequently, martensite volume fraction, ferrite grain size and carbon content in martensite of both 780 and 1000 are shown in Table 3.2. The ferrite grain size of 780 and 1000 were about 8.91  $\mu\text{m}$  and 5.71  $\mu\text{m}$ , respectively. It was found that the grain size of the ferritic phases of 780 were larger than those of 1000. The martensite phase fraction of the 780 and 1000 were approximately 36% and 50%, respectively. Additionally, the carbon contents in martensite were 0.287 wt.% and 0.338 wt.% for the 780 and 1000, respectively. Note that a hint of bainite was also found in the steel grade 980, but it was here neglected as its amount was not significant.

**Table 3.2** The resulted microstructure analysis of investigated steels.

Material	Martensite phase fraction (%)	Ferrite grain size ( $\mu\text{m}$ )	Carbon content in martensite (wt.%)
780	36	8.91	0.287
1000	50	5.71	0.338

This material is reserved for educational use only, not allowed for commercial use.

Forbidden to modify the content, and cite the document when use.

### 3.2 Quasi-static uniaxial tensile tests

For the Quasi-static uniaxial tensile tests, the standard specimen (SS) was employed for the tests for all experiments to obtain mechanical tensile properties of materials. The SS specimens were prepared according to the standard ASTM E8. The sheet samples had a gauge length of 25 mm and a nominal width of 6 mm, as illustrated in figure 3.4. The specimens were elongated under uniaxial deformation at room temperature with a strain rate of  $0.001 \text{ s}^{-1}$  by using a hydraulic universal tensile testing machine with the DIC technique, as demonstrated in figure 3.5. During the tests, a hydraulic universal tensile testing machine was recorded the force to calculate engineering stress values, while engineering strain values can be obtained by using the DIC technique, as illustrated in figure 3.6, for determined engineering stress-strain curves of the materials.

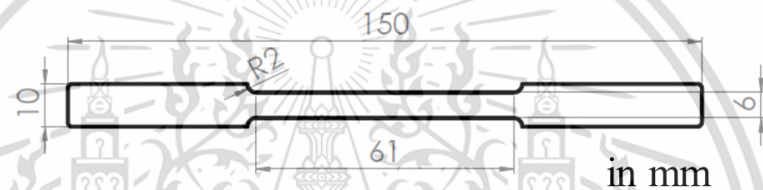


**Figure 3.4** Dimension of the SS specimen for quasi-static uniaxial tensile test.

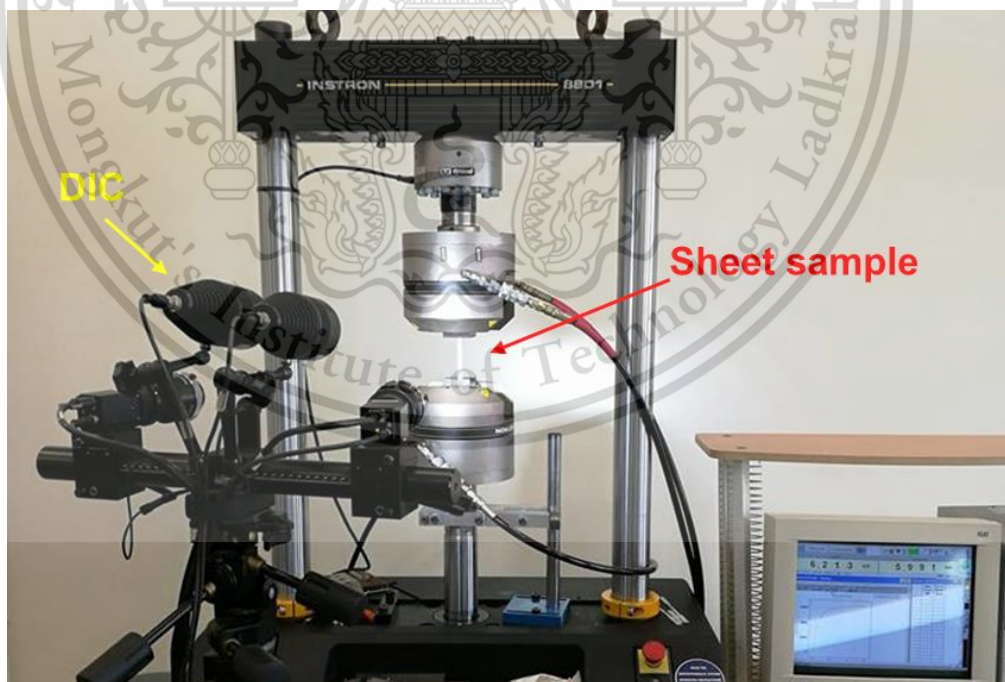


**Figure 3.5** Test setup of universal testing machine for quasi-static tensile tests.

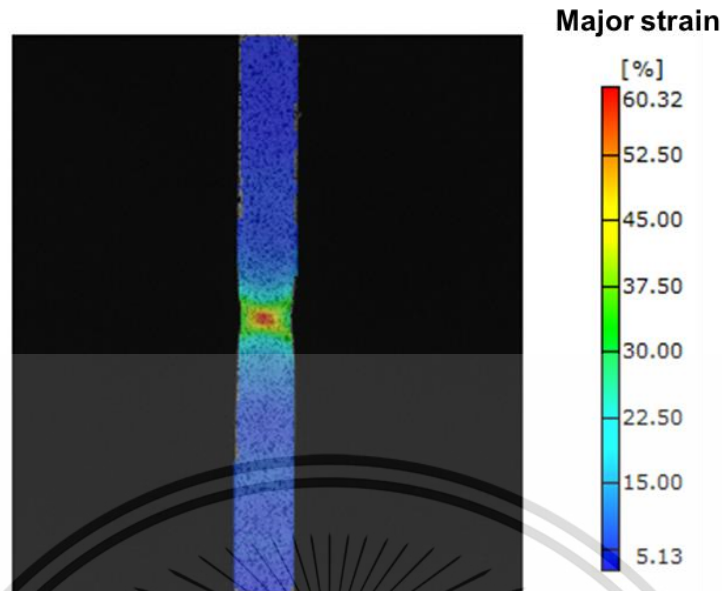


**Figure 3.6** Obtained major strain of the SS specimen by using DIC technique.

### 3.3 Tensile tests at various strain rates

For tensile tests at various strain rates, a modified specimen (MS) having the dimension, as demonstrated in figure 3.7, was applied for determining engineering stress-strain curves in different strain rates at room temperature to investigate effect of strain rate on deformation behaviour of material. In this work, tensile tests of MS sample at quasi-static to medium strain rates were carried out on the UTM, whereas the SHTB apparatus was employed for the tensile tests at high strain rates. Note that all samples were prepared along the rolling direction.

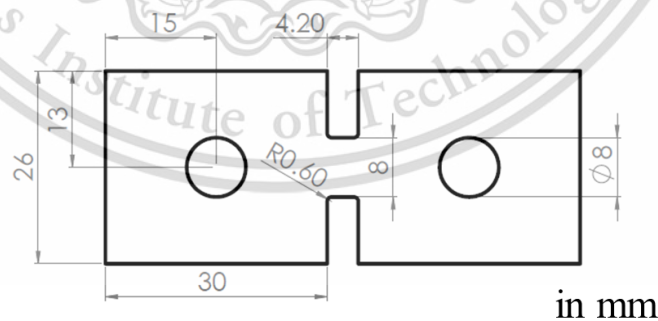


**Figure 3.7** MS specimen for tensile test at different strain rates.

#### 3.3.1 Quasi-static to medium strain rate tensile tests

Experimental testing of Quasi-static to medium strain rate tensile were carried out by using a hydraulic universal tensile testing machine with the DIC technique in the range

This material is reserved for educational use only, not allowed for commercial use.

Forbidden to modify the content, and cite the document when use.

strain rates from  $0.001 \text{ s}^{-1}$  to  $1 \text{ s}^{-1}$ . For the tests, The MS samples were firstly elongated at strain rate of  $0.001 \text{ s}^{-1}$  for quasi-static deformation, as shown in figure 3.8. Then, the medium strain rate tensile tests of MS samples were performed at strain rate of 0.5 and  $1 \text{ s}^{-1}$ .

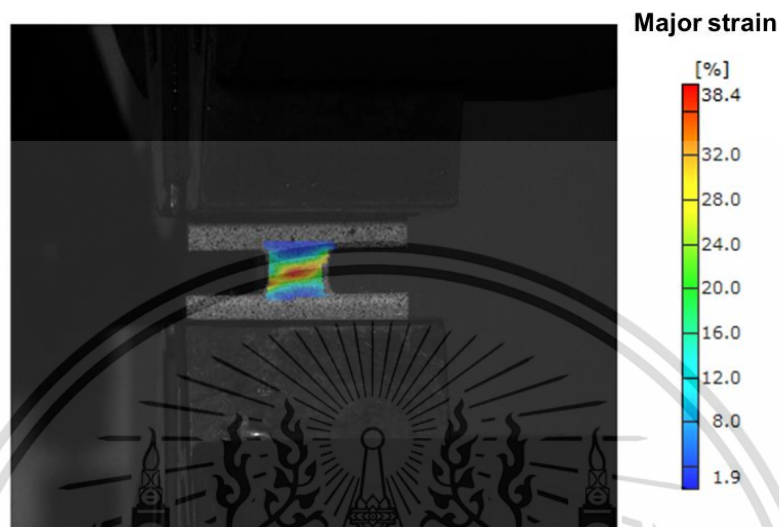


**Figure 3.8** Quasi-static deformation of MS specimen at strain rate of  $0.001 \text{ s}^{-1}$  measured by using DIC technique.

### 3.3.2 High strain rate tensile tests

For tensile tests at high strain rates, MS sheet specimens were elongated at high strain rates ( $\sim 1500\text{-}2500 \text{ s}^{-1}$ ) by using the SHTB apparatus. At least three repeated samples were employed. The bar system mainly consists of the incident bar, the transmission bar, and the hollow tube striker bar made by steel. For the setup tests, the specimens were clamped to the loading bar by using pins, as demonstrated in Fig. 3(b). Strain gauges were mounted on the incident bar and transmission bar for gathering the developed strain histories. Then, the strains measured from incident wave ( $\varepsilon_i$ ), transmission wave ( $\varepsilon_t$ ), and reflecting wave ( $\varepsilon_r$ ) were taken to calculate the overall engineering stress-strain curves of tested steel samples. Hereby, engineering stresses, engineering strains and strain rates were calculated according to the one-dimensional stress wave theory (Chen et al. 2011). The reflecting wave ( $\varepsilon_r$ ) was used to compute the strain rate and engineering strain, while the transmission wave ( $\varepsilon_t$ ) was considered for deriving the engineering stress.

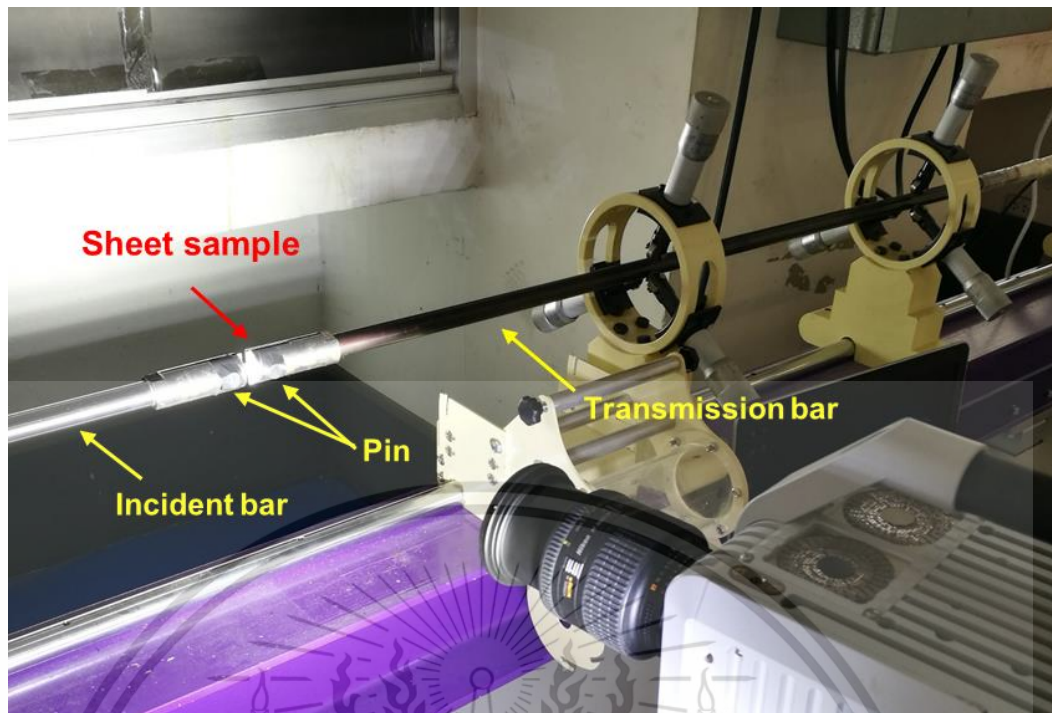
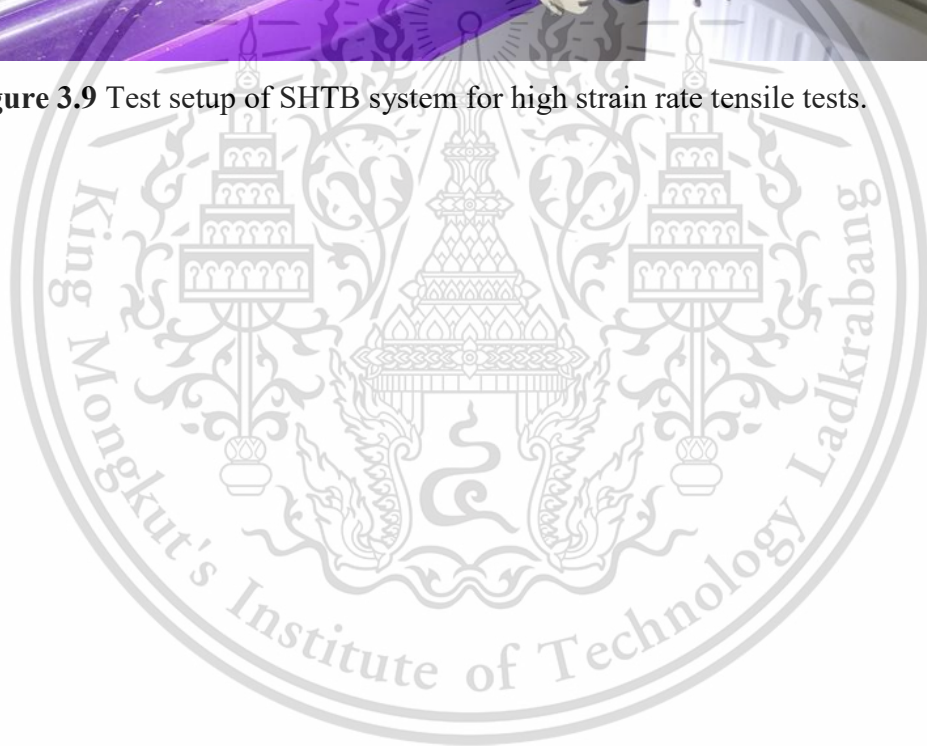


**Figure 3.9** Test setup of SHTB system for high strain rate tensile tests.



## CHAPTER 4

### EXPERIMENT RESULTS

#### 4.1 Tensile properties

For the examined steel grades 780 and 1000, plastic true stress-true strain curves from the quasi-static test of SS specimens were obtained and are provided in figure 4.1. It was found that the grade 1000 obviously exhibited higher yield and ultimate tensile strengths than those of grade 780, whereas the uniform and total elongation of grade 780 larger than those from grade 1000. The strain hardening rate of grade 1000 from yield begin until strain around 0.03 was higher than that of grade 780. Beyond this strain, both steels showed about similar hardening rate. The determined tensile properties of steels are presented in Table 4.1. The YS/TS ratios of grade 780 and 1000 were approximately the same, namely, 0.67. The post-uniform elongation of grade 780 was twice that of grade 1000.

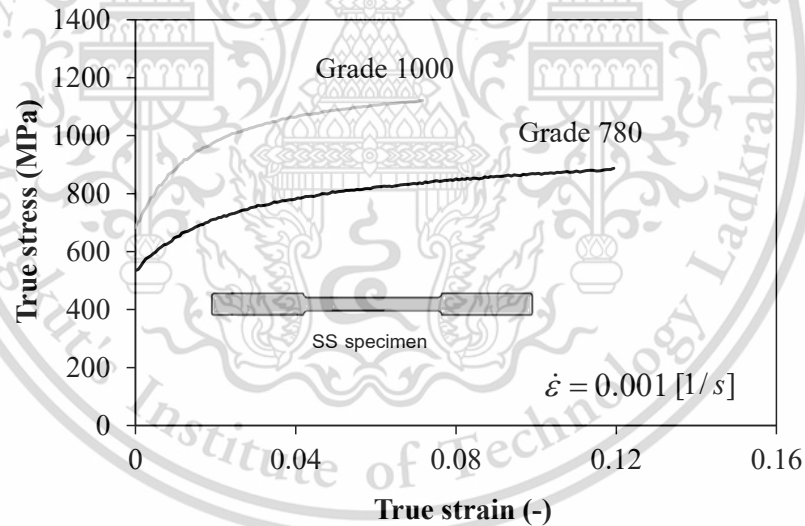


**Figure 4.1** Determined true stress-true strain curves under quasi-static uniaxial deformation of the steel grades 780 and 1000.

**Table 4.1** Resulted tensile properties of investigated steels.

Steel grades	YS (MPa)	UTS (MPa)	Elongation	
			Uniform (%)	Total (%)
780	528	778	14.0	22.7
1000	682	1030	8.7	12.9

This material is reserved for educational use only, not allowed for commercial use.

Forbidden to modify the content, and cite the document when use.

## 4.2 Stress-strain behaviour at various strain rates

To investigate effects of strain rates on the stress-strain responses of examined steels, tensile tests of the MS samples were performed under quasi-static ( $\sim 0.001 \text{ s}^{-1}$ ), medium strain rates ( $\sim 0.1\text{-}1 \text{ s}^{-1}$ ) and high strain rates ( $\sim 1500\text{-}2500 \text{ s}^{-1}$ ) condition. The determined engineering stress-strain curves at different strain rates for steel grade 780 and 1000 are demonstrated in figure 4.2(a) and (b), respectively. It is seen that three repeated tests at high strain rate range on the SHTB provided overlapping stress-strain curves with slight scatters similar to the results in (Qin et al. 2013; Wang et al. 2013). Nevertheless, the deviations were small and the tests were hence repeatable. Obviously, the steel grade 780 showed larger strain rate sensitivity than that of grade 1000 that was in accordance to that reported in (Wang et al. 2013; Xu et al. 2019; Das et al. 2017; Alturk et al. 2017). Furthermore, resulting yield strengths (YS), ultimate tensile strengths (UTS), elongations at fracture (FEL) and energy absorptions of the investigated steels under various strain rates are compared in figure 4.3(a) and (b), respectively. It was found that the yield and tensile strengths of both steels were enhanced by increasing strain rates. The increase of tensile strength was more significant than that of yield strength, especially at high strain rate region. This was in contrast to steels with low strain hardening rate like other conventional deep drawing steels. The examined steels exhibited positive strain rate sensitivities. The yield strengths at high strain rate of steel grade 780 and 1000 increased approximately 26% and 10%, respectively, in comparison with those from quasi-static condition. For the tensile strength, the grade 780 and 1000 showed such increases of around 38% and 15%, respectively. These observed increasing trends were in according to the results in (Qin et al. 2013; Das et al. 2017; Alturk et al. 2017). The larger increases of strengths or higher strain rate sensitivity of grade 780 when subjected to loading at high strain rates was due to the lower martensitic phase fraction as discussed in (Wang et al. 2013; Xu et al. 2019; Alturk et al. 2017). The elongations at fracture of grade 780 under various strain rates were slightly fluctuated, whereas those of grade 1000 were obviously increased by increasing strain rate in accordance to that reported in (Wang et al. 2013; Xu et al. 2019; Das et al. 2017; Alturk et al. 2017). Under high strain rate deformation, the microstructure consisting of higher amount of hard phases like martensite as that of grade 1000 led to slight increase of strength but noticeable increase of elongation. The similar characteristics were also described in (Wang et al. 2013; Xu

This material is reserved for educational use only, not allowed for commercial use.

Forbidden to modify the content, and cite the document when use.

et al. 2019; Das et al. 2017; Alturk et al. 2017; Yu, Guo, and Lai 2009). Additionally, energy absorptions until fracture of the investigated steels were determined as the concurrence of strength and elongation and depicted in figure 4.3(b). It is seen that in the high strain rate region the energy absorptions of both steels greatly increased, while no considerable change at medium strain rate was found. The increasing rates of energy absorption of grades 780 and 1000 were similar. The grade 780 showed somewhat higher energy absorption than the grade 1000 at all strain rate regions. More discussions about microstructure effect on mechanical properties of DP steels are provided later together with other results.

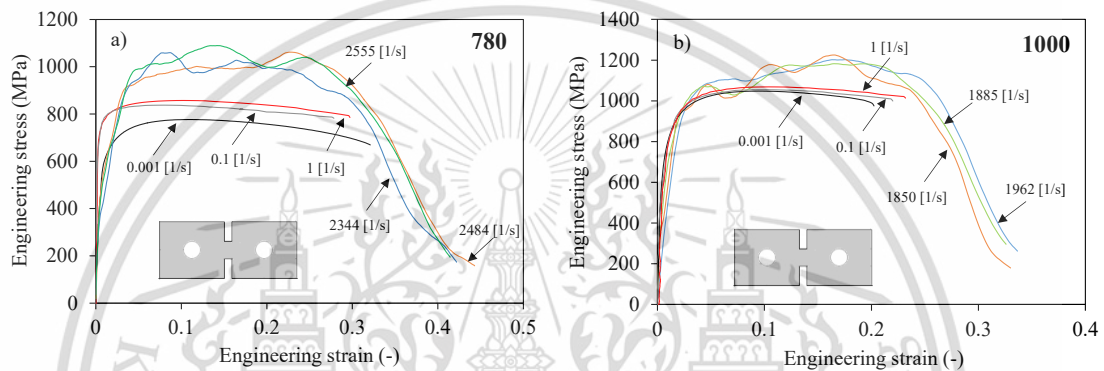


**Figure 4.2** Determined engineering stress-strain curves at different strain rates of steel grades (a) 780 and (b) 1000.

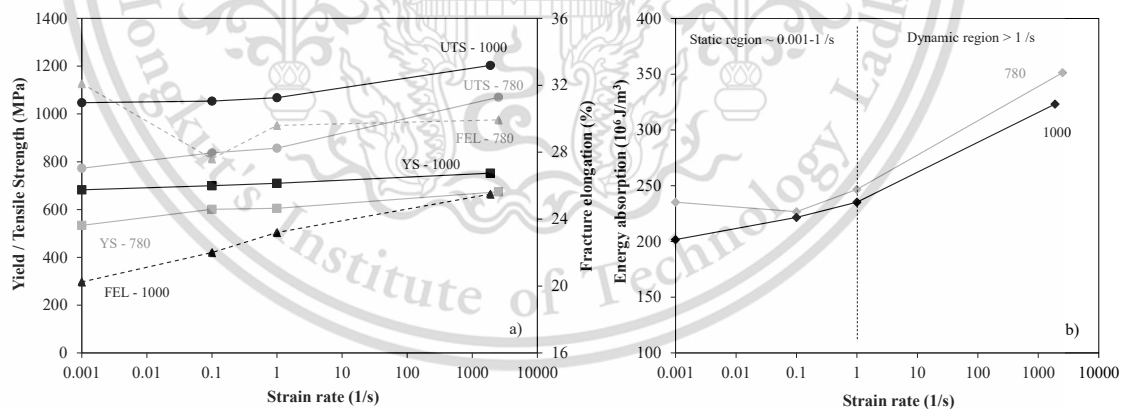


**Figure 4.3** Influences of strain rate on (a) yield strength, tensile strength, fracture elongation and (b) energy absorption of examined steel grade 780 and 1000.

### 4.3 Observation of crack development

After the tensile tests, microstructures in the vicinity of fracture surface of failed samples were characterized by SEM analysis. Figure 4.4 illustrates the microstructures of both examined steels under quasi-static and high strain rate in comparison. By the

This material is reserved for educational use only, not allowed for commercial use.

Forbidden to modify the content, and cite the document when use.

quasi-static deformation, samples with low and high martensitic phase fraction of grade 780 and 1000, respectively, exhibited similar typical crack occurrence of DP steel. Firstly, preliminary micro-voids in ferrite close to ferrite/martensite interfaces and interfacial decohesion were mostly observed, as seen in figure 4.4(a) and 4.4(d). According to the results of previous work (Anbarlooie and Kadkhodapour 2018) it was reported that the initial voids formed at the ferrite-ferrite grain boundaries and then propagated to the ferrite/martensite interfaces. Secondly, quasi-brittle cracks were also found at some large martensitic islands in both steels that was similar to that found in (Ramazani et al. 2016), as depicted in figure 4.4(b) and 4.4(e). On the other hand, at high strain rate microstructures of both grades showed micro-voids in the vicinity of interfaces and distinct interfacial decohesion of ferrite and martensite, as demonstrated in figure 4.4(c) and 4.4(f). Besides, some micro-voids were also found in martensite particles of grade 1000 samples, since small ferrite areas were embedded in martensitic islands, as seen in figure 4.4(f). The high local plastic strain of ferrite caused the occurring micro-cracks or interfacial decohesion (Ghadbeigi et al. 2010). Then, these micro-voids propagated through the surrounding martensitic islands. However, brittle cracking of martensitic islands was not observed in both steel grades under high strain rate as also reported in (Das et al. 2017). Because the adiabatic softening took place during plastic deformation on the microstructure level so that the formation of martensite cracking changed to ductile deformation at such large loading rate (Wang et al. 2013). For steel grade 780, higher number of voids was found in the samples from high strain rate test and voids occurred at both interphases as well as within ferritic grains. For steel grade 1000, samples from both static and dynamic tests exhibited similar amounts of voids, which mostly took place at the interphases since the phase fraction of martensite was high. The samples of grade 780 under static load showed the lowest number of voids.

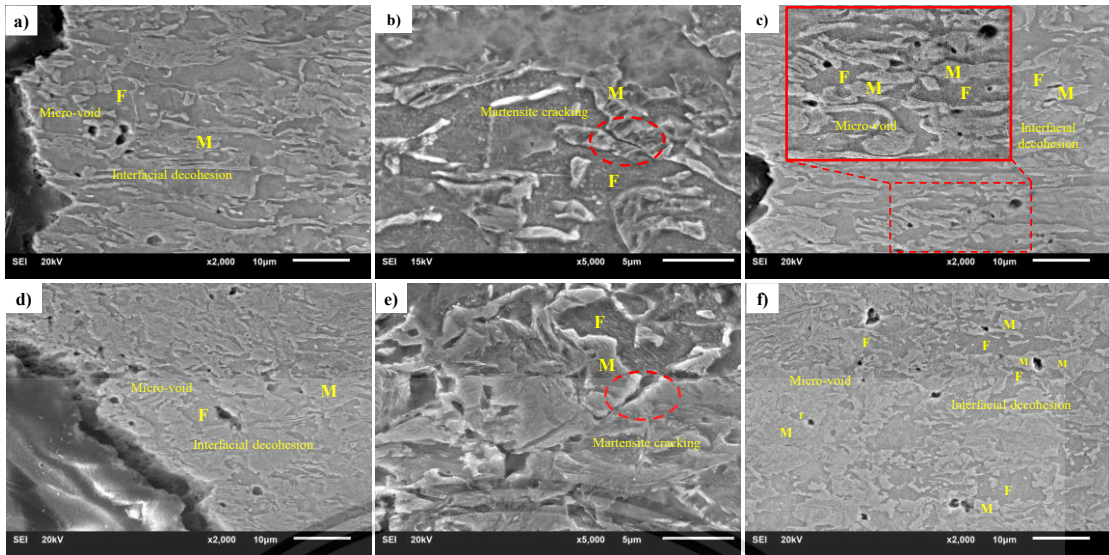


**Figure 4.4** SEM images of microstructures close to the fracture surfaces of steel grade 780 after tensile tests under (a, b) quasi-static condition, (c) high strain rate and of steel grade 1000 under (d, e) quasi-static condition and (f) high strain rate. (F is ferrite and M is martensite)

#### 4.4 Fractographs analysis

The fracture surfaces of MS samples after tensile tests under quasi-static and high strain rate condition were investigated by using SEM. Definition of the fracture surface in the necking zone is presented in figure 4.5 as following to literature (Sato et al. 2015).

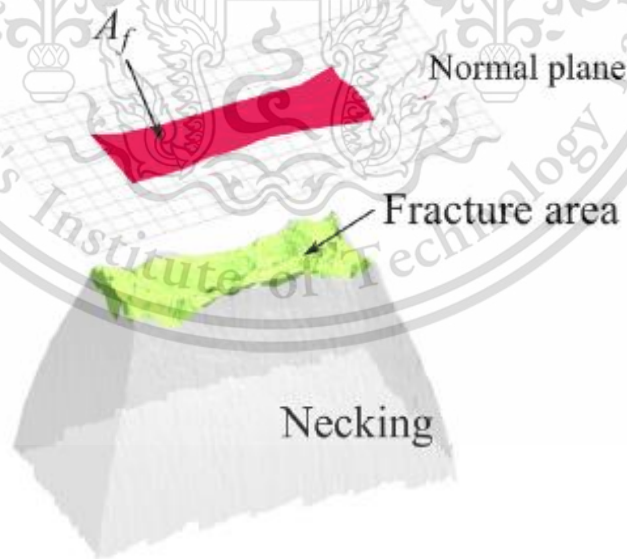


**Figure 4.5** Definition of the fracture surface in the necking zone.

Source: (Sato et al. 2015)

This material is reserved for educational use only, not allowed for commercial use.

Forbidden to modify the content, and cite the document when use.

Typical fracture surfaces of grade 780 and 1000 under quasi-static and high strain rate deformation are demonstrated in figure 4.6. Increasing strain rate could noticeably affect the fracture mechanism of examined steel samples. The dimple sizes of obtained fracture surfaces were thus measured by using an image analysis program. It was found that the average dimple areas of steel grade 780 from quasi-static and high strain rate tests were  $0.097 \mu\text{m}^2$  and  $0.265 \mu\text{m}^2$ , respectively, while those of grade 1000 were  $0.075 \mu\text{m}^2$  and  $0.121 \mu\text{m}^2$ , respectively. These measured dimple sizes fairly coincided with the determined elongations of both steels. In addition, the distributions of dimple sizes within the range of  $2 \mu\text{m}^2$  observed in the investigated samples from both strain rates were gathered, as provided in figure 4.7. In this work, the dimple sizes smaller than  $0.2 \mu\text{m}^2$  were considered as the secondary voids. For the grade 780, the dimple sizes of samples from high strain rate condition were remarkably increased. In other words, at high strain rate fewer numbers of small voids were observed. The ferrite in steel grade 780 with lower martensitic phase fraction exhibited higher plastic deformability under high strain rate due to the adiabatic heating that afterwards led to larger voids before fracture as given in (Das et al. 2017). On the other hand, more cleavage fracture planes were found in the samples of grade 780 at high strain rate than those at quasi-static condition, as seen in figure 4.6(a) and (b). In contrast, more areas of cleavage fracture were observed in samples from static rather than high strain rate deformation in case of grade 1000. The dimple sizes of grade 1000 at both strain rates were just slightly different and non-uniform, as depicted in figure 4.6(c) and (d). The larger dimple sizes of grade 780 at high strain rate loading were due to higher void growth rate of steel with lower martensitic phase fraction according to (Das et al. 2017). The growth of void in ferrite of grade 1000 was limited because of larger martensitic areas. This void growth rate was significantly affected by local plastic flow ability in the microstructure (Wang et al. 2013). The larger dimple sizes or higher growth rate of grade 780 thus related to a high strain rate hardening ability. In contrast, the grade 1000 exhibited smaller void sizes at high strain rate so that its strain rate hardening behaviour was worse.

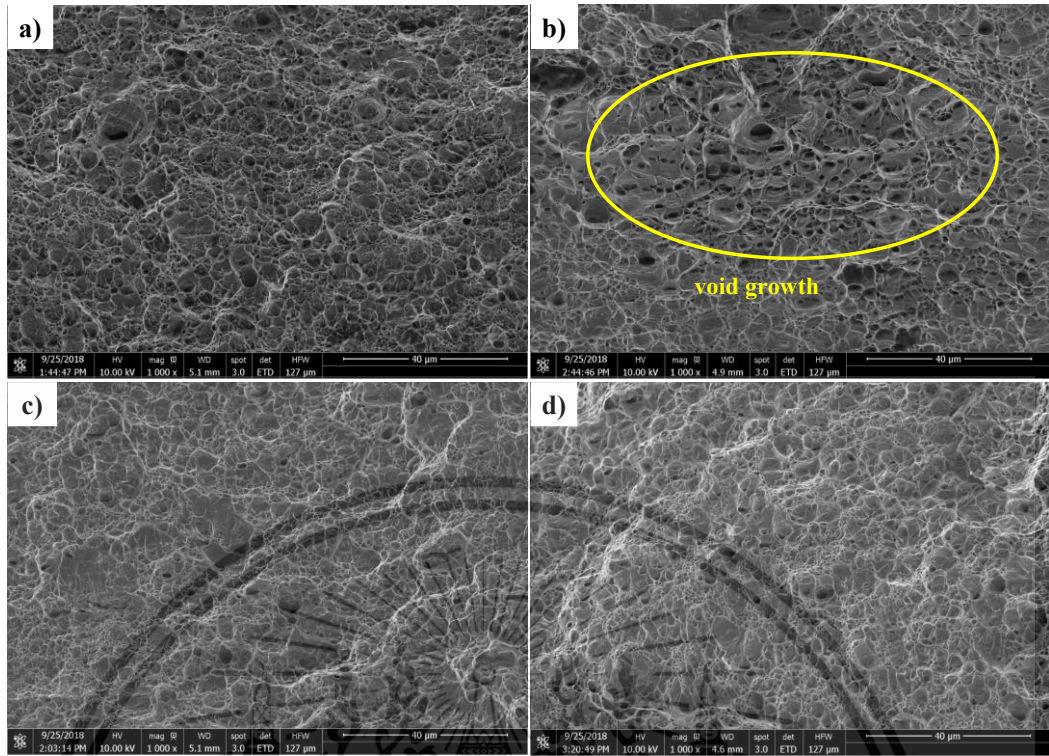


**Figure 4.6** Fracture surfaces of grade (a) 780 at quasi-static condition, (b) 780 at high strain rate, (c) 1000 at quasi-static condition and (d) 1000 at high strain rate by SEM.

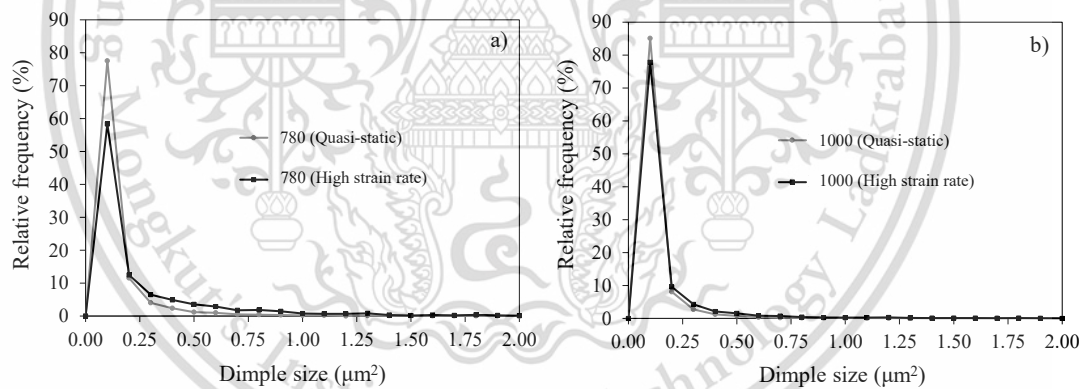


**Figure 4.7** Resulted dimple size distributions in fracture surfaces of grade (a) 780 and (b) 1000 at various strain rates.

## CHAPTER 5

### MODELLING AND SIMULATION

In this study, finite element (FE) method was applied to describe mechanical behaviour of examined DP steels. Boundary condition of the FE model was defined following to the concerned strain rate condition. Therefore, this chapter includes definition pre-processing of the FE model such as representative volume element, boundary condition, flow curves for the individual phase as well as parameters identification for used damage models.

#### 5.1 Macroscopic flow curve model

In this work, high strain rate deformations of high strength steels grades 780 and 1000 were examined. Thus, plasticity model taking into account strain hardening and strain rate hardening was employed to describe flow stress behaviour of material at various strain rates. An empirical model as a combination of Swift-Voce hardening law and Johnson-Cook (JC) rate-dependent model was applied (Hyun, Hoon, and Wagoner 2010; Roth and Mohr 2014), as given in the equation (5.1).

$$\sigma[\varepsilon, \dot{\varepsilon}] = \left( \alpha \{A(\varepsilon_0 + \varepsilon^n)\} + (1 - \alpha) \{ \sigma_0 + Q(1 - \exp(-\beta \cdot \varepsilon)) \} \right) \cdot \left( 1 + C \ln\left(\frac{\dot{\varepsilon}}{\dot{\varepsilon}_0}\right) \right) \quad (5.1)$$

For the first term of the equation (5.1),  $A$ ,  $\varepsilon_0$ ,  $n$ ,  $\sigma_0$ ,  $Q$ ,  $b$  are the Swift and Voce material parameters, and the parameter  $0 \leq \alpha \leq 1$  is a weighting coefficient. The second term is JC strain rate hardening equation including the parameters  $C$  and the reference strain rate  $\dot{\varepsilon}_0$ . Firstly, the Swift-Voce constants could be calibrated with the plastic true stress-strain curves from experimental quasi-static tensile tests of SS samples. The comparisons between predicted and determined static stress-strain curves of both steels are illustrated in figure 5.1. Subsequently, the JC model parameters were obtained on the basis of dynamic tensile tests at different strain rates using MS sample. The JC strain rate sensitivity parameter  $C$  was determined with regard to a linear relationship between natural logarithm of strain rate versus the ratio of dynamic and static yield stress, as also presented in (Qin et al. 2013; Singh et al. 2011). The predicted rate-dependent flow

This material is reserved for educational use only, not allowed for commercial use.

Forbidden to modify the content, and cite the document when use.

stress curves of steel grade 780 and 1000 are illustrated together with the experimental dynamic tensile tests in figure 5.2(a) and (b) for grades 780 and 1000, respectively. It is seen that the macroscopic stress-strain responses at all varying examined strain rates calculated by the JC models fairly agreed with the experimentally determined curves. In Table 5.1, the used model parameters of macroscopic flow stress curves for the investigated steels are summarized.

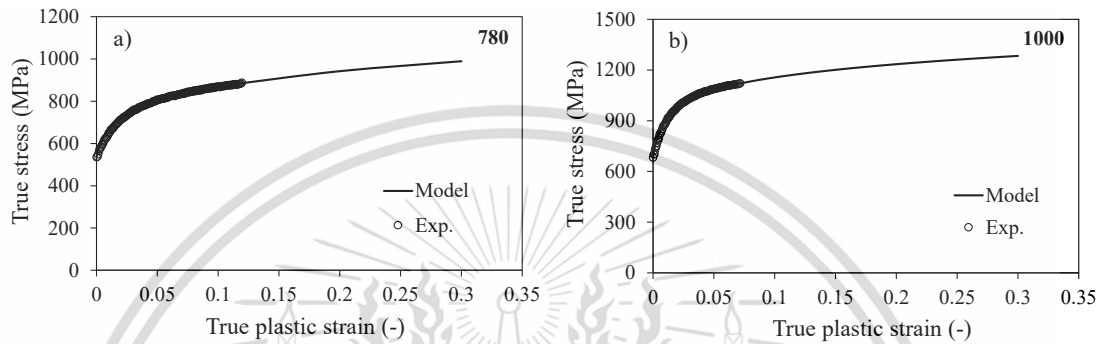


**Figure 5.1** Quasi-static stress-strain curves of grade (a) 780 and (b) 1000 from tensile tests and predicted by the combined Swift-Voce model.

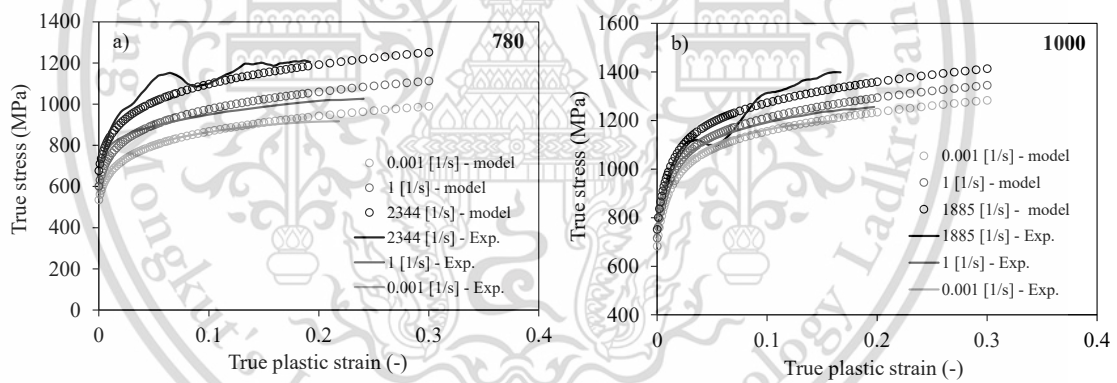


**Figure 5.2** Stress-strain curves at various strain rates of grade (a) 780 and (b) 1000 from dynamic tensile tests and predicted by Swift-Voce model combined with JC strain rate hardening model.

**Table 5.1** Obtained plasticity model parameters of the investigated steels.

Steel grade	Combined Swift-Voce model						JC model		
	$A$	$n$	$\varepsilon_0$	$\alpha$	$k_0$	$Q$	$\beta$	$C$	$\dot{\varepsilon}_0$
780	1200	0.13	0.00200	0.9	534	117	50	0.018	0.001
1000	1500	0.12	0.00142	0.8	682	540	80	0.007	0.001

## 5.2 Representative volume element (RVE)

Representative volume element (RVE) is a small volume of material on micro-scale which is used for calculating mechanical response of corresponding macroscopic behavior and investigated deformation of microstructure. In this work, RVE model was employed for investigated ferritic-martensitic microstructure of the DP steel, also morphologies, phase fraction and mechanical properties of each phase were taken into account for computation of micromechanical behavior. 2D RVEs were generated on the basis of a random area two-phase microstructure of examined DP steel taken from a light optical microscopy by using In-house software in coordination with Abaqus/CAE software. A micrograph with the size of  $50 \times 50 \mu\text{m}^2$  was used and the element size of the 2D RVE was  $0.5 \times 0.5 \mu\text{m}^2$ . The two-dimensional plane strain (CPE4) elements was used for micromechanical behaviour analysis due to the thickness of sheet sample was much larger than RVE model size (Thipwipa Sirinakorn, Uthaisangsuk, and Srimanosawapal 2014). The employed RVE models with ferritic and martensitic phases of the steel grade 780 and 1000 are depicted in figure 5.3.

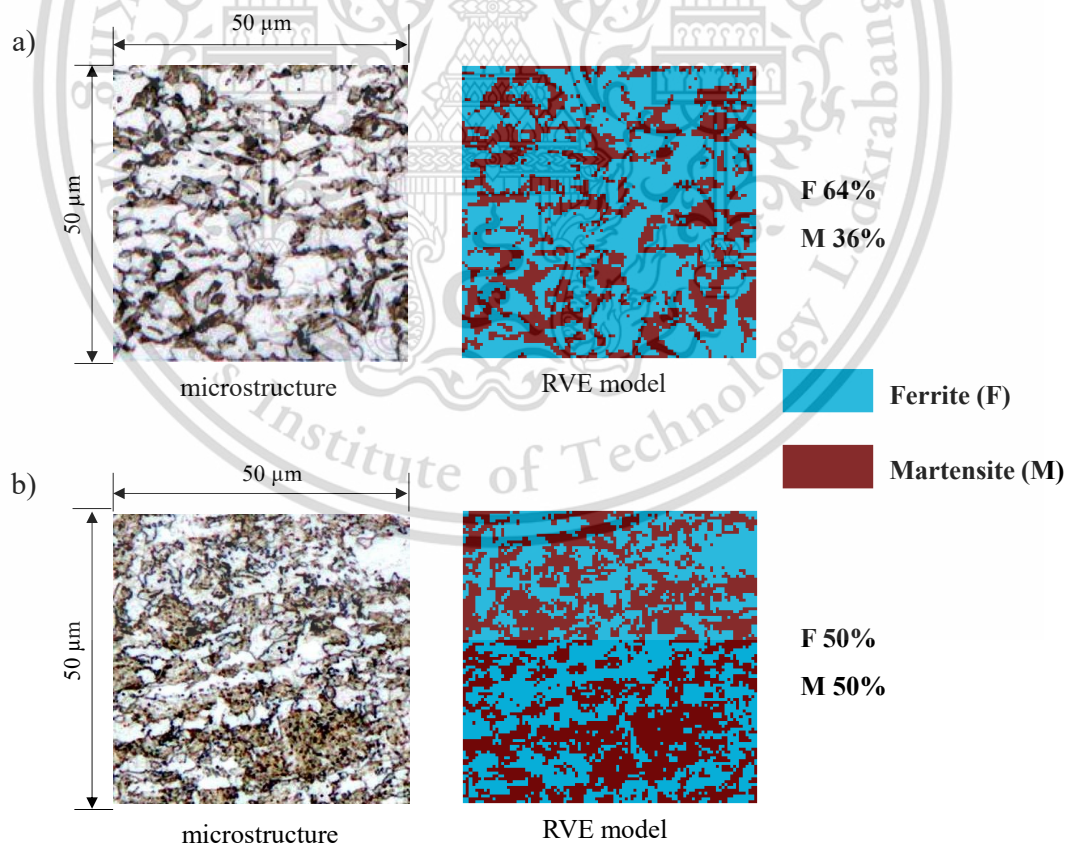


**Figure 5.3** 2D RVE models used for the examined steel grades (a) 780 and (b) 1000.

### 5.3 Micromechanics based flow curve modelling

#### 5.3.1 Single phase flow curves for quasi-static deformation

For the examined two-phase steels, static flow curves of the single phases, ferrite and martensite, were described by using a dislocation density based strain hardening model (Ramazani et al. 2016; Thipwipa Sirinakorn, Uthaisangasuk, and Srimanosawapal 2014). Hereby, the true stress as a function of plastic true strain can be expressed as following:

$$\sigma = \sigma_0 + \Delta\sigma + \alpha M \mu \sqrt{b} \sqrt{\frac{1 - \exp(-Mk_r \varepsilon)}{k_r L}} \quad (5.2)$$

Where  $\sigma$  and  $\varepsilon$  are the von Mises stress and equivalent plastic strain, respectively. The first term  $\sigma_0$  represents the Peierls stress and the effect of alloying elements in the solid solution state, as given in the equation (5.3).

$$\sigma_0 = 77 + 750(\%P) + 60(\%Si) + 80(\%Cu) + 45(\%Ni) + 60(\%Cr) + 11(\%Mn) + 11(\%Mo) + 50000(\%N_{ss}) \quad (5.3)$$

The second term,  $\Delta\sigma$  in the equation (5.2) described the material strengthening by precipitation or carbon in solution. For ferrite, it depended on the carbon content as following.

$$\sigma = 5000 \times (\%C_{ss}^f) \quad (5.4)$$

While for martensite, it was given as:

$$\sigma = 3065 \times (\%C_{ss}^m) - 161 \quad (5.5)$$

Where  $\%C_{ss}^f$  and  $\%C_{ss}^m$  were the carbon content (in wt.%) in ferrite and martensite, respectively. The carbon contents in ferrite of the grades 780 and 1000 were obtained by means of ThermoCalc. Then, the carbon contents in martensite depended on the

This material is reserved for educational use only, not allowed for commercial use.

Forbidden to modify the content, and cite the document when use.

corresponding phase fractions and were determined by using the rule of mass balance (T. Sirinakorn, Wongwiset, and Uthaisangasuk 2014; Srithananan, Kaewtatip, and Uthaisangasuk 2016). As a results, the calculated carbon contents in ferrite and martensite of grade 780 were 0.004 and 0.287 wt.%, respectively, while those of grade 1000 were 0.006 and 0.338 wt.%, respectively.

The last term of the equation (5.2) demonstrated the effect of dislocation strengthening and material softening, which contained the material constant ( $\alpha = 0.33$ ), Taylor factor ( $M = 3$ ), shear modulus ( $\mu = 80,000$  MPa), Burger's vector ( $b = 2.5 \times 10^{-10}$  m) for both phases. Moreover, the recovery rates ( $k_r$ ) and dislocation mean free paths ( $L$ ) of each phase were defined separately (Thipwipa Sirinakorn, Uthaisangasuk, and Srimanosawapal 2014). For ferrite, the parameter ( $k_r$ ) was set to be  $10^{-5}/d_\alpha$ , whereby  $d_\alpha$  was the average grain size of ferrite, and the dislocation mean free path was equal to the grain size. In case of martensite, the parameters  $L$  and  $k_r$  were used as the fitting parameters.

To validate the flow curves of both single phases and corresponding model parameters, RVE simulations coupled with the modelled individual flow stress curves were carried out under static load. The symmetry boundary condition according to a uniaxial tensile deformation were defined similar to (Darabi et al. 2017), as illustrated in figure 5.4. The J2 plasticity model was applied as it was acceptable to consider an isotropic yield on the microscale level of AHS steels (Uthaisangasuk, Prahl, and Bleck 2008). The first order homogenization method was used to determine the overall stress-strain response of steels from the RVE simulations. The predicted static true stress-strain curves of grade 780 and 1000 are compared with the experimental tensile curves, as shown in figure 5.5, together with the respective applied single phase flow curves. The magnitudes of flow stresses of ferrite in both steels were similar, while those of martensite in grade 1000 were noticeably higher due to the larger carbon content of steel. It is obvious that the static stress-strain responses obtained by the RVE microscopic simulations agreed well with the experimental results.

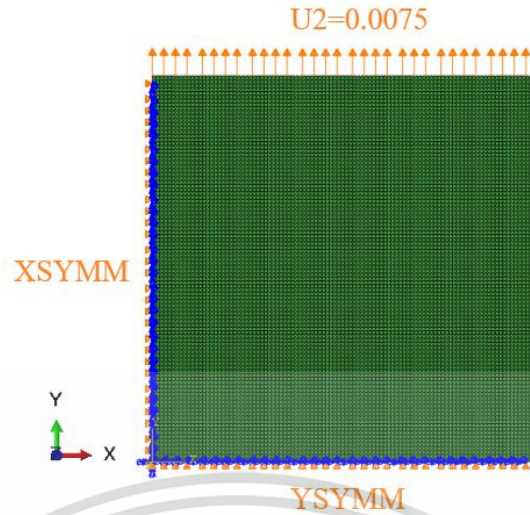


**Figure 5.4** The symmetry boundary condition of RVE tensile simulation.

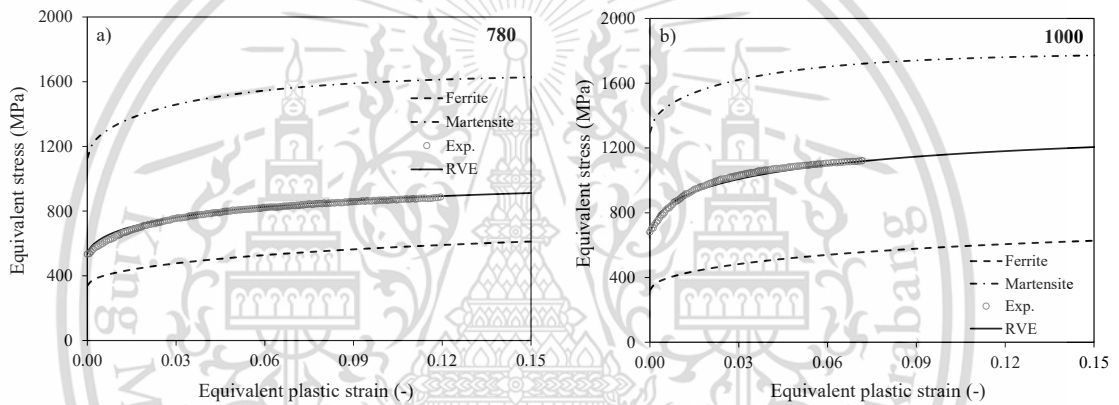


**Figure 5.5** Static stress-strain curves of single phases and steel grades (a) 780 and b) 1000 obtained by experiments and RVE simulations.

### 5.3.2 Single phase flow curves for high strain rate deformation

In addition to the static behaviour, material behaviour under high strain rate deformation at the micro-scale of investigated AHS steels was considered. The dislocation density based flow curve model from the equation (5.2) was combined with the Johnson-Cook strain rate hardening model for describing single phase flow stress curves at different strain rates. Thus, the micromechanics model coupled with the JC multiplier can be expressed as following:

$$\sigma(\varepsilon, \dot{\varepsilon}) = \left( \sigma_0 + \Delta\sigma + \alpha M \mu \sqrt{b} \sqrt{\frac{1 - \exp(-Mk_r \varepsilon)}{k_r L}} \right) \left( 1 + C \ln\left(\frac{\dot{\varepsilon}}{\dot{\varepsilon}_0}\right) \right) \quad (5.6)$$

This material is reserved for educational use only, not allowed for commercial use.

Forbidden to modify the content, and cite the document when use.

To identify the rate-dependent material characteristic or the JC strain rate hardening parameter  $C$  for the micro-scale level, tensile properties of DP steels at various strain rates correlated with results from transmission electron microscopic (TEM) observations of deformed microstructures in the literatures (Das et al. 2017; Hengjun et al. 2018; Liang et al. 2018; Wang et al. 2013; Xu et al. 2019) were taken into account. (Hengjun et al. 2018) reported that no noticeable change of dislocation density in martensite lath at different strain rates was found, while dislocation density in ferritic grains were greatly increased by higher strain rates. Moreover, effects of martensitic volume fraction on tensile properties of DP steels were studied in (Alturk et al. 2017; Qin et al. 2013; Wang et al. 2013). It was demonstrated that increased martensitic phase fraction led to lower strain rate sensitivity of DP steels. The strain rate hardening effect on flow stress behaviour of martensite can be therefore negligible. In this work, the JC multiplier term was then not applied to the martensitic phase in RVE simulations. On the other hand, multiple slip systems were obviously found in the ferritic matrix of DP steels under dynamic strain rates, whereas dislocation densities in ferrite were lower at quasi-static deformation (Hengjun et al. 2018; Liang et al. 2018). Besides, (Xu et al. 2019) showed that under high strain rate condition dislocation density in ferrite of DP steel increased and dislocation cells were also provoked so that it resulted in strengthening of ferrite. Hence, a positive strain rate sensitivity was defined for the ferritic phase in RVE and its JC strain rate hardening parameter  $C$  was determined by a calibration between RVE simulation results and the experimental data. RVE simulations under tensile loading were conducted at various strain rates similar to those of quasi-static case. The flow stress curves of grade 780 and 1000 under quasi-static and high strain rate loading predicted by the RVE simulations are compared with those from the experiments, as illustrated in figure 5.6(a) and (b), respectively. It was found that the JC strain rate hardening parameters  $C$  of 0.03 was determined and similar for the ferritic phases in both steel grades. It is noted that the measured average grain sizes of ferrite in the steel grade 780 and 1000 were 8.91 and 5.71  $\mu\text{m}$ , respectively. Though this grain size difference, the strain rate sensitivities of ferrite on both steels were not significantly deviated. This was in accordance to the results in (Okitsu and Tsuji 2014) which showed that effect of ferritic grain size on dynamic tensile properties of examined low carbon steels was small and could be omitted.

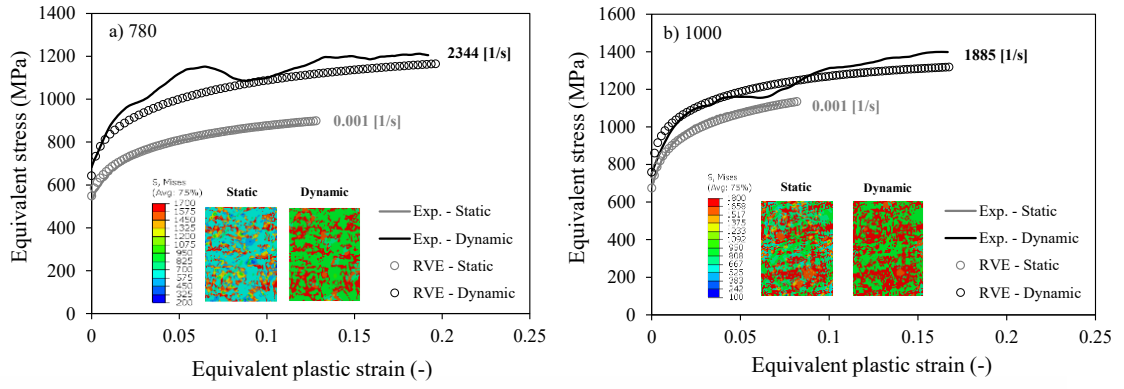


**Figure 5.6** Flow stress curves of steel grades (a) 780 and b) 1000 at different strain rates obtained by experiments and RVE simulations in comparison.

#### 5.4 Ductile damage criterion for micromechanical modelling

Ductile damage criterion in this case was employed for predicting crack initiation and crack propagation for ferritic-martensitic microstructure in DP steels at different strain rates. Identification and determination of damage criterion for each phase ferrite and martensite was described in this topic. Damage criterion in this work used for predicting damage behavior of deformation microstructure under high strain rate deformation by including strain rate function of the Johnson-Cook damage model (Johnson and Cook 1985). Damage criterion is defined to be depended on the equivalent plastic strain rate:

$$\varepsilon_p^f = \varepsilon_\eta^f [\eta] \varepsilon_\dot{\varepsilon}^f [\dot{\varepsilon}_p] \quad (5.7)$$

With the Johnson-Cook rate-dependent damage model multiplier

$$\varepsilon_\dot{\varepsilon}^f [\dot{\varepsilon}_p] = 1 + d_4 \ln \left( \frac{\dot{\varepsilon}_p}{\dot{\varepsilon}_0} \right) \quad (5.8)$$

##### 5.4.1 Determination of static damage loci for martensite

To generate damage curve for the martensitic phases in DP steels under static load, heat treatment with subsequent quenching of carbon steels with different carbon contents were firstly performed. The carbon steels were chosen with regard to the carbon contents in martensite of the examined steel grades 780 and 1000, which are 0.287% and 0.338%, respectively. Note that they were previously calculated by means of phase diagrams obtained by ThermoCalc and the rule of mass balance. The carbon

percentages of three selected steels were about 0.209%, 0.294%, and 0.494% and thus covered those of martensite in the DP steels. The steel samples were heated to the austenitization temperatures and then rapidly cooled down to room temperature by water quenching, in which the martensitic transformation took place. The heat treatment parameters for each steels were defined according to the phase diagrams and the amounts of carbon, as given in table 5.2. It was seen that all heat-treated steels exhibited a fully martensitic microstructure, as shown in figure 5.7. These steel samples were then used to represent the martensitic phases with various carbon contents in the investigated DP steels.

**Table 5.2** Used heat treatment parameters for generating fully martensitic steels with different carbon contents.

Carbon steels	Temperature (°C)	Heat treatment time (min)
%C 0.209	900	15
%C 0.294	875	30
%C 0.494	850	30



**Figure 5.7** Observed microstructure of quenched fully martensitic steel in different carbon contents of (a) 0.209%, (b) 0.294%, and (c) 0.494%.

Subsequently, quasi-static tensile tests of quenched martensitic steels were carried out by using the standard sample ASTM E8. The tensile stress-strain curves of the martensitic samples were determined and are compared with the modelled single phase flow curves of martensite in the examined DP steels, as illustrated in figure 5.8. It is seen that the stress-strain curves of martensite in both steel grades fitted well within the range of resulted stress-strain responses of heat-treated martensitic steels.

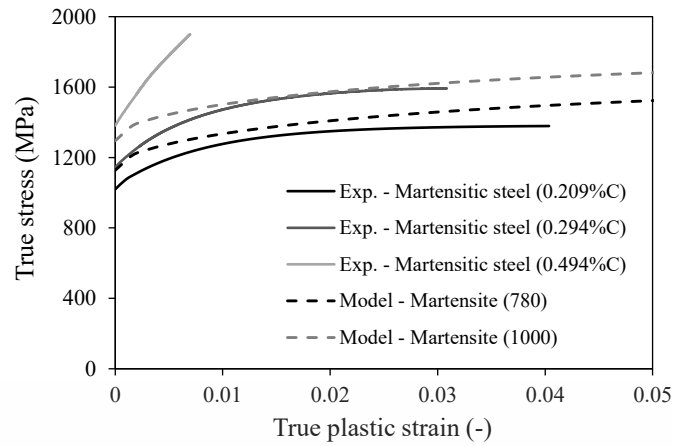


**Figure 5.8** Stress-strain curves of quenched martensitic steels with different carbon contents in comparison with modelled single phase flow curves of martensite in the investigated DP steels.

In addition, local equivalent plastic strains of the quenched samples were gathered during the tensile tests by using a DIC technique similar to (Srithananan, Kaewtatip, and Uthaisangasuk 2016). The maximum occurred plastic strains at prior fracture of all deformed martensitic samples were obtained and plotted against their corresponding carbon contents, as shown in figure 5.9. It is obvious that an increase of carbon content of martensite led to a decrease in equivalent plastic strain at prior fracture.

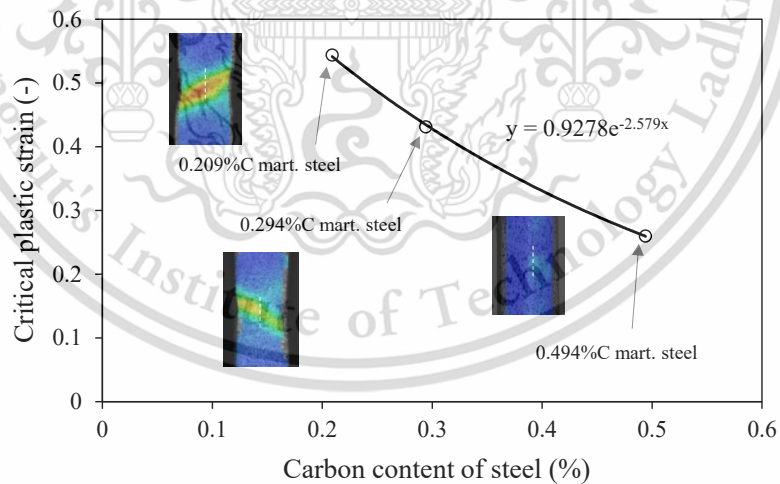


**Figure 5.9** Determined relationship between equivalent plastic strain at prior fracture and carbon percentage of martensitic steels.

For generating damage locus as a function of stress triaxiality and critical plastic strain, experimental quasi-static tensile tests with DIC technique at varying stress states of the quenched martensitic steels was additionally carried out. As reported in several works (Bai and Wierzbicki 2008; Bao and Wierzbicki 2004; Charoensuk, Panich, and Forbiden to modify the content, and cite the document when use.

Uthaisangsuk 2017), tensile samples with different geometries showed significantly different fracture mechanisms as well as resulted critical strains. Hereby, the martensitic steel with 0.209%C was used to identify the damage criterion. Five various tensile specimens, namely, pure shear ( $\eta \sim 0$ ), combined shear ( $\eta \sim 0.2$ ), uniaxial tensile ( $\eta \sim 0.33$ ), uniaxial with hole ( $\eta \sim 0.47$ ) and U-notched ( $\eta \sim 0.65$ ) specimens, as demonstrated in figure 5.10, were taken into account for representing the stress triaxiality range between around 0 and 0.66. In parallel, FE simulations of tensile tests were performed for all used specimens and local stress triaxialities were then calculated similar to those done in (Srithananan, Kaewtatip, and Uthaisangsuk 2016). In the simulations, von Mises yield function and static elastic-plastic properties from the experiments were given. Figure 5.11 depicts the distributed equivalent plastic strains measured by DIC and stress triaxialities predicted by simulations for the pure shear specimen at the state of prior fracture. Note that a comparison of local strains from DIC technique and FE results along the path, as shown in figure 5.12, were done for the verification. From the obtained critical plastic strains and stress triaxialities, damage curve of the 0.209%C martensitic steel sample could be generated, as illustrated in figure 5.13. Furthermore, strain distributions of all different specimens from experiments and simulations were also provided. It can be seen that the results were in good agreement.

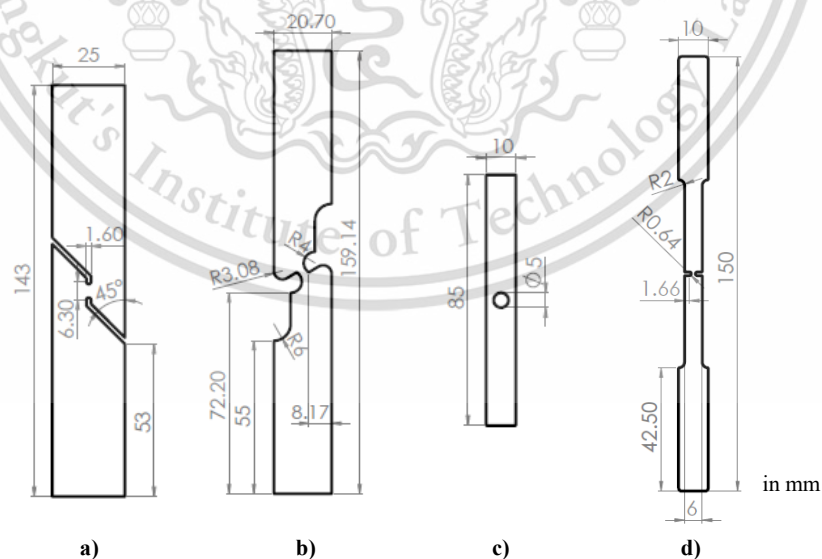


**Figure 5.10** Dimension of (a) pure shear, (b) combined shear, (c) uniaxial with hole, (d) U-notched tensile specimens for determining damage criterion (Srithananan, Kaewtatip, and Uthaisangsuk 2016).

This material is reserved for educational use only, not allowed for commercial use.

Forbidden to modify the content, and cite the document when use.

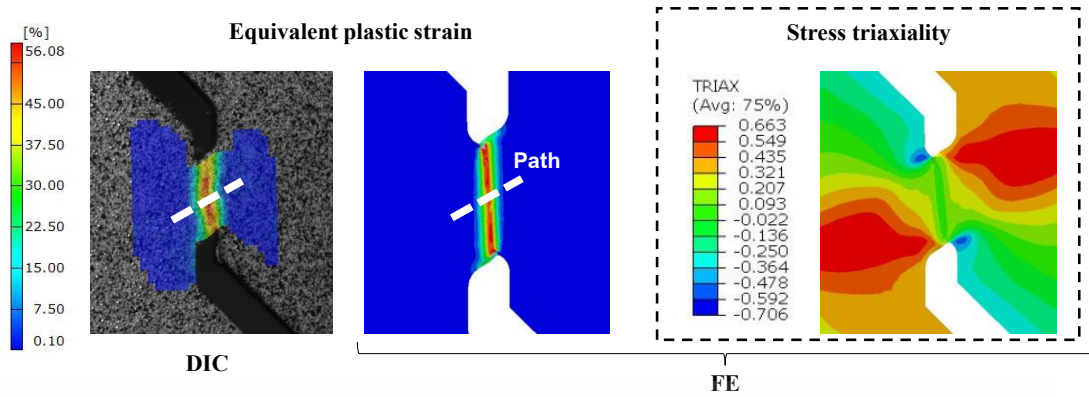


**Figure 5.11** Determined distributions of equivalent plastic strains and stress triaxiality of shear specimen at prior fracture of 0.209%C martensitic steels.

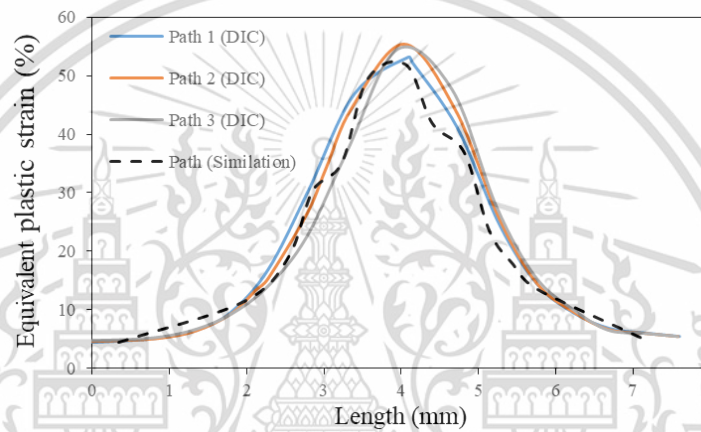


**Figure 5.12** Comparative resulted equivalent plastic strain path from DIC and FE simulation. Note that Path 1, Path 2, Path 3 are repeatable DIC experiments.

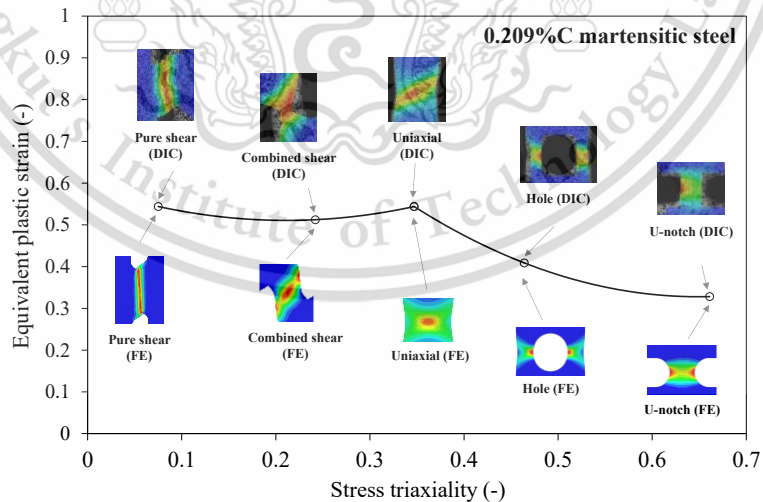


**Figure 5.13** Damage locus determined by DIC and FE simulation for 0.209%C martensitic steel specimen.

Finally, the damage curve of 0.209%C martensitic steel was used as the basis for determining damage loci of martensite in the investigated steels. The exponential

relationship between critical plastic strains at fracture under uniaxial tension and percentage of carbon in figure 5.9 was applied to identify the corresponding critical strains for martensite having different carbon contents. Therefore, the damage criterion was modified to include the term of carbon content, as expressed in the equation (5.9). Then, the entire damage curves of each martensitic phases in steel grade 780 and 1000 could be obtained according to their calculated percentage of carbon, as shown in figure 5.14. The strain at fracture in the case of uniaxial tension was as high as that of shear state. This triaxiality-dependent damage behaviour was similar to those of other martensitic steels in other works (Deole, Barnett, and Weiss 2018; Raath et al. 2018). Note that it was assumed that the dependencies between the critical strain at prior fracture and carbon content were similar for all stress triaxiality value in this work. However, this assumption should be more precisely examined in the future.

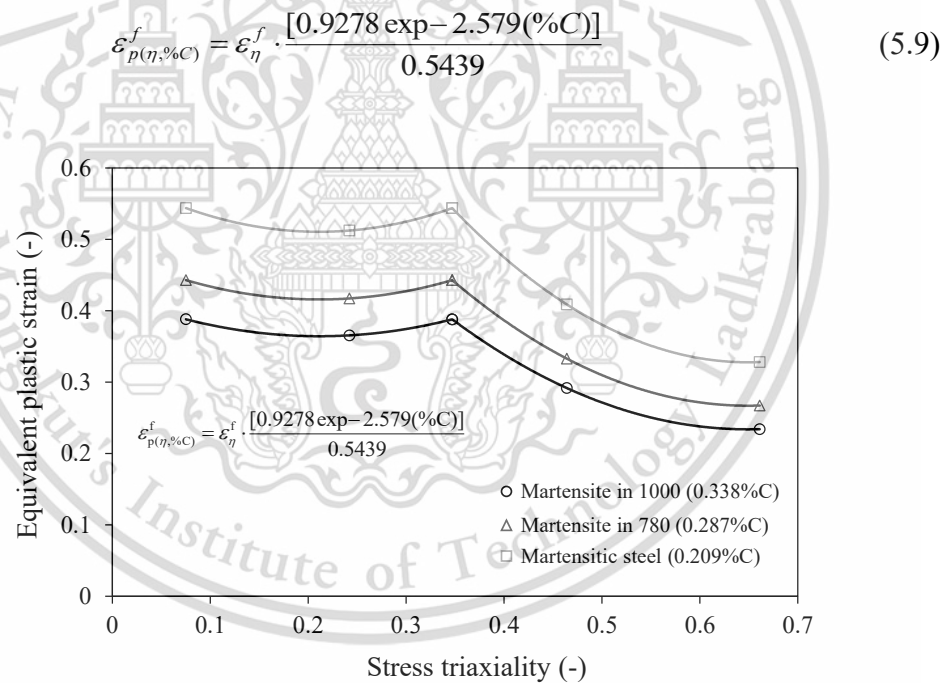


**Figure 5.14** Determined damage loci for martensite with various carbon percentages in investigated steels.

#### 5.4.2 Determination of static damage loci for ferrite

In (Charoensuk, Panich, and Uthaisangsuk 2017), crack initiations in DP steels were identified by means of a direct current potential drop (DCPD) method. Hereby, the DCPD method was employed with tensile tests of different samples and respective FE simulations to generate static damage curve for the crack initiation of steels. By

metallographic examination of deformed specimens at the crack initiation state, it was observed that small voids and micro-cracks mostly occurred in the ferritic matrix close to phase boundaries. The determined damage loci for crack initiation in (Charoensuk, Panich, and Uthaisangsk 2017) could be applied in the current work as a damage criterion of ferrite in the investigated DP steels. However, these damage initiation curves were corresponded to macroscopic equivalent plastic strains of tested tensile samples. Hence, RVE simulations of ferritic-martensitic microstructures of steels were conducted under various states of stress such as pure shear ( $\eta \sim 0$ ), combine shear ( $\eta \sim 0.2$ ), uniaxial ( $\eta \sim 0.33$ ), plane strain ( $\eta \sim 0.45$ ) and biaxial ( $\eta \sim 0.6$ ) by varying uniform loads  $F_1$  and  $F_2$ , as demonstrated in figure 5.15. The detailed boundary condition at various state-stresses by varied uniform load  $F_1$  are presented in table 5.3, as recommend by literatures (T. Sirinakorn, Wongwises, and Uthaisangsk 2014; Srithananan, Kaewtatip, and Uthaisangsk 2016). Afterwards, average equivalent plastic strains of ferritic regions in deformed RVEs were gathered at the states of crack initiation or when the overall plastic strains were equal to the critical strains of referred damage loci. Such plastic strains obtained from RVE simulations under different stress states were used as the critical strains of ferrite on the microstructure level.

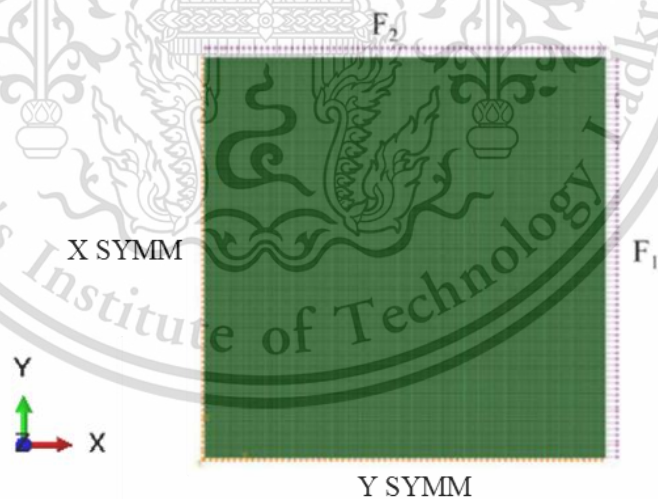


**Figure 5.15** Boundary condition for RVE simulations under various loading.

Then, the damage curves of ferrite in steel grade 780 and 1000 could be generated and are compared with those referred curves of corresponding steels, as illustrated in figure 5.16(a) and (b), respectively. It is seen that the damage curves of ferrite in both steel

This material is reserved for educational use only, not allowed for commercial use.

Forbidden to modify the content, and cite the document when use.

grades significantly higher than the overall damage curves of respective steels, especially at low triaxiality region because of the existence of hardly formed martensite. The difference was slightly higher in case of grade 1000, which contained larger amount of martensite.

**Table 5.3** The values of applied uniform loads  $F_1$  and  $F_2$  for different stress triaxialities.

$F_1$	$F_2$	Stress triaxiality ( $\eta$ )
-1	1	0
-0.29	1	0.2
0	1	0.33
0.23	1	0.45
0.57	1	0.6

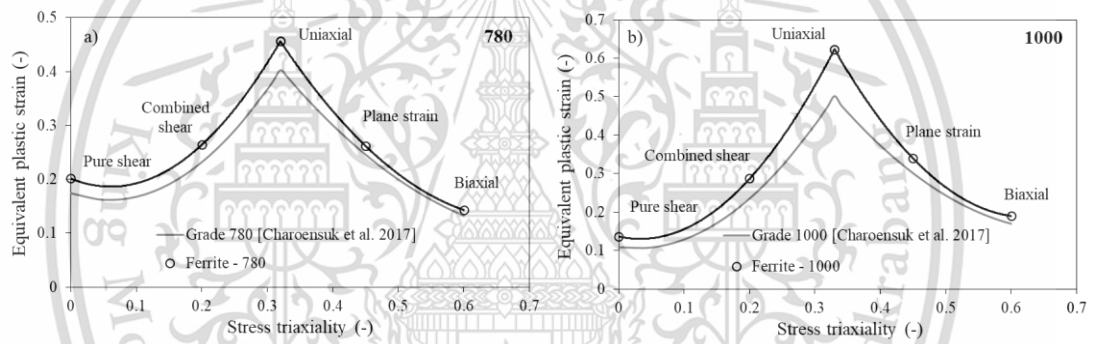


**Figure 5.16** Damage loci for ferrite in steel grade (a) 780 and (b) 1000 determined by RVE simulations coupled with the data from (Charoensuk, Panich, and Uthaisangsuk 2017).

### 5.4.3 Rate-dependent damage locus

Furthermore, for describing damage behaviour of steels under various strain rates on the microstructure level rate-dependent damage curves were determined in this work according to the equation (5.8). Therefore, the JC rate-dependent damage parameters ( $d_4$ ) needed to be identified for both ferrite and martensite in the DP steels. It was reported in (Alturk et al. 2017) that the differences of rate-dependent mechanical characteristics of various DP steels were significantly due to the combined phase fraction of soft and hard phase. Thus, the strain rate sensitivity for damage of each phases in the investigated steels were assumed to be similar here. For ferrite, the parameter  $d_4$  was taken from the results in (Børvik et al. 2005). For martensite,

This material is reserved for educational use only, not allowed for commercial use.

Forbidden to modify the content, and cite the document when use.

experimental tensile tests at various strain rates of the 0.209%C fully martensitic steel were performed. Then, the parameter  $d_4$  was derived from the resulted stress-strain curves and local strains measured by DIC technique, as illustrated in figure 5.17(a). It is seen that increasing strain rates led to enhanced fracture elongations of martensitic samples.

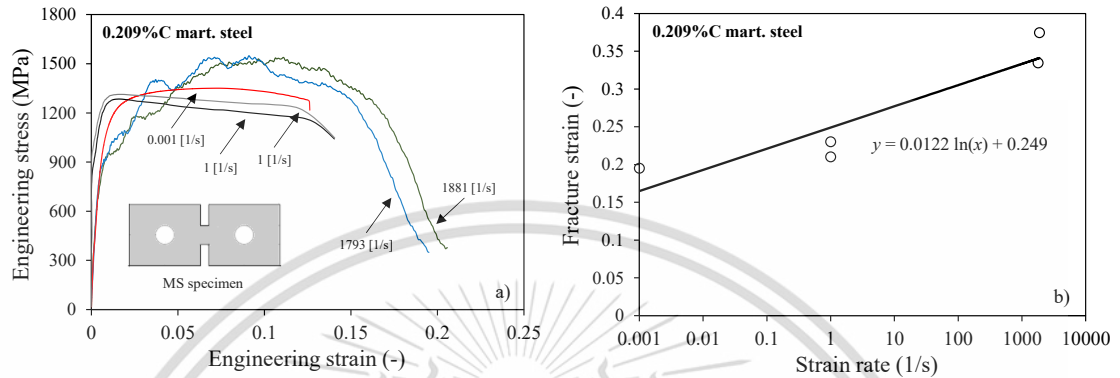


**Figure 5.17** (a) Determined stress-strain curves at different strain rates of 0.209%C martensitic steel and (b) relationship between fracture strain and strain rate.

The relationship between determined equivalent plastic strains at fracture and applied strain rates of martensitic steel is depicted in figure 5.17(b), which could be used to calculate the JC rate-dependent damage parameter  $d_4$ . Then, the parameters  $d_4$  identified for the investigated DP steels are listed in table 5.4. It is obvious that the strain rate sensitivity for damage of ferrite was less than zero. It meant that the soft ferritic phase in DP steels showed decreased elongation at high strain rate condition, as also described in (Yu, Guo, and Lai 2009). In contrast, the hard martensitic phase exhibited increasing fracture strains under high strain rate deformation, as it showed the positive strain rate sensitivity for damage. Finally, these rate-dependent parameters were applied to obtain the damage loci at different strain rates for ferrite and martensite in both steel grades, as summarized in figure 5.18, which were further used for RVE simulations at varying strain rates

**Table 5.4** Identified JC damage model parameter ( $d_4$ ) for the individual phases in DP steels.

Phase	JC damage model parameter ( $d_4$ )
Ferrite	-0.0150 (Børvik et al. 2005)
Martensite	0.0122

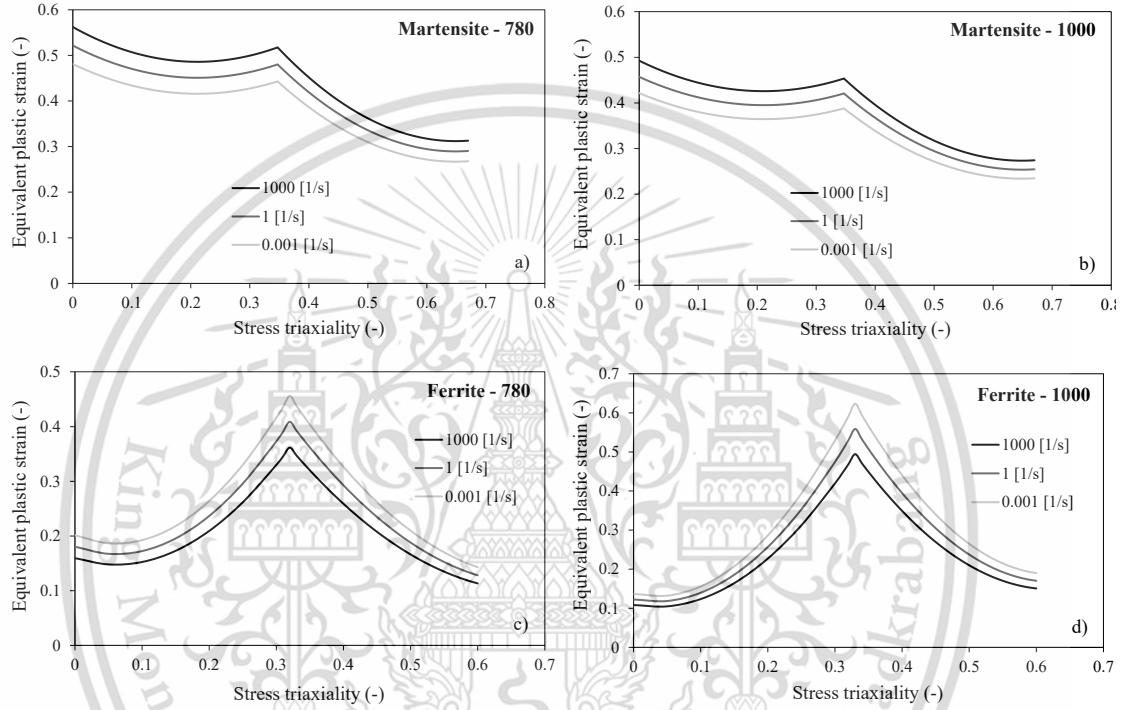


**Figure 5.18** Determined rate-dependent damage loci for martensite in (a) grade 780 and (b) 1000 and for ferrite in (c) grade 780 and (d) grade 1000.

#### 5.4.4 Damage initiation and damage evolution in RVE simulation

In RVE simulations of the examined DP microstructures, damage initiation was described by using the damage criterion, as expressed in the equation (5.7). It represented the equivalent plastic strain at the onset of damage. Hereby, the damage history variable was defined as following:

$$\omega_D = \int \frac{d\varepsilon_p^f}{\varepsilon_p^f[\eta, \dot{\varepsilon}_p^f]} \quad (5.10)$$

Where  $\omega_D$  is damage indicator which is presented by the integral of the weighted accumulative equivalent plastic strain and the weighting function  $\varepsilon_p^f[\eta, \dot{\varepsilon}_p^f]$ . If  $\omega_D$

This material is reserved for educational use only, not allowed for commercial use.

Forbidden to modify the content, and cite the document when use.

was greater than 1, the onset of progressive damage function was triggered. In this work, a linear damage evolution, which was represented by the stiffness degradation variable (SDEG), was employed for predicting crack occurrence and propagation. Hereby, the stiffness of material was continuously degraded during further deformation after damage initiation took place. If the SDEG was then equal to 1, the concerned element was completely damaged and removed from the model (Hillerborg, Modéer, and Petersson 1976). This SDEG variable could be thus used to monitor progressive damage behavior of microstructure in the RVE simulations. In this work, the linear damage evolution was defined as a function of equivalent plastic displacement. The damage evolution parameters could be identified from the damage-induced softening part of experimental tensile stress-strain curves coupled with the smallest used element size of RVE model as also done in (Abaqus 2012; Biswas and Ding 2015; Dzugan et al. 2012; Li and Wierzbicki 2010). For ferrite in both grades 780 and 1000, the damage evolution parameters were derived from the previous results in (Charoensuk, Panich, and Uthaisangsuk 2017), in which equivalent plastic strains at crack initiation and final fracture of DP steels were taken into account. Moreover, it was reported in (Alturk et al. 2017; Borvik et al. 2001) that the failure softening parts of ferritic steel obtained from experimental tensile tests at various strain rates were just slightly different. Therefore, the same damage evolution parameters were given for the ferritic phase in examined steels under quasi-static and high strain rate condition. Additionally, microstructures of both steel grades after quasi-static deformation obviously exhibited martensite cracking similar to that found in (Ramazani et al. 2016). In the case of martensite, the damage evolution parameter for static condition was thus set to be zero due to its brittle characteristic and no noticeable softening part. Nevertheless, the evolution parameter for dynamic condition of martensite was directly determined from the damage-induced softening part of experimental tensile stress-strain curves of the 0.209%C martensitic steel at high strain rate, shown in figure 5.17. It could be observed that ferrite exhibited damage initiation at lower critical plastic strains, but its damage evolution required larger plastic deformation than martensite.

## CHAPTER 6

### SIMULATION RESULTS AND DISCUSSIONS

RVE simulations, in which damage criteria were applied individually for each phases, were carried out under uniaxial tension deformation with quasi-static ( $0.001 \text{ s}^{-1}$ ) and high strain rate ( $1000 \text{ s}^{-1}$ ) condition. Then, local deformation and damage occurrence of the examined ferritic-martensitic microstructures were investigated, as depicted in figure 6.1. Hereby, the results of both static and dynamic conditions were taken from the similar overall deformation. Note that the rate-dependent terms and their parameters for strain hardening and damage initiation were only used for the RVE simulations subjected to high strain rate. It is seen that predicted local stresses in the microstructures under high strain rate were somewhat higher than those under static load in both steels. The damage appearance sites from the static and dynamic simulations were similar in the case of grade 780, while the grade 1000 under static and dynamic loading showed obviously different damage initiations in terms of site and magnitude.

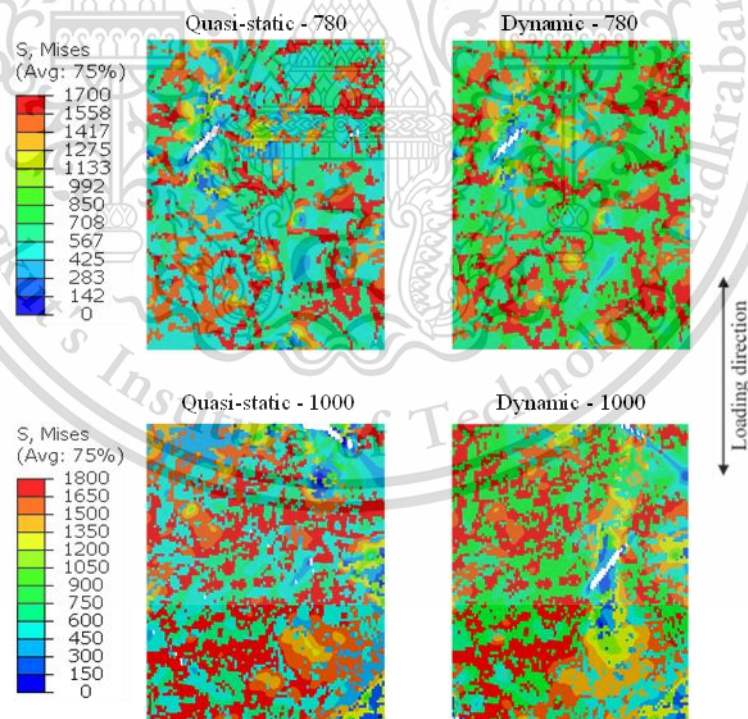


**Figure 6.1** Resulted local stresses and damage appearance by RVE simulations for steel grade 780 and 1000 under uniaxial deformation at different strain rates.

The predicted damage developments in microstructures of steel grade 780 were further investigated at larger deformation state, as depicted in figure 6.2 and figure 6.3, for the static and dynamic conditions, respectively. Figure 6.4 and figure 6.5 show the calculated damages in microstructures of grade 1000 at the onset of damage and damage propagation under static and dynamic load, respectively. It was observed that by static loading emerging damage initiation and its progression characteristics in the microstructure of grade 780 and 1000 were rather similar. At the early state of damage initiation, both interfacial decohesion between ferrite and martensite and martensite cracking were found. The damages also directly took place in the ferritic matrix. The martensite cracking sites were small and well distributed all over the microstructure. Note that after the interfacial decohesion damage propagated preferably through the ferrite regions. This predicted damage onset behaviour under static load well agreed with the results observed by SEM, as presented in section 4.3, and was also in accordance with the finding of other works (Ramazani et al. 2016; Anbarlooie and Kadkhodapour 2018; Ghadbeigi et al. 2010). Afterwards, the damages induced by void occurrence in ferrite and at the ferrite/martensite interfaces further propagated along high plastic deformation zone or localized shear bands, as illustrated for grade 780 and 1000 in figure 6.2 and figure 6.4, respectively that was similar to those reported in (Avramovic-cingara et al. 2009). The damage appearances in the microstructure of steel grade 780 and 1000 under high strain rate loading predicted by RVE simulations were also similar, as depicted in figure 6.3 and figure 6.5. Hereby, damage onsets were solely caused by voids in ferrite and interfacial decohesion, as also shown in (Xu et al. 2019). No noticeable martensite cracking was observed at high strain rate in contrast to the static condition. This was due to the adiabatic softening effect which was indirectly considered in the determined damage criteria of martensite. Hence, within some large martensite particles, micro-damages could be occurred and enlarged, as seen in the SEM results in figure 4.4. Subsequently, for both steels damage propagations at high rate took place through the plastic shear bands, as demonstrated in figure 6.3 and figure 6.5. The differences of damage propagations in steel grade 1000 subjected to static and dynamic loading were more significant than those of grade 780 that could be due to the larger phase fraction of martensite and its rate-dependent damage behaviour. It is noticed that a regular mesh was used in this work and the type of mesh also likely affected the local damage predictions. The effect of varied mesh size would be investigated in the future.

Th educational use only, not allowed for commercial use.

Forbidden to modify the content, and cite the document when use.

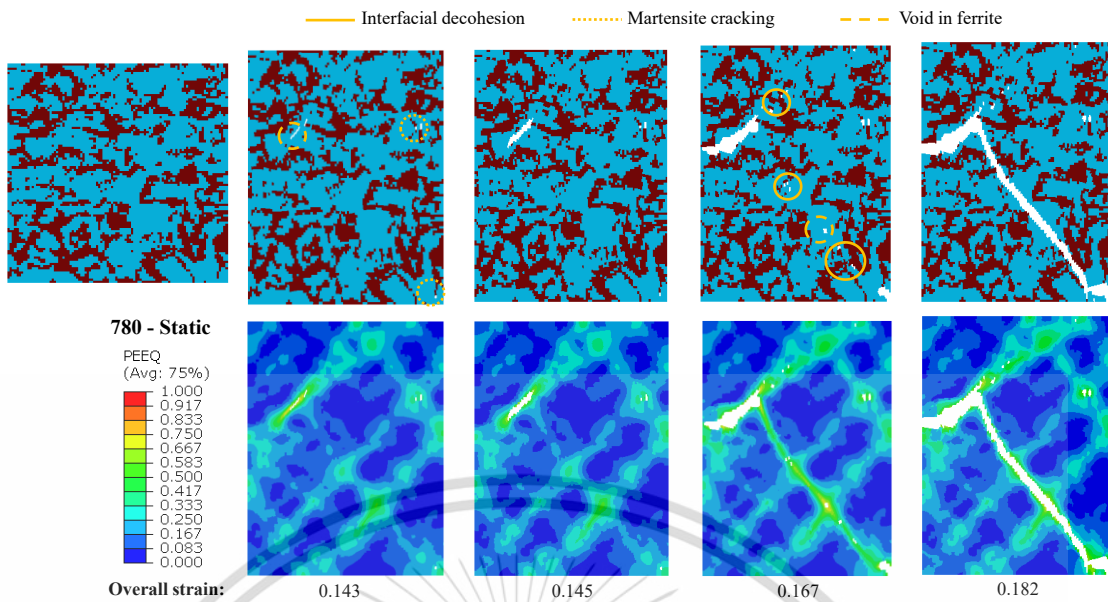


**Figure 6.2** Damage initiation, damage propagation and strain distributions in microstructure of grade 780 under quasi-static loading predicted by RVE simulations.

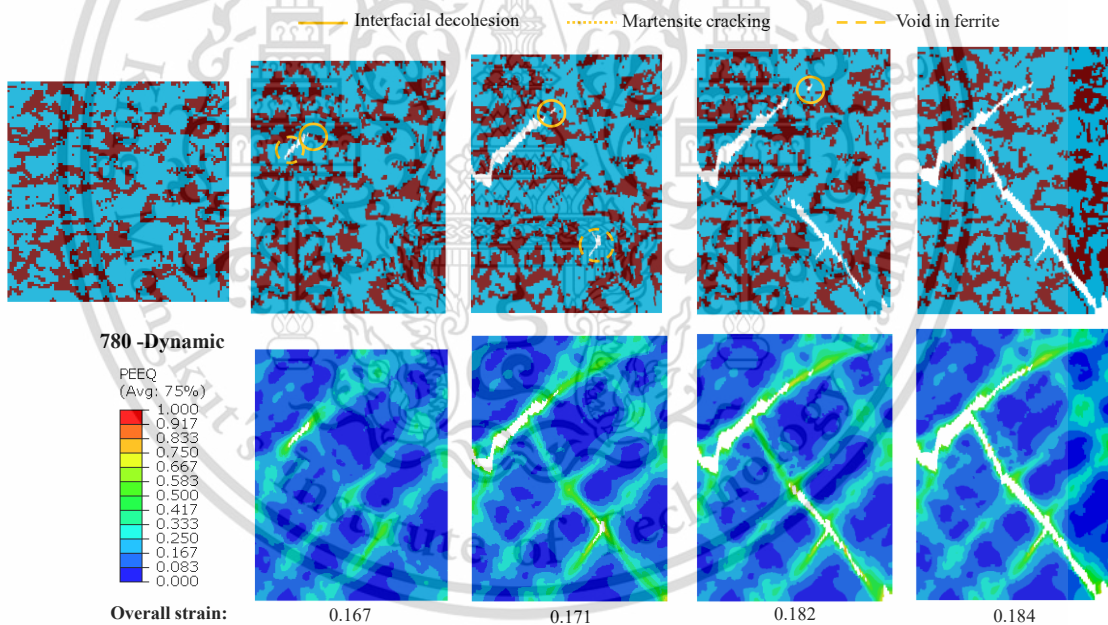


**Figure 6.3** Damage initiation, damage propagation and strain distributions in microstructure of grade 780 under high strain rate loading predicted by RVE simulations.

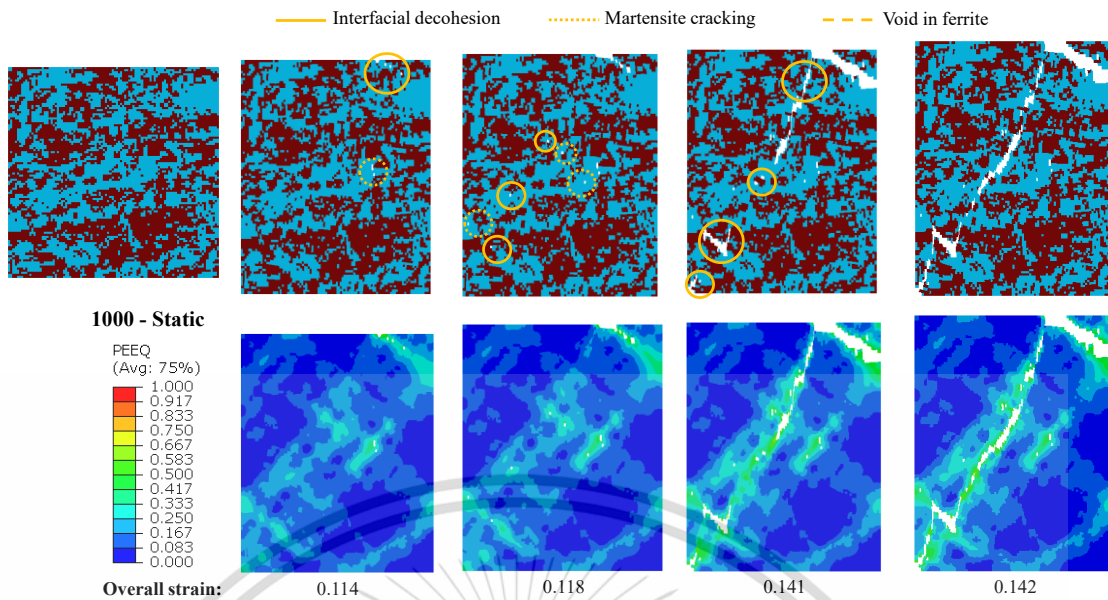


**Figure 6.4** Damage initiation, damage propagation and strain distributions in microstructure of grade 1000 under quasi-static loading predicted by RVE simulations.

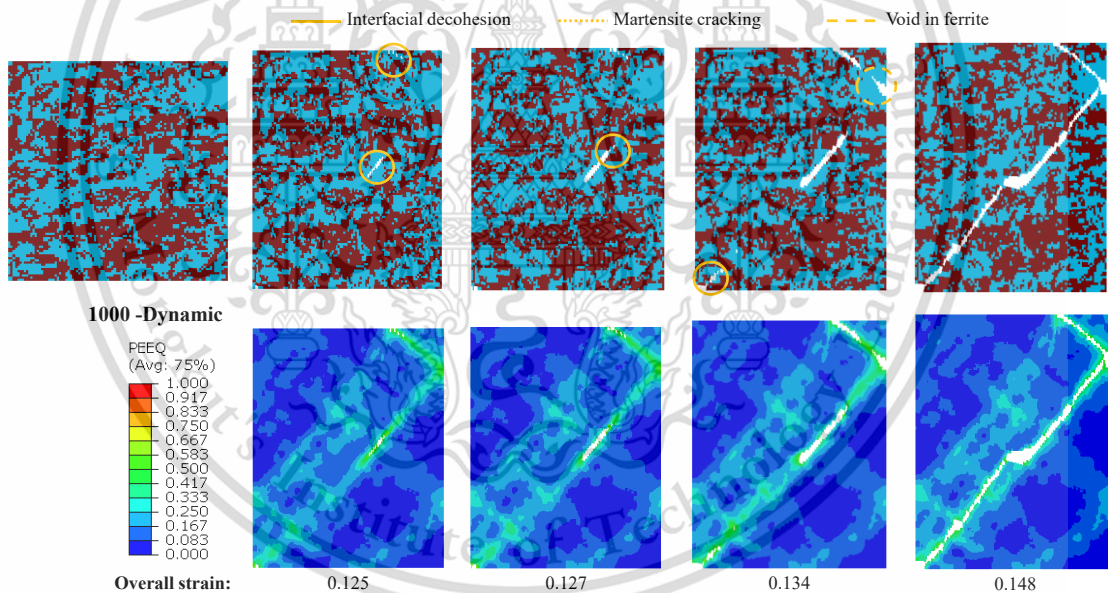


**Figure 6.5** Damage initiation, damage propagation and strain distributions in microstructure of grade 1000 under high strain rate loading predicted by RVE simulations.

Moreover, the amount of damaged areas in the examined microstructures under static and dynamic loading were determined. Note that an element in RVE, whose damage variable ( $\omega_D$ ) or DUCTRT value has reached 1, was considered to be the damage area. The developments of percentages of damaged area in ferrite and martensite of RVE during uniaxial tension under quasi-static and high strain rate condition are depicted in

This material is reserved for educational use only, not allowed for commercial use.

Forbidden to modify the content, and cite the document when use.

figure 6.6 and figure 6.7 for grade 780 and 1000, respectively. The characteristic damage and plastic strain distributions at the crack propagation state were also shown for both loading conditions. It is seen that the percentages of damaged sites in ferrite and martensite of both steels increased with increasing applied plastic strain. Nevertheless, the number of damage sites in martensite was significantly lower. It meant that damage evolution particularly occurred in the ferritic matrix independent on the phase fraction of steels. Under dynamic loading, damage evolution rates of ferrite were obviously higher than those under static load. In contrast, the increasing rates of damages of martensite in both steels at high strain rate were lower. This was due to that under dynamic condition martensite became more ductile and thus exhibited failure at larger plastic strains that was similar to the results in (W. Wang et al. 2013; Alturk et al. 2017).

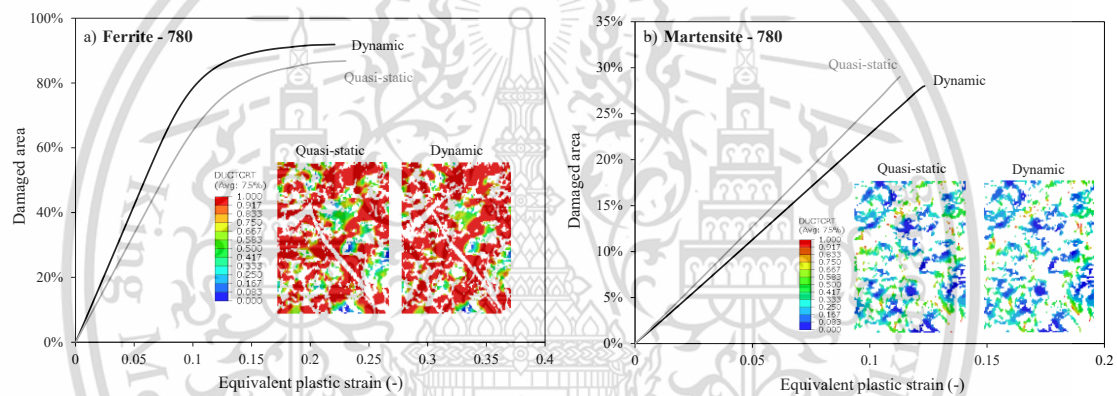


**Figure 6.6** Percentages of damaged areas and distributions of damage variables and equivalent plastic strains at the overall strain 0.182 in (a) ferrite and (b) martensite of steel grade 780.

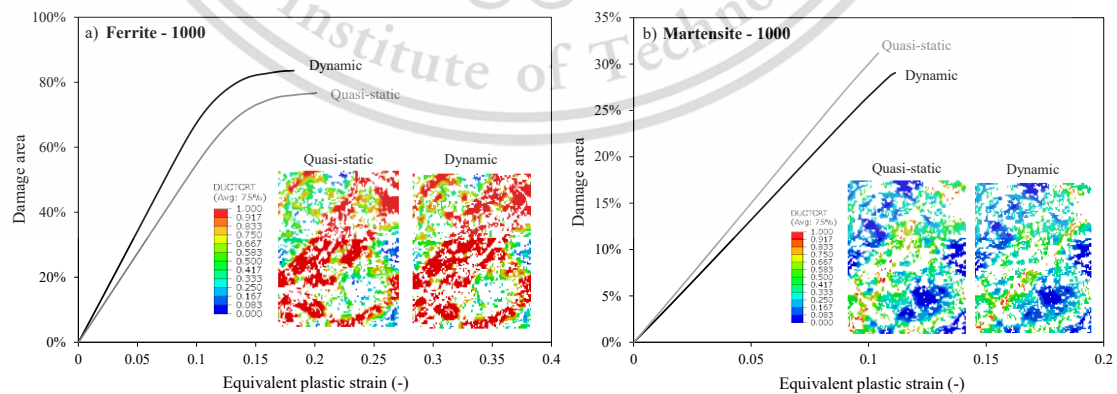


**Figure 6.7** Percentages of damaged areas and distributions of damage variables and equivalent plastic strain at the overall strain 0.146 in (a) ferrite and (b) martensite of steel grade 1000.

This material is reserved for educational use only, not allowed for commercial use.

Forbidden to modify the content, and cite the document when use.

Additionally, stress-strain responses of ferrite and martensite in the microstructures of examined steels under quasi-static and high strain rate loading obtained from RVE simulations were investigated and compared in figure 6.8. Obviously, flow stresses of ferrite were greatly increased with rising strain rate for both DP steels, whereas those of martensite rarely changed. This was in accordance to the given strain rate sensitivities for strain hardening of each phases. On the other hand, with increasing strain rate predicted ductilities of martensite in both steels were certainly increased, while those of ferrite were slightly lowered. This was also due to the rate-dependent multipliers for damage defined for both phases that was in agreement with (W. Wang et al. 2013; Alturk et al. 2017).

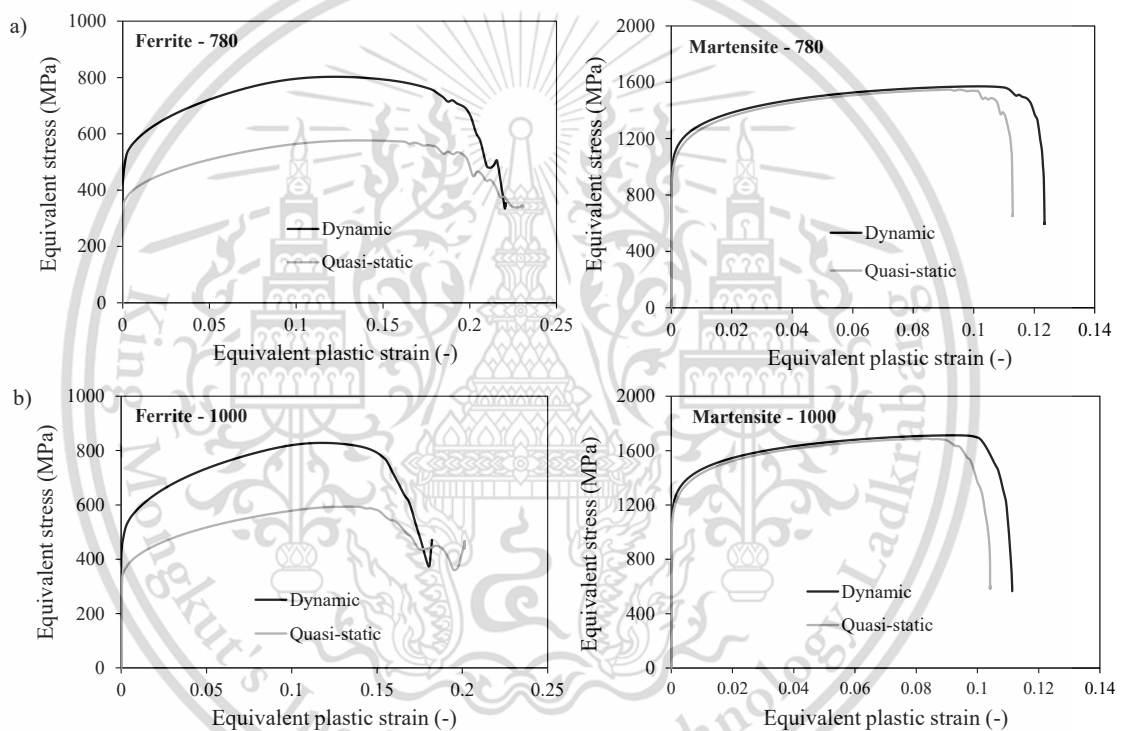


**Figure 6.8** Calculated stress-strain responses of ferrite and martensite in steel grade (a) 780 and (b) 1000 under loading with different strain rates obtained by RVE simulations.

Finally, the overall stress-strain curves of examined steels at static and high strain rate condition gathered from experiments and RVE simulations were compared, as illustrated in figure 6.9. It is seen that the stress-strain behaviors of steels at varying strain rates could be fairly described by the RVE simulations. Note that the failure strains of calculated stress-strain curves described the failure of RVEs on the micro-scale, in which final crack reached a length of around 25  $\mu\text{m}$ . Hence, these failure states were rather referred to crack initiation states of the macroscopic sample level. They

This material is reserved for educational use only, not allowed for commercial use.

Forbidden to modify the content, and cite the document when use.

were strongly affected by the different local stress-strain and damage characteristics at varying strain rates of both phases. The phase fraction of ferrite and martensite in steels played the dominant role for the overall strain hardening and ductility at elevated strain rates of DP steels. The introduced micromechanical approach can be employed to study effects of microstructure characteristics and their individual mechanical behaviors on the macroscopic properties of DP steels.

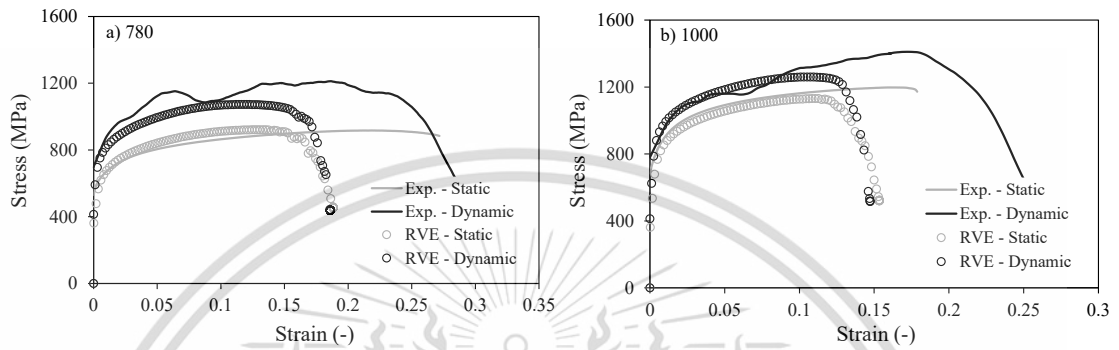


**Figure 6.9** Overall stress-strain curves of steel grade (a) 780 and (b) 1000 under static and dynamic loading from experimental tensile tests and RVE simulations.

## CHAPTER 7

### CONCLUSIONS

In this work, experimental tensile tests at different strain rates were conducted for the AHS steel grade 780 and 1000. The effects of strain rate on strength, ductility, local crack mechanism and fracture behaviour were investigated. 2D RVE simulations were carried out for the examined steels, in which dislocation density based hardening model and JC damage model were applied for the individual phases. Furthermore, the JC rate-dependent parameters for strain hardening and damage were also incorporated. The damage loci of ferrite were determined on the basis of experimental results of previous work, while those of martensite were obtained by using the quenched martensitic samples with different carbon contents. The results of experiments and simulations were compared and correlated. The findings of this work is given as following.

- Both DP steel grades exhibited increased yield, tensile strengths as well as elongations when subjected to higher strain rate. The grade 780 showed a larger strain rate sensitivity than the grade 1000, whereas effect of strain rate on the ductility of grade 1000 was more significant.
- The damage initiation in microstructures of steels under quasi-static loading was caused by micro-voids in ferrite, interfacial decohesion and martensite cracking, while at high strain rate only interfacial decohesion and voids in ferrite occurred and no martensite cracking was observed. This was affected by the adiabatic softening on microstructure level so that the formation of martensite cracking changed to ductile deformation at large strain rate.
- The dimple size at fracture surface of grade 780 became noticeably larger with increasing strain rate. It was due to the higher void growth rate of steel with lower martensitic phase fraction. This higher growth rate was governed by local plastic flow ability in the microstructure and thus related to the higher strain rate hardening of grade 780 than grade 1000. The amount of cleavage planes at static deformation were higher than that at high strain rate in case of grade 1000.
- The results of RVE simulations coupled with the rate-dependent hardening and damage model fairly described the overall stress-strain responses and observed

This material is reserved for educational use only, not allowed for commercial use.

Forbidden to modify the content, and cite the document when use.

damage occurrences in the microstructures of both steels. The strain rate hardening and ductility characteristics of each phases at varying strain rates and their interactions strongly affected the mechanical properties of steels. The phase fraction played a dominant role on both strain hardening and deformability of DP steels at elevated strain rates.



This material is reserved for educational use only, not allowed for commercial use.

Forbidden to modify the content, and cite the document when use.

## REFERENCES

- Autocarindia. (2015, September 3). Volvo XC90 gets full mark at Euro-NCAP. Retrieved from <https://www.autocarindia.com/car-news/volvo-xc90-gets-full-marks-at-euro-ncap-397267>
- RDN. (2015, July 8). Steel ‘debate’ guest column: The future for steel in the automotive industry. Retrieved from <https://www.autocarindia.com/car-news/volvo-xc90-gets-full-marks-at-euro-ncap-397267>
- D. Lukaszewicz, S. Hesse, L. Graff, S. Kerscher, L. Deobald, C.Y. Park, N. Desai. (2014). A Design and Analysis Method for Automotive and Aerospace Composite Structures including Manufacturing Variations. Proc. of the American Society for Composites 29<sup>th</sup> Conference, Sept. 2014.
- J. Lian, W. Liu, I. Papadioti, I. Bellas, S. Chandran, P. Verleysen, H. Richter, N. Aravas, S. Munstermann. (2018). Plasticity and failure behavior modeling of high-strength steels under various strain rates and temperatures: microstructure to components. *Procedia Structural Integrity* 13 1421–1426. <https://doi.org/10.1016/j.prostr.2018.12.295>
- C.W. Isaac, O. Oluwole. (2015). Finite Element Comparative Analysis of Crushing Behaviour of Square Steel Tubes. *International Journal of Scientific & Engineering Research*, Volume 6, Issue 7, July-2015.
- Abaqus Acumen. (2017, Jan 10). Johnson-Cook Material model with Damage : Significance and application. Retrieved from <https://stats.video/youtube-channel-statistics/abaqus-acumen>
- Michael Worswick. (2018). Dynamic Considerations in Prediction of Fracture of Ultra High-Strength Steel During Crash. Presented at University of Waterloo, Waterloo, Canada. Retrieved from [https://www.autosteel.org/autosteel\\_org/document-types/great-designs-in-steel/gdis-2018/track-1---worswick---waterloo](https://www.autosteel.org/autosteel_org/document-types/great-designs-in-steel/gdis-2018/track-1---worswick---waterloo)
- Msynk. (2014, February 17). Ultra High Strength Standard Size Steel Tubing. Retrieved from <https://superiorrollforming.wordpress.com/>
- Satyendra. (2014, June 1). Dual Phase Steels. Retrieved from <http://ispatguru.com/dual-phase-steels/>
- C. Salisbury, M. Worswick. (2007). High Rate Deformation of VHB Tapes, Department of mechanical engineering, University of Waterloo, Canada.

- Luciano Avilla Gray. (2013). Material Behaviour under High Strain Rates. Retrieved from <https://www.lcc.mw.tum.de/en/research-groups/material-behavior-and-testing/material-behavior-under-high-strain-rates/>
- J. Bouquerel, K. Verbeken, B.C. De Cooman. (2006). Microstructure-based model for the static mechanical behaviour of multiphase steels. *Acta Mater.* 54 1443–1456.
- S. Münstermann, W. Bleck. (2009). Future design methods for optimised use of modern steels in pressure vessels. Dillinger Pressure Vessel Colloquium, September 16<sup>th</sup> & 17<sup>th</sup>, 2009.
- Y. Bai, T. Wierzbicki. (2015). A comparative study of three groups of ductile fracture loci in the 3D space. *Eng. Fract. Mech.* 135 147–167.  
<http://dx.doi.org/10.1016/j.engfracmech.2014.12.023>
- M. Borsutzki, D. Cornette, Y. Kuriyama, A. Uenishi, B. Yan, E. Opbroek. (2005). Recommendations for Dynamic Tensile Testing of Sheet Steels. International Iron and Steel Institute.
- P.C. Chakraborti, M.K. Mitra. (2007). Microstructure and tensile properties of high strength duplex ferrite–martensite (DFM) steels. *Mater. Sci. Eng. A* 466 123–133.
- A. Fallahi. (2002). Microstructure-Properties Correlation of Dual Phase Steels Produced by Controlled Rolling Process. *J. Mater. Res. Technol.*, Vol.18 No.5.
- Jody N. Hall. (2011, May 18). Evolution of Advanced High Strength Steels In Automotive Applications. General Motors Company, Joint Policy Council, Auto/Steel Partnership. Retrieved from <https://www.autosteel.org/-/media/files/autosteel/great-designs-in-steel/gdis-2011/20---jody-hall---evolution-of-advanced-high-strength-steels-in-automotive-applications.ashx>
- H. Huh, W.J. Kang, S.S. Han. (2002). A Tension Split Hopkinson Bar for Investigating the Dynamic behaviour of Sheet Metals. *Exp. Mech.*, Vol. 42, No. 1, March 2002.
- J. Hyun, J. Hoon, R.H. Wagoner. (2010) A plastic constitutive equation incorporating strain, strain-rate, and temperature. *Int. J. Plastic.* 26 1746–1771.  
<http://dx.doi.org/10.1016/j.ijplas.2010.02.005>
- Shawn Morgans. (2013). Advanced High-Strength Steel Technologies in the 2013 Ford Fusion. Ford Motor Company. Retrieved from <https://www.autosteel.org/-/media/files/autosteel/great-designs-in-steel/gdis-2012/advanced-high-strength-steel-technologies-in-the-2013-ford-fusion.ashx>

- B. Pan, K. Qian, H. Xie, A. Asundi. (2009). Two-dimensional digital image correlation for in-plane displacement and strain measurement: a review. *Meas. Sci. Technol.*, vol. 20, pp. 1-17.
- S. Paul. (2013). Real microstructure based micromechanical model to simulate microstructural level deformation behavior and failure initiation in DP 590 steel. *Mater. Des.* 44 397–406. <http://dx.doi.org/10.1016/j.matdes.2012.08.023>
- K. Sato, Q. Yu, J. Hiramoto, T. Urabe, A. Yoshitake. (2015). A method to investigate strain rate effects on necking and fracture behaviors of advanced high-strength steels using digital imaging strain analysis. *Int. J. Impact Eng.* 75 11-26. <https://doi.org/10.1016/j.ijimpeng.2014.07.001>
- J.H. Kim, D. Kim, H.N. Han, F. Barlat, M.G. Lee. (2013). Strain rate dependent tensile behavior of advanced high strength steels: Experiment and constitutive modeling. *Mater. Sci. Eng. A* 559 222–231. <http://dx.doi.org/10.1016/j.msea.2012.08.087>
- ABAQUS/Analysis user's manual Version 6.10, ABAQUS Inc.
- D. Anderson, S. Winkler, A. Bardelcik, M.J. Worswick. (2014). Influence of stress triaxiality and strain rate on the failure behavior of a dual-phase DP780 steel. *Mater. Des.* 60 198-207. <http://dx.doi.org/10.1016/j.msea.2012.08.087>
- T. Rahman, A. Bardelcik, J. Imbert, C. Butcher, M.J. Worswick. (2016). Effect of strain rate on flow stress and anisotropy of DP600, TRIP780, and AA5182-O sheet metal alloys. *Int. J. Impact Eng.* 88 72-90. <http://dx.doi.org/10.1016/j.ijimpeng.2015.09.006>
- B. Erice, C. Roth, D. Mohr. (2018). Stress-state and strain-rate dependent ductile fracture of dual and complex phase steel. *Mech. Mater.* 116 11-32. <https://doi.org/10.1016/j.mechmat.2017.07.020>
- Y. Chen, A.H. Clausen, O.S. Hopperstad, and M. Langseth. (2011). Application of a split-Hopkinson tension bar in a mutual assessment of experimental tests and numerical predictions, *Int. J. Impact Eng.* 38 824-836.
- N.K. Singh, E. Cadoni, M.K. Singha, N.K. Gupta. (2011). Dynamic tensile behavior of multi phase high yield strength steel, *Mater. Des.* 32 5091–5098. <http://dx.doi.org/10.1016/j.matdes.2011.06.027>
- J. Qin, R. Chen, X. Wen, Y. Lin, M. Liang, F. Lu. (2013). Mechanical behaviour of dual-phase high-strength steel under high strain rate tensile loading, *Mater. Sci. Eng. A* 586 62-70. <http://dx.doi.org/10.1016/j.msea.2013.07.091>

- V. Uthaisangasuk, U. Prael, W. Bleck. (2009). Stretch-flangeability characterisation of multiphase steel using a microstructure based failure modelling, *Comput. Mater. Sci.* 45 617–623. <http://dx.doi.org/10.1016/j.commatsci.2008.06.024>
- A. Ramazani, M. Abbasi, S. Kazemiabnavi, S. Schmauder, R. Larson, U. Prael. (2016). Development and application of a microstructure-based approach to characterize and model failure initiation in DP steels using XFEM, *Mater. Sci. Eng. A* 660 181–194. <http://dx.doi.org/10.1016/j.msea.2016.02.090>
- W. Wang, M. Li, C. He, X. Wei, D. Wang, H. Du. (2013). Experimental study on high strain rate behavior of high strength 600-1000MPa dual phase steels and 1200MPa fully martensitic steels. *Mater. Des.* 47 510–521. <http://dx.doi.org/10.1016/j.matdes.2012.12.068>
- M. Xu, H. Li, R. Jiang, D. Tang, H. Jiang, Z. Mi. (2019). Deformation behavior and microstructural evolution in ultra-high-strength dual-phase (UHS-DP1000) steel with different strain rates. *J. Iron Steel Res. Int.* 26 173-181. <http://link.springer.com/10.1007/s42243-018-0213-1>
- A. Das, M. Ghosh, S. Tarafder, S. Sivaprasad, D. Chakrabarti. (2017). Micromechanisms of deformation in dual phase steels at high strain rates. *Mater. Sci. Eng. A* 680 249–258. <http://dx.doi.org/10.1016/j.msea.2016.10.101>
- H. Yu, Y. Guo, X. Lai. (2009). Rate-dependent behavior and constitutive model of DP600 steel at strain rate from  $10^{-4}$  to  $10^3$ s<sup>-1</sup>, *Mater. Des.* 30 2501–2505. <http://linkinghub.elsevier.com/retrieve/pii/S0261306908005104>
- R. Alturk, S. Mates, Z. Xu, F. Abu-Farha. (2017). Effects of microstructure on the strain rate sensitivity of advanced steels. In: TMS T. (eds) TMS 2017 146th Annual Meeting & Exhibition Supplemental Proceedings. The Minerals, Metals & Materials Series. Springer, Cham, pp 243-254. [https://doi.org/10.1007/978-3-319-51493-2\\_24](https://doi.org/10.1007/978-3-319-51493-2_24)
- X. Sun, K.S. Choi, W.N. Liu, M.A. Khaleel. (2009). Predicting failure modes and ductility of dual phase steels using plastic strain localization. *Int. J. Plastic.* 25 1888–1909. <http://dx.doi.org/10.1016/j.ijplas.2008.12.012>
- T. Sirinakorn, S. Wongwises, V. Uthaisangasuk. (2014). A study of local deformation and damage of dual phase steel. *Mater. Des.* 64 729–742. <http://dx.doi.org/10.1016/j.matdes.2014.08.009>
- P. Srithananan, P. Kaewtatip, V. Uthaisangasuk. (2016). Micromechanics-based modeling of stress-strain and fracture behavior of heat-treated boron steels for hot stamping process. *Mater. Sci. Eng. A* 667 61–76. <http://dx.doi.org/10.1016/j.msea.2016.04.065>

- A.Ch. Darabi, H.R. Chamani, J. Kadkhodapour, A.P. Anaraki, A. Alaie, M.R. Ayatollahi. (2017). Mechanics of Materials Micromechanical analysis of two heat-treated dual phase steels : DP800 and DP980, *Mech. Mater.* 110 68–83. <http://dx.doi.org/10.1016/j.mechmat.2017.04.009>
- G.R. Johnson, W.H. Cook. (1983). A constitutive model and data for metals subjected to large strains, high strain rates and high temperatures. in: *Proceedings of the 7th International Symposium on Ballistic*, pp. 541–547.
- J. Hyun, J. Hoon, R.H. Wagoner. (2010). A plastic constitutive equation incorporating strain, strain-rate, and temperature. *Int. J. Plastic.* 26 1746–1771. <http://dx.doi.org/10.1016/j.ijplas.2010.02.005>
- C. Roth, D. Mohr. (2014). Effect of strain rate on ductile fracture initiation in advanced high strength steel sheets: Experiments and modeling. *Int. J. Plastic.* 56 (2014) 19–44. <http://dx.doi.org/10.1016/j.ijplas.2014.01.003>
- A.L. Gurson. (1977). Continuum theory of ductile rupture by void nucleation and growth: Part I—yield criteria and flow rules for porous ductile media. *J. Eng. Mater. Tech.* 99 2-15.
- V. Uthaisangskuk, U. Prah, W. Bleck. (2008). Micromechanical modelling of damage behaviour of multiphase steels. *Comput. Mater. Sci.* 43 27–35.
- N. Vajragupta, V. Uthaisangskuk, B. Schmaling, S. Münstermann, A. Hartmaier, W. Bleck. (2012). A micromechanical damage simulation of dual phase steels using XFEM. *Comput. Mater. Sci.* 54 271-279. <http://dx.doi.org/10.1016/j.commatsci.2011.10.035>
- G.R. Johnson, W.H. Cook. (1985). Fracture characteristics of three metals subjected to various strains, strain rates, temperatures and pressures. *Eng. Fract. Mech.* 21 31–48.
- Y. Bao, T. Wierzbicki. (2004). On fracture locus in the equivalent strain and stress triaxiality space. *Int. J. Mech. Sci.* 46 81–98.
- Y. Bai, T. Wierzbicki. (2008). A new model of metal plasticity and fracture with pressure and Lode dependence. *Int. J. Plast.* 24 1071–1096.
- K. Charoensuk, S. Panich, V. Uthaisangskuk. (2017). Damage initiation and fracture loci for advanced high strength steel sheets taking into account anisotropic behaviour. *J. Mat. Pro. Tech.* 248 218–235. <http://dx.doi.org/10.1016/j.jmatprotec.2017.05.035>
- B. Anbarlooie, J. Kadkhodapour H. Hosseini Toudeshky, S. Schmauder. (2017). Micromechanics of Dual-Phase Steels : Deformation, Damage, and Fatigue, *Handbook of Mechanics of Materials*. pp. 1–30, Dec. 2017. [http://dx.doi.org/10.1007/978-981-10-6855-3\\_70-1](http://dx.doi.org/10.1007/978-981-10-6855-3_70-1)

- H. Ghadbeigi, C. Pinna, S. Celotto, J.R. Yates. (2010). Local plastic strain evolution in a high strength dual-phase steel. *Mater. Sci. Eng. A* 527 (2010) 5026–5032. <http://dx.doi.org/10.1016/j.msea.2010.04.052>
- C. Thomser. (2009). *Modelling of the Mechanical Properties of Dual Phase Steels Based on Microstructure*. Shaker Verlag, Aachen.
- J. Liang, Z. Zhao, H. Wu, C. Peng, B. Sun, B. Guo, J. Liang, D. Tang. (2018). Mechanical behavior of two ferrite-martensite dual-phase steels over a broad range of strain rates. *Metals* 8 1-14.
- C. Hengjun, S. Renbo, J. Long, W. Ran, L. Yi, N. Wenjie. (2018). Plastic deformation behavior and construction of constitutive model in a wide range of strain rates of 800 MPa grade dual phase steel. *Mech. Mater.* 122 104–117.
- Y. Okitsu, N. Tsuji. (2014). Effect of ferrite grain size on dynamic tensile properties of ultrafine grained low carbon steels with various chemical compositions. *Mater. Trans.* 55 78-84. <https://doi.org/10.2320/matertrans.MA2323>
- T. Borvik, O.S. Hopperstad, T. Berstad, M. Langseth. (2001). A computational model of viscoplasticity and ductile damage for impact and penetration. *Eur. J. Mech. A/Solids* 20 685–712.
- T. Sirinakorn, V. Uthaisangsuk. (2018). Investigation of damage initiation in high strength dual phase steels using cohesive zone model. *Int. J. Damage Mech.* 27 409-438.
- N.D. Raath, D. Norman, I. Mcgregor, S. Hepple, R. Dashwood, D.J. Hughes. (2018). Characterization of loading responses and failure loci of a boron steel spot weld, *Metall. Mater. Trans. A* 49 1536–1551. <https://doi.org/10.1007/s11661-018-4502-x>.
- A.D. Deole, M.R. Barnett, M. Weiss. (2018). The numerical prediction of ductile fracture of martensitic steel in roll forming, *Int. J. Solids Struct.* 144–145 20–31. <https://doi.org/10.1016/j.ijsolstr.2018.04.011>.
- A. Hillerborg, M. Modéer, P.E. Petersson. (1976). Analysis of crack formation and crack growth in concrete by means of fracture mechanics and finite elements. *Cem. Concr. Res.* 6 773-781.
- N. Biswas, J.L. Ding. (2015). Numerical study of the deformation and fracture behavior of porous Ti6Al4V alloy under static and dynamic loading. *Int. J. Impact Eng.* 82 89-102. <http://dx.doi.org/10.1016/j.ijimpeng.2014.08.011>
- Børvik, O.S. Hopperstad, S. Dey, E.V. Pizzinato, M. Langseth, C. Albertini. (2005). Strength and ductility of Weldox 460 E steel at high strain rates, elevated temperatures and various stress triaxialities. *Eng. Fract. Mech.* 72 1071–1087.

- E.J. Pineda, B.A. Bednarczyk, S.M. Arnold. (2012). Effects of subscale size and shape on global energy dissipation in a multiscale model of a fiber-reinforced composite exhibiting post-peak strain softening using Abaqus and FEAMAC. In: Proceedings of the SIMULIA community conference, Providence, RI, p. 1-14.
- Y. Li, T. Wierzbicki. (2010). Prediction of plane strain fracture of AHSS sheets with post-initiation softening, *Int. J. Solids Struct.* 47 (2010) 2316–2327.  
<https://doi.org/10.1016/j.ijsolstr.2010.04.028>.
- J. Ruzicka, M. Spaniel, A. Prantl, J. Dzukan, J. Kuzelka, M. Moravec. (2012). Identification of ductile damage parameters in the Abaqus, *Bull. Appl. Mech.* 8 89-92.



## APPENDIX A

### X-RAY DIFFRACTION (XRD) RESULTS

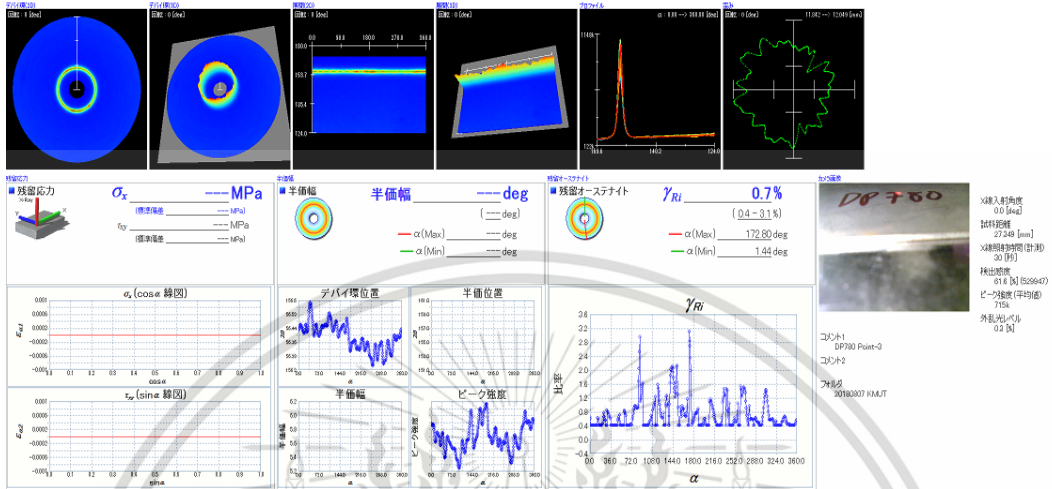


Figure A.1 Resulted XRD investigation of TRIP effect on steel grade 780.

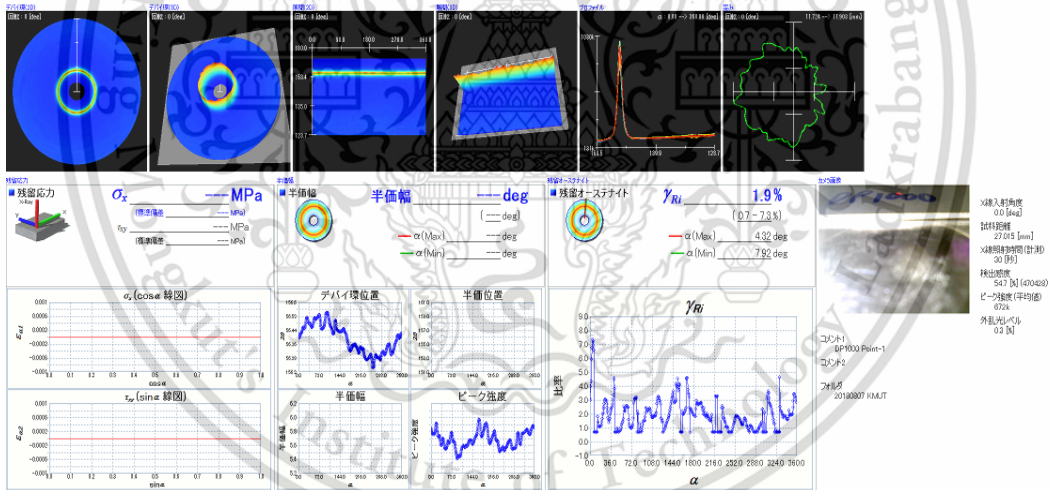
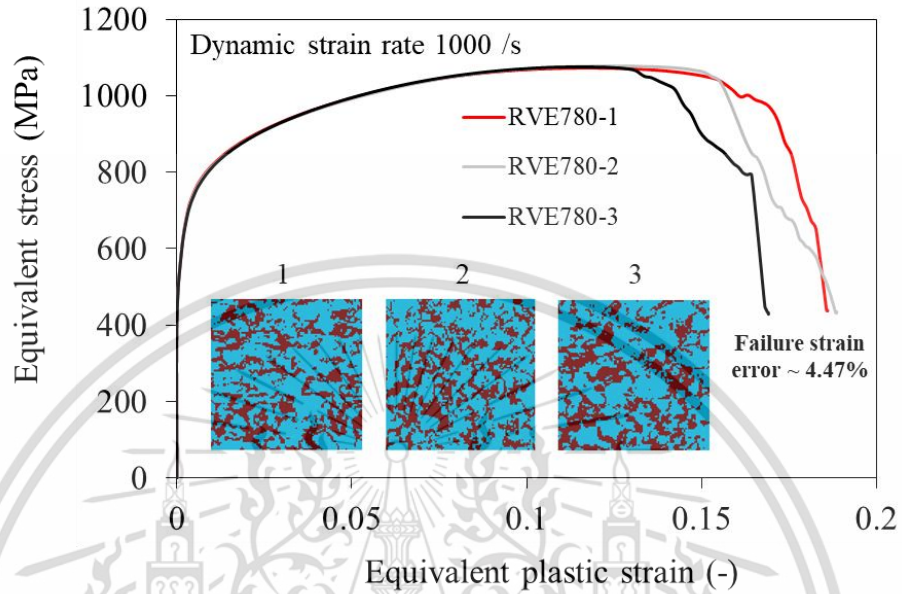


Figure A.2 Resulted XRD investigation of TRIP effect on steel grade 1000.

## APPENDIX B

### EFFECT OF MICROSTRUCTURE CHARACTERISTIC ON SIMULATIONS



**Figure B.1** Resulted stress-strain behaviour of RVE simulations of steel 780 in different microstructure characteristic at dynamic strain rate.

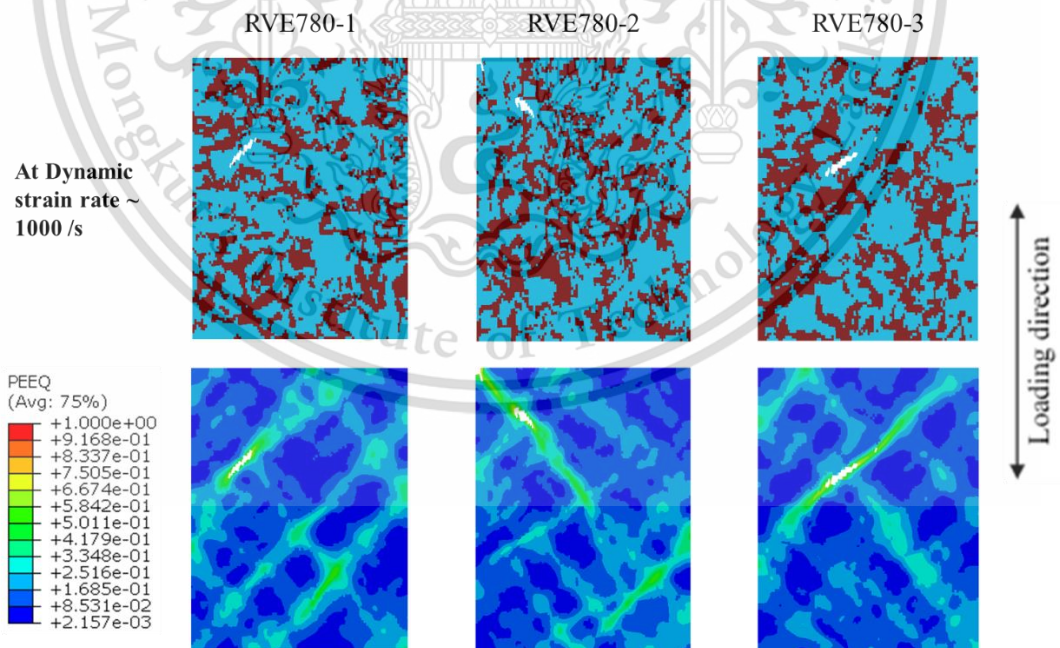
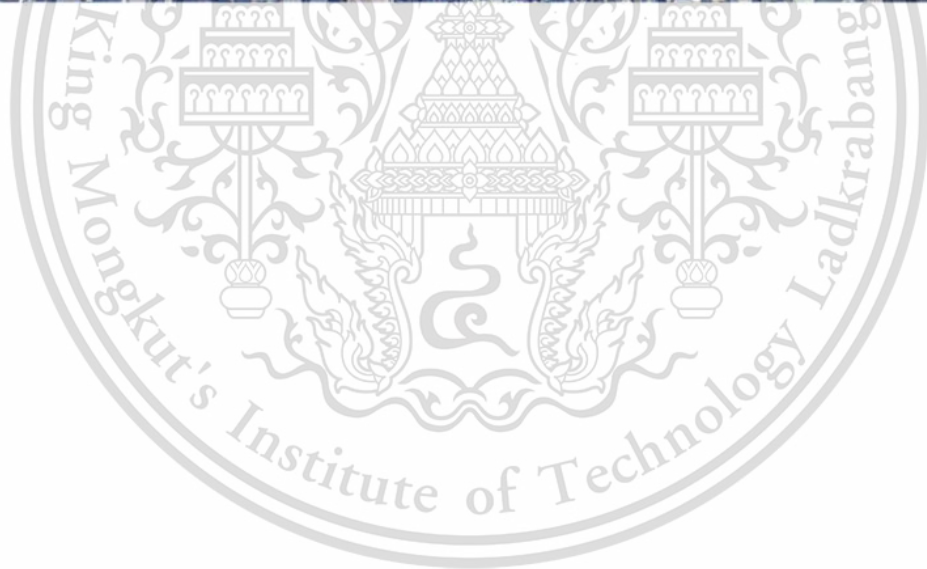


**Figure B.2** Local damage in RVE simulations of steel 780 in different microstructure characteristic at dynamic strain rate.

**APPENDIX C**  
**PUBLICATION**

The 11th International Conference and Workshop on Numerical Simulation of 3D Sheet Metal Forming Processes, July 30-August 3, 2018, Hotel East 21 Tokyo, Tokyo, Japan



PAPER • OPEN ACCESS

## Finite element analysis of AHS steel under dynamic loading using a micromechanical modelling

To cite this article: T Chiyatan *et al* 2018 *J. Phys.: Conf. Ser.* **1063** 012109

View the [article online](#) for updates and enhancements.

### Related content

- [A microstructure based modelling of high strength steel sheet under stretch-bending](#)  
K. Achineethongkham, P. Thanakijkasem and V. Uthaisangasuk
- [An Experimental Study on Mechanical properties of P110S under Dynamic Loads](#)  
Mingfei Li, Lihu Cao, Hailong Geng *et al.*
- [A staggered coupling strategy for the finite element analysis of warm deep drawing process](#)  
J M P Martins, P M Cunha, D M Neto *et al.*



This content was downloaded from IP address 171.98.209.31 on 07/08/2018 at 15:25

## Finite element analysis of AHS steel under dynamic loading using a micromechanical modelling

T Chiyatan<sup>1</sup>, P Karin<sup>1</sup>, N Ohtake<sup>2</sup> and V Uthaisangsuk<sup>3</sup>

<sup>1</sup> International College,

King Mongkut's Institute of Technology Ladkrabang  
Chalongkrung Rd., Ladkrabang, Bangkok 10520, Thailand

<sup>2</sup> Department of Mechanical Science and Engineering  
Tokyo Institute of Technology

2 Chome-12-1 Ookayama, Meguro, Tokyo 152-8550, Japan

<sup>3</sup> Department of Mechanical Engineering, Faculty of Engineering,  
King Mongkut's University of Technology Thonburi  
126 Pracha Uthit Road, Bang Mod, Thung Khru, Bangkok 10140, Thailand

Corresponding author's email: [yitoon.uth@kmutt.ac.th](mailto:yitoon.uth@kmutt.ac.th)

**Abstract.** Currently, advanced high strength (AHS) steel sheets have been increasingly used in the automotive structural parts, where improved crashworthiness and lightweight design are required at the same time. Such steel sheets provide an excellent combination between high strength and great energy absorption. Most AHS steels exhibit microstructures containing several phases and constituents with different morphologies and mechanical properties. In this work, the dual phase (DP) steel grade 780 was investigated under dynamic tensile loading by means of a finite element modelling on the micro-scale. A representative volume element (RVE) model was applied to take into account the effects of microstructure characteristics on the mechanical behaviour of steel sheets at high strain rates. For the RVE modelling, the Johnson-Cook constitutive model was applied to describe the stress-strain response, whereas the Johnson-Cook damage model and damage locus were employed for predicting failure development of each individual phases of examined steel. The RVE simulations were performed under varying strain rates and states of stress and the results were subsequently compared.

### 1. Introduction

By designing a new vehicle, lightweight and passive safety of structural parts must be taken into account. Therefore, understanding material deformation at high strain rates is necessary for achieving the improved crashworthiness of vehicle. Dual phase (DP) steel is one of the most important AHS steel grades that show superior formability and energy absorption behaviour. The DP steels have been successfully employed in such crash-resistance components, by which weight reduction, lower fuel consumption and enhanced safety features of vehicle could be attained. The DP steel is a multiphase steel which has ferritic-martensitic microstructure. The ferritic phase is soft and exhibits good elongation, while the martensitic phase is hard and contributes to strength of DP steels. During the plastic deformation of DP steels, these both phases have strong interactions on the microstructure level. Hence, a micro-scale based model is needed for characterizing the micro-mechanical behaviour



Content from this work may be used under the terms of the Creative Commons Attribution 3.0 licence. Any further distribution of this work must maintain attribution to the author(s) and the title of the work, journal citation and DOI.  
Published under licence by IOP Publishing Ltd

1

of steel so that representative volume element (RVE) FE simulations were taken into account in this work. However, the accuracy of numerical results significantly depends on the used constitutive models and their parameters. The Johnson-Cook (JC) model has been widely applied for predicting plastic deformation of material under high strain rate loading. Besides, various models based on accumulative damage mechanisms could be used as a fracture criterion. For example, the Gurson-Tvergaard-Needleman (GTN) model was successfully employed to describe ductile failure of metals at high stress triaxiality condition [1]. Moreover, the Johnson-Cook damage model has been developed for incorporating the effects of stress triaxiality, strain rate, and temperature [2]. In addition, Bao and Wierzbicki [3] examined the relationships between different fracture strains and stress triaxialities including shear fracture phenomenon and introduced then the damage locus.

In this study, RVE FE simulations in combination with the JC constitutive model were conducted to describe the local high strain rate deformation of DP microstructure. Additionally, the JC damage model and damage locus were applied to predict the fracture behaviour of DP steel on the micro-scale under dynamic loading. The material parameters for each individual phase were identified and provided. The resulted microstructure developments were compared and discussed.

## 2. Material

The dual phase steel sheet grade 780 with the thickness of 1 mm was investigated in this work. The chemical composition of the as-received steel sheet is given in Table 1.

**Table 1.** Chemical compositions of investigated steel grade 780, mass content in %.

Steel grade	C	P	Si	Cu	Ni	Cr	Mn	Mo
780	0.114	0.012	0.010	0.008	0.008	0.183	2.648	0.062

### 2.1. Microstructure

Microstructure of investigated steel was characterized by optical microscopy and the obtained micrograph is presented in figure 1. It was found that the used DP steel grade 780 consisted of about 36% martensitic phase fraction and 64% ferritic phase fraction.

### 2.2. Uniaxial tensile test

Quasi-static uniaxial tensile test of the examined steel sheet was carried out by a universal testing machine. The ASTM E8 standard specimen was used and the test was performed at room temperature with the strain rate of  $0.001 \text{ s}^{-1}$ . The stress-true strain curves of steel specimens were determined and are provided in figure 2. The yield and ultimate tensile strength of steel sheet were 497 and 791, respectively, while the total elongation of around 22.5 % was achieved. It is seen that the steel showed rather low yield strength to tensile strength ratio which is typical for DP steel.

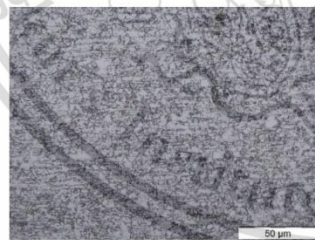


**Figure 1.** Observed microstructure of steel grade 780.

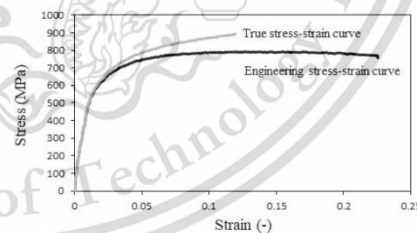


**Figure 2.** Determined stress-true strain curves of investigated steel grade 780.

### 3. FE analysis

In the case of numerical analyses, FE simulations were conducted to predict microstructure behavior of the examined steel under dynamic loading. The strain rate of  $500 \text{ s}^{-1}$  was taken into account. The macroscopic simulations of tensile test under high strain rates were firstly carried out at varying states of stress. A multi-scale approach was applied, in which local strain fields of deformed tensile specimens were taken as the boundary condition of micro-scale model. Note that on the micro-scale a 2D RVE model based on real micrograph was used. The strain rate dependent flow stress curves of DP steel were incorporated by the JC model. Furthermore, the JC damage model and damage locus were applied on the micro-scale for each phase in the RVE. More details will be given later.

#### 3.1. Macroscopic model

**3.1.1. Macroscopic model.** The geometries of tensile specimens were defined in order to obtain varying states of stress. Three different specimens, namely, pure shear, uniaxial, and U-notched [4] were thus employed. Then, FE models of the specimens were generated by using a two-dimensional plane stress (CPS4) element.

**3.1.2. RVE model.** In this work, 2D RVE model was generated on the basis of a random area of real two-phase microstructure of investigated DP steel. Hereby, a micrograph with the size of  $50 \times 50 \mu\text{m}^2$  was used and the element size of RVE model was  $0.5 \times 0.5 \mu\text{m}^2$ . The used RVE model consisting of ferritic and martensitic phase is presented in figure 3. For the RVE model, the CPS4 element was also defined. In addition, the sub-modelling technique was employed to gather the boundary conditions of RVE model from the critical areas of the various macroscopic tensile specimens subjected to tension load.

#### 3.2. Flow curve modelling

**3.2.1. Static flow curves of single phases.** The true stress-true strain curve of ferrite and martensite in the investigated steel sheet were firstly described by considering the carbon partitioning and a dislocation theory [5]. The predicted flow stress curves of both phases under quasi-static loading are illustrated in figure 4.



**Figure 3.** 2D RVE of the investigated steel.

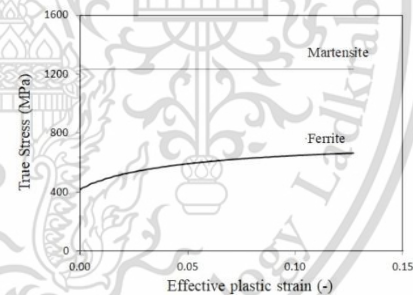


**Figure 4.** Predicted flow stress curves for the individual phases of steel grade 780.

**3.2.2. Dynamic flow stress curve.** The JC constitutive model was used to describe the strain rate dependent flow stress curve of examined steel sheet. Note that, in this work, the JC model parameters were obtained by calibrating with the static flow stress curve and taking from the previous investigations [6-8]. For the macroscopic simulations of tensile specimens, the static stress-strain

curve in figure 2, while for the micro-scale RVE simulations, the predicted single flow stress curves of ferrite and martensite, as shown in figure 4, were used to calibrate the JC parameters of DP steel and each individual phase, respectively. However, the strain rate sensitivity parameters  $C$  of the JC model for DP steel were taken from the literatures [6-8], whereas for ferrite and martensite they were defined as those of the ferritic mild steel and fully martensitic quenched boron steel [6-8]. Note that the carbon contents of both steel sheets were similar to those in ferrite and martensite of the examined DP steel. The identified JC model parameters of DP steel, containing ferritic and martensitic phase are listed in Table 2.

**Table 2.** Identified Johnson-Cook constitutive model parameters of investigated steel [6-8].

	$A$ [MPa]	$B$ [MPa]	$n$	$C$	$\dot{\epsilon}$ [ $s^{-1}$ ]
<b>Steel 780</b>	575	750	0.410	0.0090	0.001
<b>Ferrite</b>	418	700	0.500	0.0220	0.001
<b>Martensite</b>	1226	6	0.001	0.0053	0.001

### 3.3. Damage modelling

In addition, the JC damage model and damage locus were applied for the individual phases in the RVE model in order to describe the damage initiation of DP microstructure under various states of stress. Both ductile damage criteria represented the relationship between the equivalent plastic strain to fracture and governed stress triaxiality. Nevertheless, the damage locus criterion differed from the JC damage model, in which the relationships for low and high stress triaxiality regions were distinguished. To obtain the parameters of JC damage model the damage curves of ferrite [6,9] and martensite [10] determined from previous works were referred. The applied JC damage curves of each phase are given in figure 5. On the other hand, the used damage loci with two triaxiality zones of each single phase were adapted from the damage curves provided in the former investigations [9,10] and literatures [11], which are also demonstrated in figure 5 for a comparison. To describe fracture behaviour on the micro-scale under high strain rate deformation, the corresponding strain rate sensitivity must be taken into account. In this work, the strain rate sensitivities of JC damage model for both phases were assumed to be similar to that of the DP steel grade 780 [9-11]. It is noted that the damage loci for various strain rates were defined by employing this strain rate sensitivity term of JC damage model.

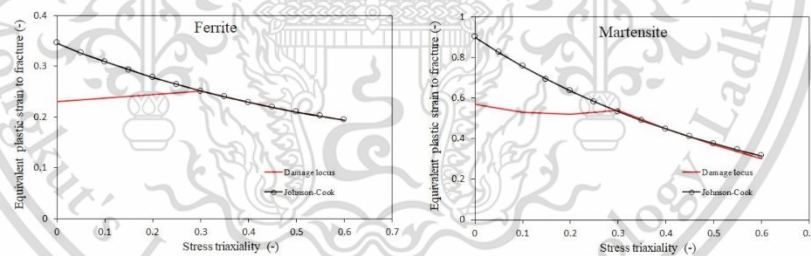


**Figure 5.** Comparisons of damage curves for ferrite and martensite in DP steel represented by the JC damage model and damage locus criterion.

## 4. Results

FE simulations of tensile specimens under varying states of stress were carried out at the strain rate of 500 1/s. The local stress triaxialities of each formed sample were calculated and are shown in figure 6-

7. It was found that the averaged stress triaxiality values of the critical area of pure shear, uniaxial and U-notch samples were 0.05, 0.34 and 0.58, respectively. Afterwards, RVE simulations under different states of stress were performed with the same loading of those critical areas from the corresponding macroscopic simulations. The local damage initiations in the examined DP microstructure under different deformation modes at high strain rates could be predicted and are also illustrated in figure 6-7. It was seen that the crack initiation sites and crack propagations were significantly different when the overall state of stress was changed. Furthermore, the RVE simulations using damage locus with two triaxiality zones noticeably showed fracture behaviour different from those using the JC model, especially in the case of shear loading. For the DP microstructure under uniaxial tensile loading at high strain rate, crack initiations and propagations occurred within the ferritic phase that was well in accordance with the results in [12], as illustrated in figure 8. Note that the calculated local strain rates of RVE were much higher than the overall strain rate of macroscopic specimens. With regard to the JC damage model constant strain rate sensitivity was assumed. However, the dependency between damage and applied strain rate can be certainly varied that will be considered in the future work.

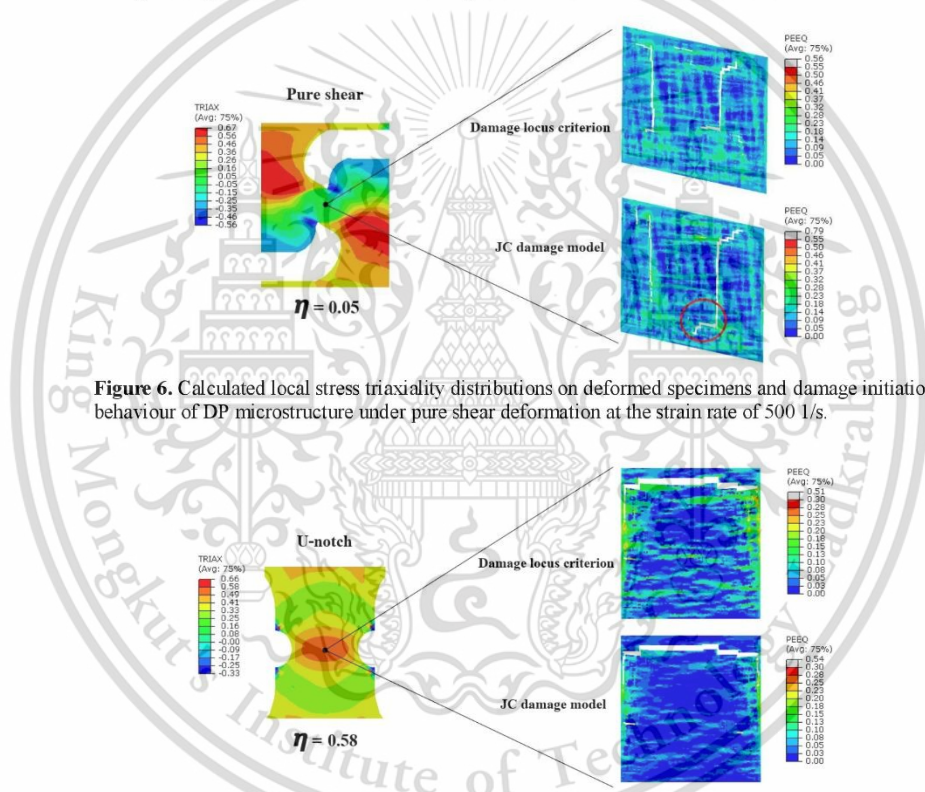


**Figure 6.** Calculated local stress triaxiality distributions on deformed specimens and damage initiation behaviour of DP microstructure under pure shear deformation at the strain rate of 500 1/s.

**Figure 7.** Local stress triaxiality distributions on deformed specimens and calculated local damage initiation behaviour of DP microstructure under tensile deformation of notch sample at the strain rate of 500 1/s.

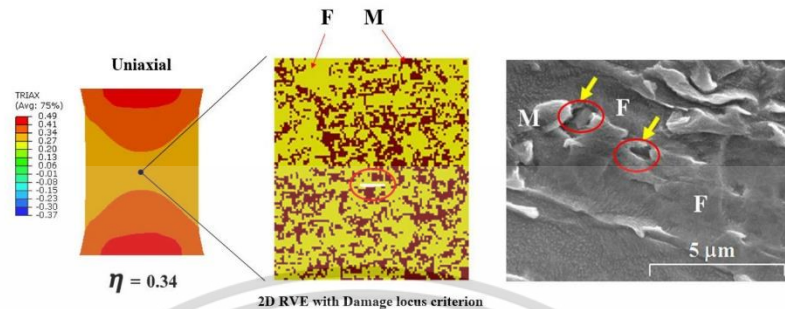


**Figure 8.** Predicted local damage initiation in DP microstructure under uniaxial tensile deformation at the strain rate of 500 1/s in comparison to experimental observations [12].

### 5. Conclusions

FE simulations of tensile specimens under varying states of stress and high strain rate of 500 1/s were performed for the DP steel grade 780. Subsequently, RVE simulations on the microstructure level were carried out for the corresponding samples. The JC model was used to describe the stress-strain responses at high strain rates, in which their parameters were obtained by calibrating with the static flow stress curve of DP steel and containing individual phases. In addition, two damage criteria with and without consideration of low stress triaxiality region were applied to the micro-scale simulations and the predicted damage developments were compared. It was found that the damage initiation and propagation of DP microstructure under shear deformation at high deformation rate predicted by both criteria were significantly different. Local fracture behavior under low triaxiality must be particularly taken into consideration. Additionally, the predicted results will be validated with experimental observations in the future works.

### Acknowledgement

The authors would like to acknowledge the Thailand Research Fund (TRF) and “KMUTT 55<sup>th</sup> Anniversary Commemorative Fund” for financial supports (RSA6180057) and Summit Auto Body Industry for the materials support.

### References

- [1] Gurson L 1977 *J. Eng. Mater. Tech.* **99** 2-15
- [2] Johnson G R and Cook W H 1985 *Eng. Fract. Mech.* **21** (1) 31-48
- [3] Bao Y and Wierzbicki T 2004 *J. Eng. Mater. Tech.* **26** (3) 314-324
- [4] Peirs J, Verleysen P and Degrieck J 2011 *Procedia Eng.* **10** 2336-2341
- [5] Rodriguez R and Gutiérrez I 2003 *Mater. Sci. Forum* 426-432 4525-4530
- [6] Kim J, Kim D, Han H, Barlat F and Lee M 2013 *Mater. Sci. Eng. A* **559** 222-231
- [7] Prabowo D, Kariem M and Gunawan L 2017 *Procedia Eng.* **173** 608-614
- [8] Li H, He L, Zhao G and Zhang L 2013 *Mater. Sci. Eng. A* **580** 330-348
- [9] Vajragupta N, Uthaisangskuk V, Schmaling B, Münstermann S, Hartmaier A. and Bleck W 2012 *Comput. Mater. Sci.* **54** 271-279
- [10] Srithanapan P, Kaewtatip P and Uthaisangskuk V 2016 *Mater. Sci. Eng. A* **667** 61-76
- [11] Yin Q, Zillmann B, Sutner S, Gerstein G, Biasutti M, Tekkaya A, Wagner M, Merklein M, Schaper M, Halle T and Brosius A 2014 *Int. J. Solids Struct.* **51** (5) 1066-1074
- [12] Singh M, Das A, Venugopalan T, Mukherjee K, Walunj M, Nanda T, Kumar B 2017 *Metall. Mater. Trans A* **49** (2) 463-475

## AUTHOR BIOGRAPHY

**Author:** Mr. Tachawut Chiyatan  
**Degree:** Master of Engineering  
**Date of Graduation:** 29/08/2019  
**Date of Birth:** 15<sup>th</sup> June 1994  
**Place of Birth:** Bangkok, Thailand

### Undergraduate and Graduate Education:

Master of Engineering in Automotive Engineering,  
King Mongkut's Institute of Technology Ladkrabang, Bangkok, 2019

Bachelor of Engineering in Production Engineering,  
King Mongkut's University of Technology North Bangkok, Bangkok, 2016

**Major:** Automotive Engineering

### Presentations and Publications:

- [1] T Chiyatan, P Karin, N Ohtake, and V Uthaisangsuk "Finite element analysis of AHS steel under dynamic loading using a micromechanical modelling", 2018, The 11th International Conference and Workshop on Numerical Simulation of 3D Sheet Metal Forming Processes, July 30-August 3, 2018, Hotel East 21 Tokyo, Tokyo, Japan.